

A two-screen model of the variable scintillation of pulsar B1737+13

Sammy Siegel

an Honors Thesis presented to the Oberlin College

Department of Physics and Astronomy

Advisor: Professor Emeritus Dan Stinebring

April 2023

OBERLIN

COLLEGE & CONSERVATORY

Abstract

In this thesis, I discuss a set of observations of the pulsar B1737+13 and develop a two scattering screen model to explain the observed variability in the pulsar's scintillation behavior. I begin by introducing the phenomenon of pulsar scintillation and the underlying physical framework behind one-dimension scattering screen models and scintillation arcs. I then discuss the methods used to analyze the observations as well as the methods of simulating two-screen scattering to compare to the observations. I then present the results of the analysis and simulations. To do this, I develop the idea of interaction arcs to characterize scattering in the two-screen model. I find that the two-screen model and interaction arcs are able to explain key features in the observed variability in the pulsar's scintillation behavior. The explanatory power of this two-screen model provides strong evidence for the existence of two scattering screens along the line of sight to B1737+13.

Dedication

To my parents and sister, for making me who I am.

Acknowledgments

This work would not have been possible if not for the support of my supervisor, Dr. Dan Stinebring. I'm incredibly grateful to him for believing in my abilities and for his support and guidance from the start of this project to the end. I'm indebted to Dan for his kindness, understanding, and advocacy for me. I'm also very lucky to have had the mentorship of Dr. Joey Key at the University of Washington Bothell and Dr. Jeff Hazboun at Oregon State University, who provided me an opportunity to work on this project at the UW Bothell REU program and immerse myself in the NANOGrav community.

I'm also grateful for my mentors at Oberlin. Dr. Jason Stalnaker gave me my first research opportunity in physics, and has been a great source of guidance throughout my entire time at Oberlin. Dr. Yumi Ijiri worked with me for over a year as I developed my skills as a researcher, and was always willing to give me a push in the right direction, whether that be with research, career development, or life generally.

I also owe a sincere debt of gratitude to my collaborators in the field pulsar scintillation. The work of Sprenger et al. (2022) inspired this project, and Tim Sprenger and Robert Main were both incredibly helpful in answering my questions, suggesting directions to pursue, and sharing their code. Marten van Kerkwijk, Daniel Baker, and Rik van Lieshout at the University of Toronto provided invaluable contributions to my methods and simulations, and I'm grateful for the advice and feedback I received at the Scintillometry Workshop at the University of Toronto in 2022 from them and many others. Felix Weber also worked on B1737+13 shortly before I did, and his work was useful to me as I began my own study of

this pulsar.

A great many friends have been there for me during this project and throughout my whole development into a researcher, but I have room to mention only a few of them here. Ilana Meisler and Niels Vanderloo have been there for me time and time again as incredible friends and incredible physicists. Kalista, Kam, and Monica made my experience at UW Bothell incredibly fun, memorable, and intellectually stimulating, and I was very lucky to have their support since the very early stages of this project. I'm also grateful to my friends at Oberlin and elsewhere—Luca, Heather, Kat, Tabassom, Grace, Jess, Caris, Susanne, Ellie, Annabelle, Henry, all the members of Pyle Inn Co-op, and many others—for their support in a multitude of ways. My childhood friends, Sarah and Alexeya, have been there for me since being a scientist was only an aspiration, and they continue to be there as that aspiration becomes a reality.

Finally, I'd like to thank my family. My parents, Mike and Rebecca, and my sister, Miriam, are truly the most wonderful people I know, and their love and support are foundational to all that I am. My grandparents, Lew and Eve, my aunts and uncles, and my cousins are also all owed a great debt of gratitude.

Thank you all! I couldn't have gotten here without you, and I'm excited to see what the future holds.

The Research Experience for Undergraduates program at University of Washington Bothell is funded by National Science Foundation Award #2050928. Additional funding for this thesis project was provided National Science Foundation Award #2009759.

Contents

1	Introduction	8
1.1	Motivation	8
1.2	Radio Wave Propagation in the Interstellar Medium	9
1.3	Pulsars	11
1.4	Scintillation	11
1.5	Observations Analyzed	12
1.6	Thesis Summary	13
2	Pulsar Scintillation: Theory and Observables	14
2.1	Observing Pulsar Scintillation	14
2.1.1	Secondary Spectra	16
2.1.2	The Wavefield	17
2.2	Modeling Scattering in the Interstellar Medium	17
2.2.1	Point Model	17
2.2.2	Oscillator Model	22
2.2.3	Screen Model	24
2.2.4	Derivation of a one-screen model	25
2.3	Scintillation Arcs	29
2.3.1	Multiple Arcs	30
2.3.2	Scintillation Arc Substructure	31

2.3.3	Anisotropy Angle	32
3	Measuring Arc Curvature	34
3.1	Manual Arc Measurement	34
3.1.1	Linearizing the Secondary Spectrum	35
3.2	Theta-Theta Mapping	35
3.2.1	Physical Significance of the Theta-Theta Map	41
3.3	Curvature Search Algorithms	41
4	Simulating Scintillation	45
4.1	Screens Package	45
4.1.1	Code Framework	45
4.1.2	Calculating τ and f_D	47
4.2	Sprenger et. al. (2022) Version	49
4.3	Finding Dynamic Spectra from the Wavefield	53
5	A 36-Epoch Observation of Pulsar B1737+13	54
5.1	Characterizing the Data Set	54
5.2	Measured Curvatures	55
5.2.1	Primary Arc	61
5.2.2	Secondary Arc Curvatures	65
6	Modeling the Scintillation of Pulsar B1737+13	72
6.1	Interaction Curvature	72
6.1.1	Definition	72
6.1.2	A Problem Arises	75
6.1.3	Revising the Definition of Interaction Curvature	77
6.1.4	Characterizing Interaction Curvature Behavior	79
6.2	Modeling	85

7 Conclusion	92
7.1 Summary of Results	92
7.2 Future Work	93
Bibliography	94

Chapter 1

Introduction

1.1 Motivation

This thesis is motivated primarily by the desire to understand the physics of radio wave scattering in the ionized interstellar medium. We concern ourselves with an observation of pulsar B1737+13 made by the Arecibo telescope in 2008, attempting to understand the scintillation behavior of the pulsar in this data set to gain insights into the scattering mechanisms underlying this behavior.

The study of pulsar scintillation has applications for a number of fields in astrophysics. Pulsar scintillation can be used to probe the structure of the interstellar medium, which helps us understand the structure and history of our galaxy. It can also be used to develop timing models for pulsars, which are used for pulsar timing arrays to detect gravitational waves. It also has broad applications in plasma physics, optics, and radio astronomy.

This thesis owes a great intellectual debt of gratitude to the work of Sprenger et al. (2022), who performed a similar study of pulsar scintillation for the pulsar B1508+55. Their work was the inspiration for this thesis and provided a roadmap for how to approach pulsar scintillation for this data set. It also provided an excellent resource for understanding the physics of two-screen scattering, which is the model we use to explain the scintillation behavior of

B1737+13.

1.2 Radio Wave Propagation in the Interstellar Medium

¹The *interstellar medium* (ISM) is the matter that exists between the stars in our galaxy. It is composed of primarily of hydrogen and helium, with a small amount of heavier elements, and is found at differing densities and temperatures depending on the type of region it is in. We are primarily interested in the ionized component of the ISM, in particular the so-called *warm* ISM with a temperature $T \sim 10^4$ K. In the plane of the Milky Way, the number density of hydrogen atoms is approximately 1 cm^{-3} . Of these, about 1 atom out of 30 is ionized, leading to an electron density $n_e \sim 0.03 \text{ cm}^{-3}$. Unlike a neutral gas, this plasma has a natural oscillation frequency, the *plasma frequency*, given by

$$\nu_p = \sqrt{\frac{n_e e^2}{\pi m_e}} = (8.97 \text{ kHz}) n_e^{1/2}, \quad (1.1)$$

where e is the electron charge (cgs units), m_e is the electron mass, and n_e is expressed in cm^{-3} .² This leads to a dispersion relation, $\omega^2 = \omega_p^2 + k^2 c^2$, where $\omega_p = 2\pi\nu_p$ and $k = 2\pi\nu/c$. The phase velocity of an e-m wave in the plasma is $V_p = \omega/k$, and a little algebra shows us that since the group velocity, $V_g = d\omega/dk$, we have $V_p V_g = c^2$ for a plasma. Hence, with $V_p = c\sqrt{1 + \nu_p^2/\nu^2}$, we find that $V_g = c(1 + \nu_p^2/\nu^2)^{-1/2}$. Since for the radio waves of interest ($\nu > 100 \text{ MHz}$) we have $\nu \gg \nu_p$ in the ISM, the group velocity is

$$V_g \approx c \left(1 - \frac{\nu_p^2}{2\nu^2}\right). \quad (1.2)$$

We can see, then, that an impulsive signal, like that from a pulsar, will have higher radio frequencies arriving at the Earth before lower frequencies. In particular, if the pulse travels

¹This section is adapted from private communication with Dan Stinebring.

²A derivation of this can be found in many places. One particularly instructive one can be found in the Feynman Lectures, Vol. II, section 7-3, e. g. https://www.feynmanlectures.caltech.edu/II_07.html.

a distance L , the travel time t will be approximately

$$t = \frac{L}{c} + \frac{e^2}{2\pi m_e c} \frac{\text{DM}}{\nu^2}, \quad (1.3)$$

where the *dispersion measure*, DM, is a measure of the column density of free electrons along the line of sight

$$\text{DM} \equiv \int_0^L n_e \, ds. \quad (1.4)$$

An example of a dispersed pulse is shown in Figure 1.1. Since the plasma frequency is

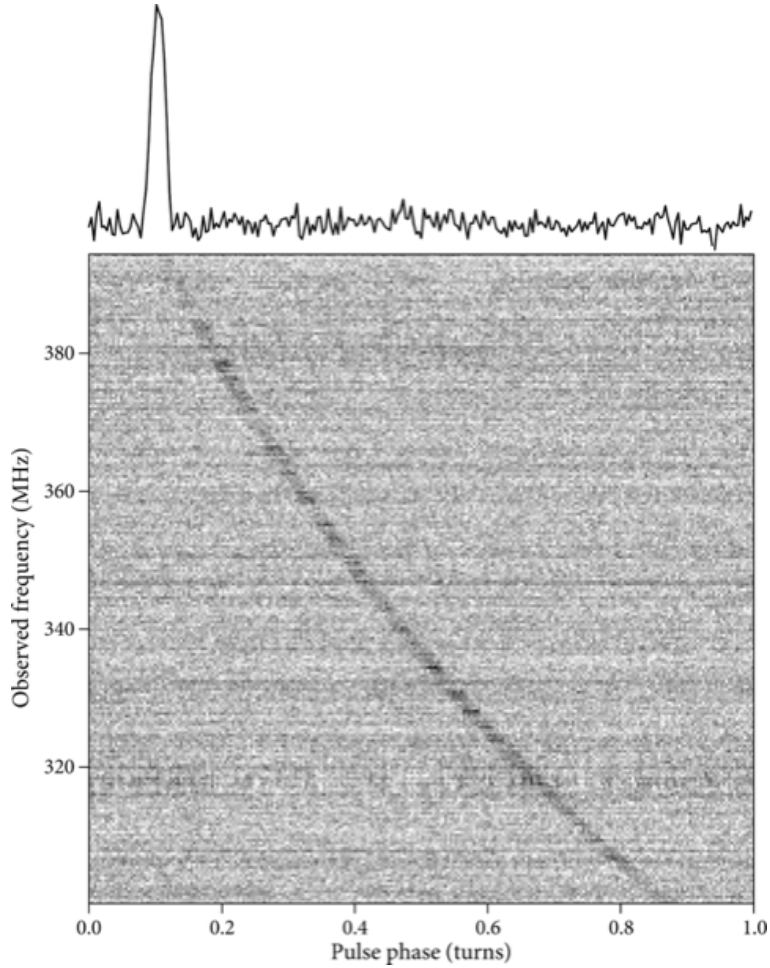


Figure 1.1: An example of a dispersed pulse. Higher frequencies arrive at the Earth before lower frequencies.

density dependent, we also see that an inhomogeneous plasma, like that of the ISM, will

yield refractive effects leading to multi-path scattering, a key phenomenon in what follows.

1.3 Pulsars

Pulsars are neutron stars, which are stellar remnants that result from the collapse of massive stars ($10 - 25M_{\odot}$), leaving behind an incredibly dense core of neutrons supported by neutron degeneracy pressure. Neutron stars are the densest stellar objects in the universe; most have a radius of around 10 km and a mass of around $1.4M_{\odot}$, giving them a density of order $10^{17} - 10^{18} \text{ kg/m}^3$ (Lyne & Smith, 1990). Pulsars are highly magnetized and rapidly rotating neutron stars, with periods of rotation ranging from seconds to milliseconds. Pulsars emit beams of electromagnetic radiation, including radio waves, from their magnetic poles, which sweep across the sky like a lighthouse as a pulsar rotates (Lorimer & Kramer, 2005). They were discovered in 1967 by Jocelyn Bell and Anthony Hewish at Jodrell Bank Observatory (Hewish et al., 1968).

As a probe of the ionized interstellar medium, pulsars have several key properties. First, being both very small and far away, they are incredibly compact sources of radiation. This means their radiation is spatially coherent, acting essentially like point sources. Second, the radiation is pulsed, giving both on- and off-pulse signals that makes it easier to subtract out background noise (Blandford et al., 1992). All of these properties make pulsars ideal sources for studying the ISM.

1.4 Scintillation

In observational astronomy, *scintillation* refers to a range of phenomena that cause the brightness of a source to vary with time. Generally, these phenomena involve a source's radiation traveling through some medium—a medium which is not uniform and is characterized by chaotic fluctuations in density and temperature (Ellison, 1952). This causes light to scatter in a way that changes with time, creating interference that causes the source's brightness

to vary.

The most well-known example of scintillation is the twinkling of stars in the night sky. This occurs due to the starlight scattering as it travels through pockets of air in Earth's atmosphere with varying densities (Ellison, 1952). Scintillation can also be observed for sources of terrestrial origin. For example, looking at West Seattle from across Elliot Bay in the Olympic Sculpture Park one night last summer, I noticed that the lights of the houses appeared to be flickering. This was also due to atmospheric scintillation. We might note one thing about the sources just listed: they are all very small compared to how far away they are. Only compact sources are observed to scintillate, whereas sources with larger angular sizes — like the Moon and planets — do not. The larger angular sizes of these sources means that any scattering that happens is averaged over a larger area, making the effect less noticeable (Rickett, 2001).

It is not just visible light sources that scintillate. As is of interest to us, radio wave sources also scintillate, although the medium that causes this scintillation is not neutral air molecules, but ionized gas and plasma. Ionospheric scintillation was the first of these phenomena to be observed in the early 1950s (Rickett, 2001). Interplanetary scintillation due to the solar wind was first observed for quasars by Margaret Clarke in 1964 and published by Hewish et al. (1964). The phenomenon that is of most interest to us is interstellar scintillation, which we observe for pulsars due to scattering in the ionized interstellar medium (Lyne & Smith, 1990). The primary aim of Chapter 2 will be to describe how we observe and characterize pulsar scintillation to understand the properties of the ISM.

1.5 Observations Analyzed

The data set analyzed in this thesis is a set of observations of pulsar B1737+13 made by the Arecibo telescope in 2008. Observations of pulsar B1737+13 were made using the Arecibo telescope in Puerto Rico. The data set consists of 36 epochs of observations over a period of 38.5 weeks, with the first observation on 5 April 2006 (Modified Julian Day (MJD)

53830) and the last on 31 December 2006 (MJD 54100). Observations were 1 hour long and were made in 4 different frequency bands: 1175 MHz, 1380 MHz, 1425 MHz, and 1470 MHz. What makes this data set of particular interest is that the pulsar was observed to undergo a dramatic change in its scintillation behavior over the course of the observations. The reasons for this change are not well understood, but this thesis will attempt to provide some insight into possible mechanisms at work. More information about the observations is given in Section 5.1.

1.6 Thesis Summary

This thesis is organized into seven chapters. Chapter 1 is this introduction, which provides a brief overview of the motivation for this work, the physics of radio wave propagation in the ISM, and the properties of pulsars, and the phenomenon of scintillation. Chapter 2 describes the theory of pulsar scintillation, including the observable quantities that we use to characterize it and how we understand scintillation due to scattering screens. Chapter 3 describes the methods used to analyze the data to find the curvature of scintillation arcs. Chapter 4 discusses the methods used to simulate two-screen scintillation. Chapter 5 discusses the B1737+13 data set, characterizing the observations in terms of the changing appearance of the scintillation arcs and measurement of arc curvatures over time. Chapter 6 discusses simulations of the B1737+13 data set, developing the idea of “interaction arcs” and using this idea to build a two-screen model of the B1737+13 system that shows promise in explaining the observations. Chapter 7 summarizes the results of this work and discusses future directions for this research.

Chapter 2

Pulsar Scintillation: Theory and Observables

2.1 Observing Pulsar Scintillation

In order to understand how pulsar intensity changes, one must first contend with the fact that pulsar radiation is intrinsically highly variable over time due to the pulsed nature of the radiation. The period of a pulsar is usually much shorter than typical scintillation time scales. As a result, we can probe the longer time scale of scintillation by synchronously averaging pulses at the Doppler-shifted period for a window of time δt , the subintegration time, in essence treating the pulsar as a continuous source (Stinebring et al., 2019). As an important accompaniment to the synchronous averaging of the signal, we also synchronously average the off-pulse noise in a separate window. This gives us a rapidly alternating on/off modulation, with resultant interference suppression and immunity to longer-term drifts in the observing system. Over a total observation time T , our data will be divided into N_t subintegrations with $\delta t = T/N_t$. An FFT-based spectrometer also divides the observing frequency bandwidth B into N_ν frequency channels, each channel with $\delta\nu = B/N_\nu$. Thus, a single observation of pulsar scintillation will yield $N_t \times N_\nu$ data points, with each one

corresponding to the averaged flux density at a particular time and frequency.

It is common to represent these data as an array of pixels indexed along one axis by time and along the other by frequency, with the brightness or color of each pixel representing the average flux density at the corresponding time and frequency. This plot is known as a *dynamic spectrum*, and it provides the primary way of visualizing the changing pulsar intensity as a function of time and frequency. An example dynamic spectrum is shown in Figure 2.1.

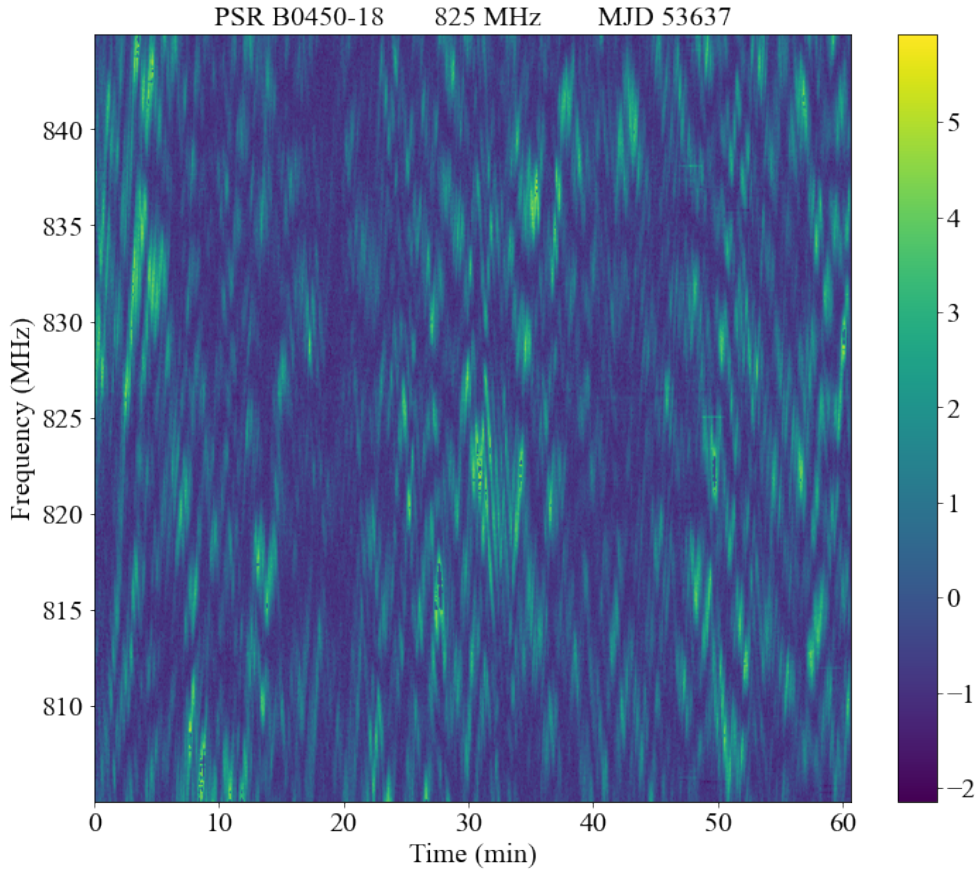


Figure 2.1: An example dynamic spectrum from an observation of pulsar B0450-18 (Stinebring et al., 2022). Pulsar flux density (“Intensity”) is plotted as a function of radio frequency and time, with a bandwidth of 39.9 MHz divided into 1024 channels of width 38.9 kHz and an observation time of 3640 s divided into 364 time bins with subintegration time 10 s. The scintles (elongated patchy regions) that are characteristic of scintillation are clearly visible.

Evidence of interstellar scintillation can be seen in dynamic spectra from the patchy regions of power known as “scintles” that commonly appear. The approximate widths of

these scintles in time and frequency are Δt_{DISS} and $\Delta\nu_{\text{DISS}}$, respectively (Stinebring, 2007).

2.1.1 Secondary Spectra

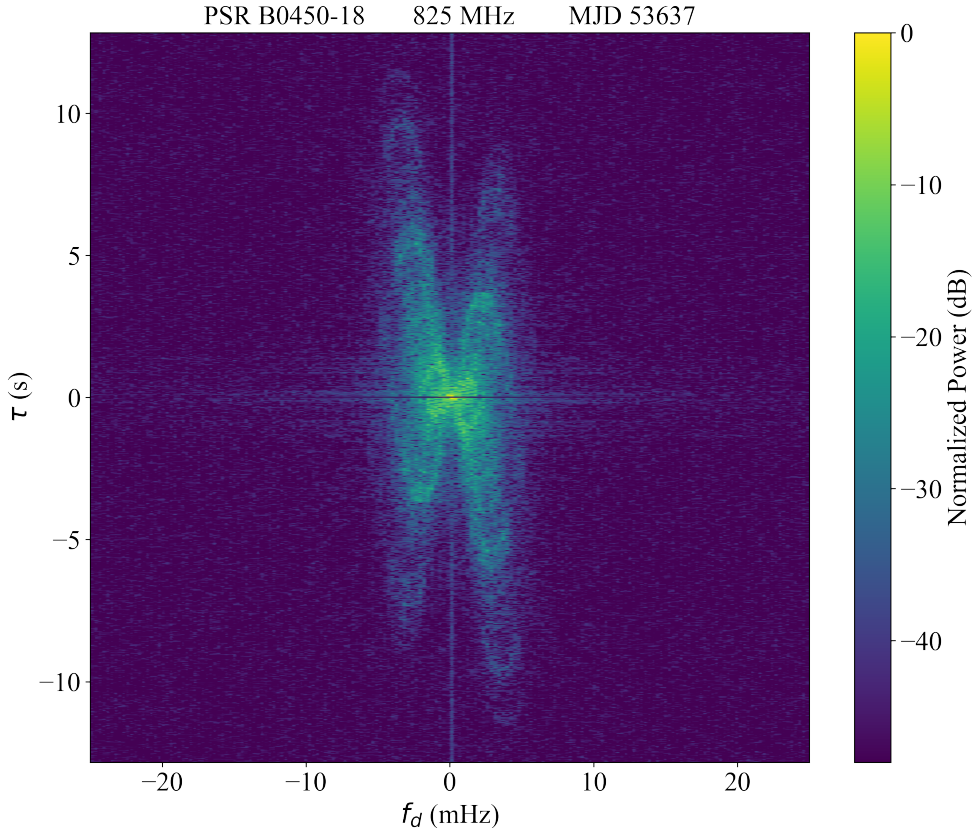


Figure 2.2: An example secondary spectrum from an observation of pulsar B0450-18 (Stinebring et al., 2022). Power, in decibels, is plotted as a function of time delay τ , on the order of μs , and Doppler frequency shift f_D , on the order of mHz. A parabolic scintillation arc is clearly visible.

The crisscross patterns that can be seen in dynamic spectra imply a periodicity in time and frequency. This provided the impetus for performing a 2D Fourier transform of the dynamic spectra (Stinebring et al., 2001, e.g.). The power spectrum of this transform is called the *secondary spectrum*, defined as

$$S_2(f_\nu, f_t) = \left| \tilde{S}(\nu, t) \right|^2,$$

with $S(\nu, t)$ the dynamic spectrum and \tilde{S} its 2D Fourier transform (Hill et al., 2003). The axes of the secondary spectrum are conjugate time, f_t , and conjugate frequency, f_ν . These are also often respectively denoted as f_D ¹ and τ , as will be explained in Section 2.2.4.

An example secondary spectrum is shown in Figure 2.2. Note that power is concentrated in a parabolic arc. These parabolic arcs are called *scintillation arcs*, and are characteristic features of pulsar observation observed in a large number of pulsars (Stinebring et al. (2022), Main et al. (2023)). A physical explanation for such arcs is given in Section 2.3.

2.1.2 The Wavefield

In simulations of pulsar scintillation, we are often not just interested in the secondary spectrum for a simulated observation, but also a representation known as the *wavefield*. The wavefield $W(f_\nu, f_t)$ can be thought of as the 2D Fourier transform of $E(t, \nu)$, the electric field at the observer. We can also understand the secondary spectrum as the autoconvolution of the wavefield (Baker et al., 2022). Thus, the wavefield representation is a useful, and, in a sense, more fundamental way to represent information about scintillation, and we will calculate it in our simulations (see Chapter 4). An example wavefield is shown with its corresponding secondary spectrum in Figure 2.3.

2.2 Modeling Scattering in the Interstellar Medium

2.2.1 Point Model

Consider a system of an observer, a pulsar located a distance D_{psr} away, and a thin screen of plasma between them at a distance D_{scr} . The pulsar, screen, and observer each have associated (2D) transverse velocities of \mathbf{v}_{psr} , \mathbf{v}_{scr} , and \mathbf{v}_{obs} respectively. We can use the parameter $s \in [0, 1]$ to describe the distance to the screen, with $s = (D_{\text{psr}} - D_{\text{scr}})/D_{\text{psr}}$. Thus, the screen is a distance $s D_{\text{psr}}$ from the pulsar and $(1 - s)D_{\text{psr}}$ from the observer.

¹Also written as f_d

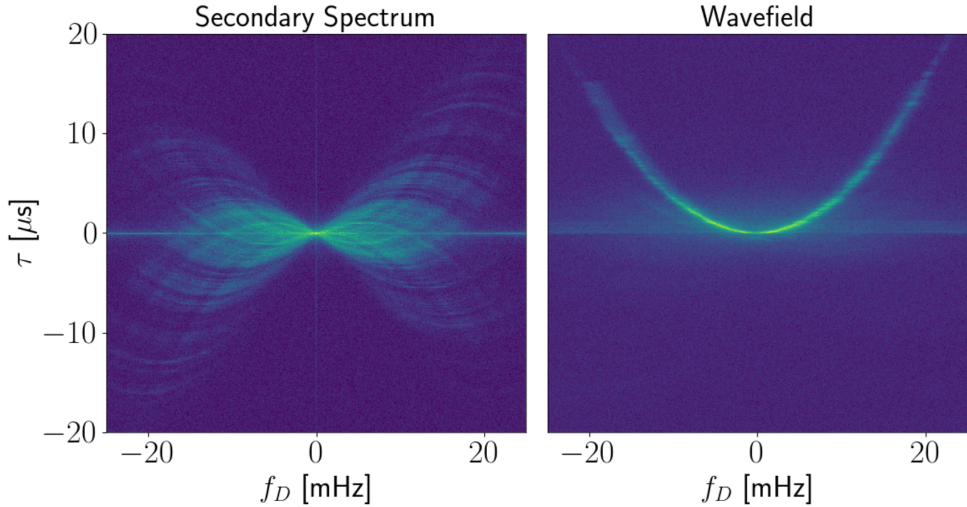


Figure 2.3: An example wavefield from an observation of pulsar B1508+55 shown on the right, with the corresponding secondary spectrum shown on the left. The secondary spectrum is the autoconvolution of the wavefield. Figure from Sprenger et al. (2022). The wavefield is not generally directly observable, and the wavefield shown here was calculated using an assumption of 1-D scattering.

Now, consider two ray paths traveling from the pulsar to the observer. The first ray travels directly along the line of sight, with no deflection. The second ray travels at an angle θ_{psr} to the first and is scattered off of a point at the screen, approaching the observer at an angle θ_{obs} relative to the first ray. This situation is represented in Figure 2.4. The two rays then recombine at the observer. Because the source is a pulsar, the rays are coherent, so the electric field at the observer is the sum of the two rays. When the rays recombine, they interfere with each other. Because we are dealing with only two rays, we can understand this situation as analogous to two-slit interference. This is represented in Figure 2.5, in which we have a broadband incident plane wave of light passing through two slits a distance D from the observer. One slit is directly along the line of sight, while the other is offset from the line of sight by a distance d . The light produces an interference pattern at the observer's plane. If the observer moves along this plane at a speed v , the intensity of light observed will change periodically with time. The spacing y between fringes in the interference pattern is given by $y = (\lambda/d) D = \lambda/\theta$, with $\theta = d/D$ under a small angle approximation. This is the

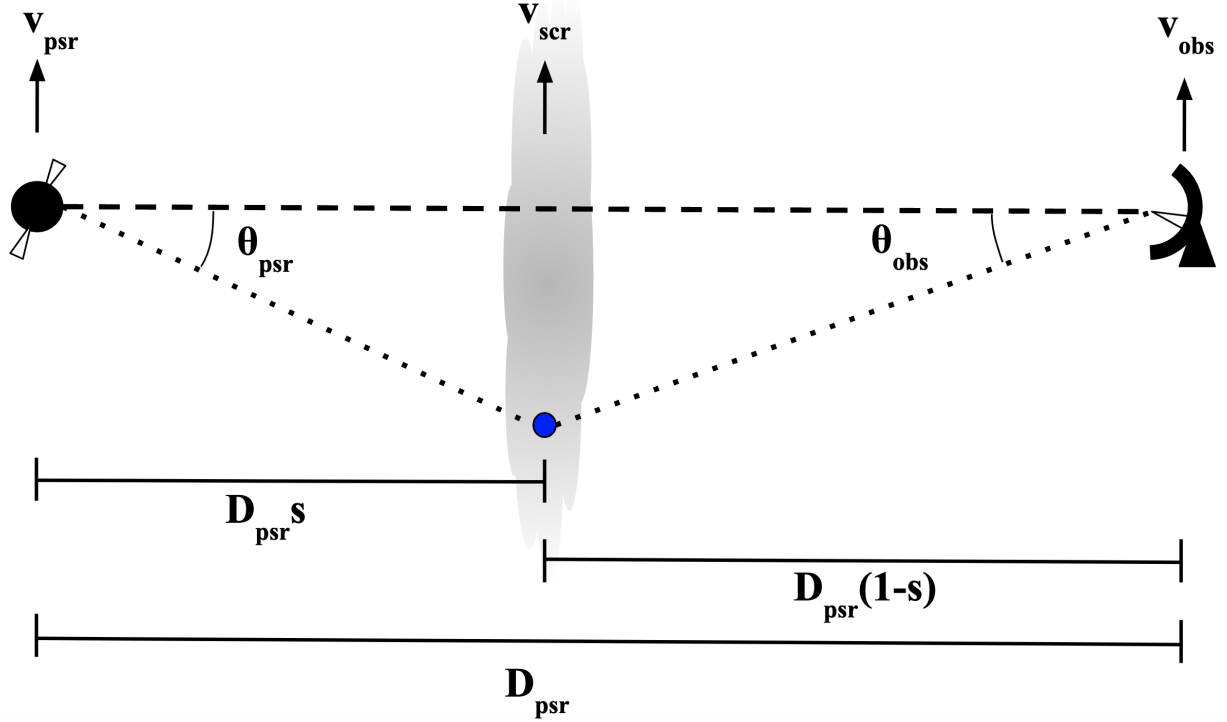


Figure 2.4: The point model of scattering - angles on mas scale

periodicity in *space*, but, since our observer is moving through space at speed v , they will experience intensity as varying in *time* with a periodicity of $\Delta t = \lambda/(v\theta)$, or a frequency of

$$f_t = \frac{v}{\lambda} \theta. \quad (2.1)$$

A periodicity in frequency is also introduced because the light from both slits is broad-band, with a range of frequencies and associated amplitudes. The two slits are at different distances to the observer, with the path length difference between them being $\Delta l = \sqrt{D^2 + d^2} - D = D [(1 + \theta^2)^{1/2} - 1] \approx D(1 + \frac{1}{2}\theta^2 - 1) = \frac{D}{2}\theta^2$. The time delay is then $\tau = \frac{D}{2c}\theta^2$. This time delay will cause the signal from the upper slit to be shifted in phase relative to the signal from the lower slit. However, this phase shift will be frequency dependent since $\Delta\phi = \omega\Delta t = 2\pi\nu\tau$. If, at some frequency ν , $\nu\tau = n$ for some integer n , the component of the two signals at this frequency will be in phase, and constructively interfere. At other frequencies, the two signals will arrive out of phase. Thus, the intensity of light at

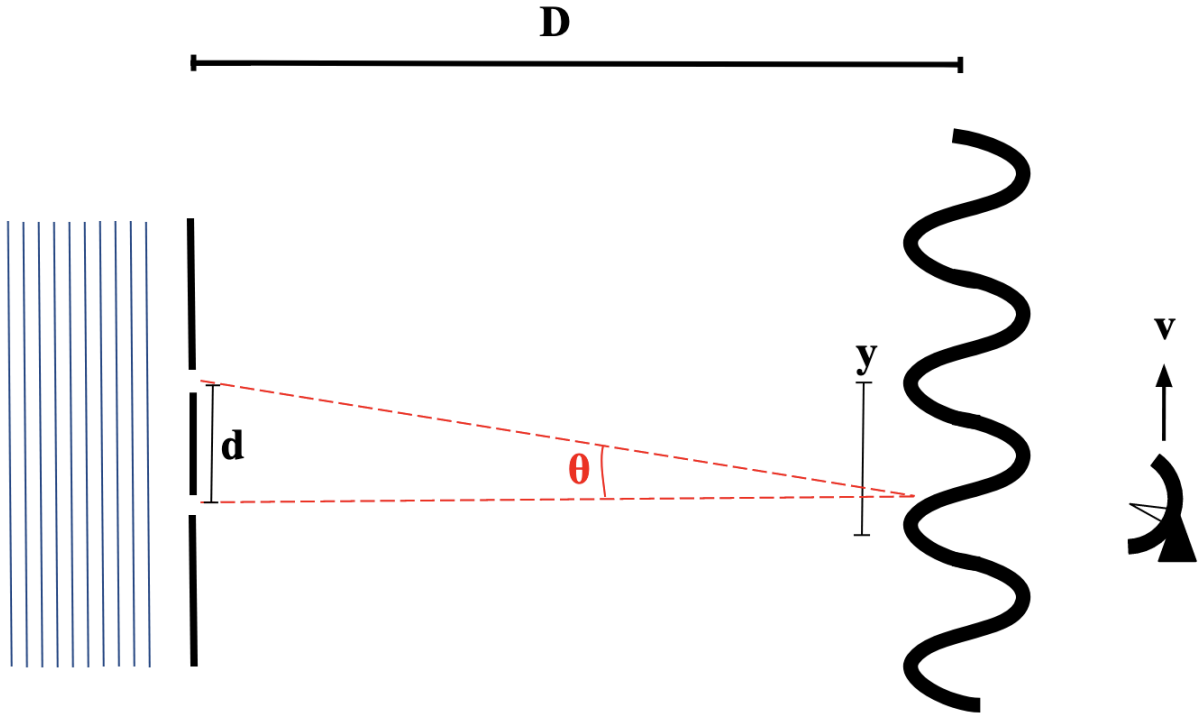


Figure 2.5: An analogous situation to the point model of scattering with an incident plane wave of light passing through two slits separated by a spacing d located at a distance D from the observer. The light produces an interference pattern at the observer's plane. If the observer moves along this plane at a speed v , the intensity of light observed will change periodically with time and frequency.

the observer will be periodic in frequency, with a period of $\Delta\nu = \frac{1}{\tau}$ between peak intensities, or a modulation frequency of

$$f_\nu = \tau = \frac{D}{2c}\theta^2. \quad (2.2)$$

The quantities f_ν and f_t are related, as we can discover by seeing how they evolve in time and frequency, respectively. Starting from Equation 2.2, we find

$$\frac{df_\nu}{dt} = \frac{d}{dt} \left(\frac{D}{2c}\theta^2 \right) = \frac{D}{c}\theta \frac{d\theta}{dt}. \quad (2.3)$$

Recall that $\theta = d/D$, so $\dot{\theta} = \dot{d}/D = v/D$, as distance d changes as the line of sight moves at the speed of the observer. Thus,

$$\frac{df_\nu}{dt} = \frac{v}{c}\theta. \quad (2.4)$$

Meanwhile, the frequency derivative of f_t is given by

$$\frac{df_t}{d\nu} = \frac{d}{d\nu} \left(\frac{\nu v}{c} \theta \right) = \frac{v}{c} \theta. \quad (2.5)$$

We find that

$$\frac{df_\nu}{dt} = \frac{df_t}{d\nu}. \quad (2.6)$$

From this, we can see that f_t is linearly related to \dot{f}_ν , scaling with frequency:

$$f_t = \nu \dot{f}_\nu. \quad (2.7)$$

Note that f_t has units of time, and is equal to the geometric time delay τ between the two signals. Thus, f_t is often referred to simply as the time delay or geometric delay and denoted τ . Likewise, f_ν has units of frequency, and is often denoted as f_D and called the Doppler shift. Section 2.2.4 will show that f_D can be found as the relative Doppler shift between a scattered image and a line of sight image. Section 2.2.4 will also derive τ as the geometric time delay between the scattered and line of sight images for the slightly more complicated geometry of Figure 2.4. The results are quoted below, but they should look very familiar to Equations 2.2 and 2.1:

$$\tau = \frac{1}{2c} D_{\text{eff}} \theta_{\text{obs}}^2, \quad (2.8)$$

$$f_D = \frac{\nu}{c} v_{\text{eff},\parallel} \theta_{\text{obs}}. \quad (2.9)$$

Here, D_{eff} is given by

$$D_{\text{eff}} = \frac{1-s}{s} D_{\text{psr}} = \frac{D_{\text{psr}} D_{\text{scr}}}{D_{\text{psr}} - D_{\text{scr}}}, \quad (2.10)$$

while $v_{\text{eff},\parallel}$ is the velocity of the interference pattern with respect to the observer in the direction to the line of images, given by

$$v_{\text{eff},\parallel} = \frac{1-s}{s} v_{\text{psr},\parallel} - \frac{1}{s} v_{\text{scr},\parallel} + v_{\text{obs},\parallel}. \quad (2.11)$$

Derivations for D_{eff} and $v_{\text{eff},\parallel}$ are also given in Section 2.2.4.

2.2.2 Oscillator Model

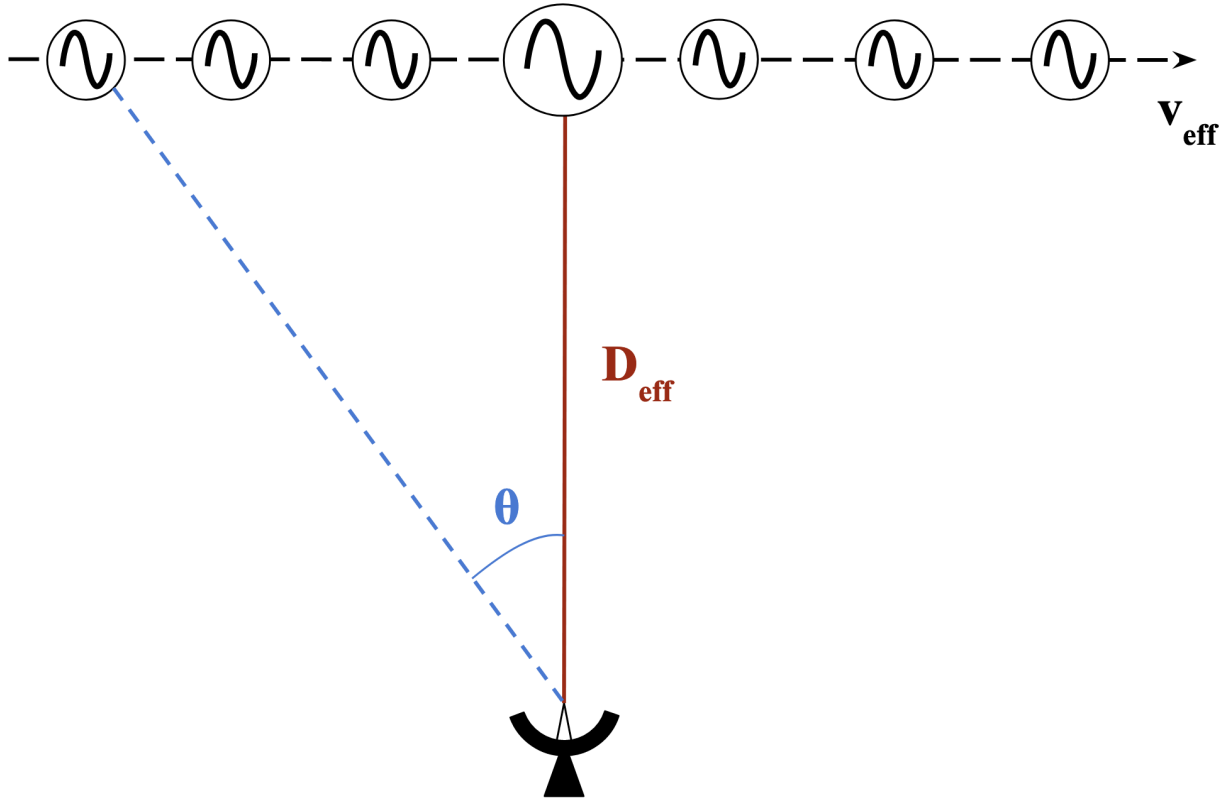


Figure 2.6: The oscillator model of scattering. A line of signal generators moves with speed v_{eff} at a closest-approach distance of D_{eff} .

The oscillator model is the next step up in complexity from the point-scattering model. Now, instead of one image, we have multiple images represented by a line of n signal generators in the sky. The line of signal generators is a distance D_{eff} away and moves with a speed of v_{eff} as shown in Figure 2.6. Each oscillator is a coherent source that emits the same signal

at a range of frequencies, mimicking the signal from a pulsar. Each signal generator also produces a different intensity of signal, with the oscillator closest to the line of sight producing the strongest signal representing the unscattered line-of sight signal. We can represent this by giving each oscillator a complex magnification μ , with the amplitude representing the strength of the signal and the phase representing the electromagnetic phase of the signal. Unlike with the point model, where we have interference between only two signals, here we have interference between many signals at once. If we consider the interference between oscillator j and oscillator k , we will find that they produce interference that is periodic in time and frequency akin to the point model, with

$$\tau_{jk} = \frac{1}{2c} D_{\text{eff}} (\theta_j^2 - \theta_k^2), \quad (2.12)$$

and

$$f_{D,jk} = -\frac{\nu}{c} v_{\text{eff}} (\theta_j - \theta_k). \quad (2.13)$$

The electric field at the observer from such interference as a function of time and frequency is then a 2D sinusoid given by:

$$E_{jk}(t, \nu) = \mu_j \mu_k \exp 2\pi i (\tau_{jk} \nu + f_{D,jk} t). \quad (2.14)$$

An example of a 2D sinusoid is shown in Figure 2.7. If we want to find the total electric field at the observer, we need to consider the interference between all pairs of oscillators, summing up all the 2D sinusoids from each pair. This is given by:

$$E_{\text{tot}}(t, \nu) = \sum_{j=1}^{n-1} \sum_{k=j+1}^n E_{jk}(t, \nu). \quad (2.15)$$

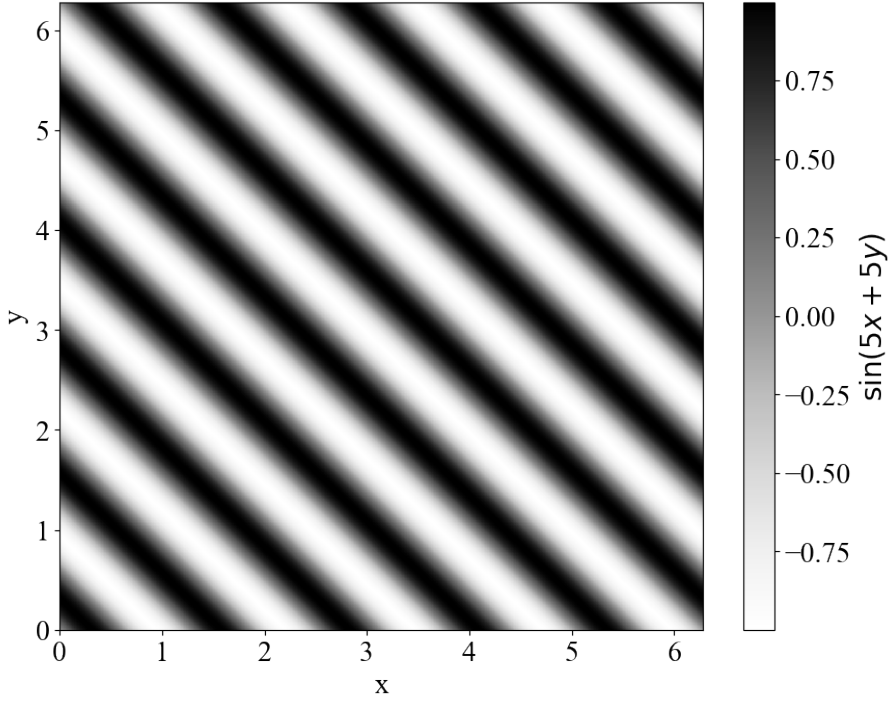


Figure 2.7: An example of a 2D sinusoid, in this case the function $f(x, y) = \sin(5x + 5y)$, plotted on the interval $x \in [0, 2\pi]$ and $y \in [0, 2\pi]$.

2.2.3 Screen Model

The screen model is the model that we will use to understand the scattering of a pulsar signal. However, we have already identified all of the main features of the screen model in previous models. I list them below to provide a concise description of what we have learned so far:

- Unlike the point and oscillator models, we consider a scattering screen to have a continuous line of images rather than a discrete set of images. However, we will inevitably have to approximate a screen as a set of discrete images in order to simulate it.
- Screen images lie along a line contained within a plane perpendicular to the line of sight. We say that a screen has *1D anisotropy* because scattering occurs along this line, which is sometimes referred to as a *line of anisotropy*.
- A screen can have some transverse velocity \mathbf{v}_{scr} and is located at a distance sD_{psr} from

the pulsar and a distance $D_{\text{scr}} = (1 - s)D_{\text{psr}}$ from the observer. θ_{obs} describes the position of a point on the screen (see Figure 2.4), where $\theta_{\text{obs}} = d/D_{\text{scr}}$ and d is the distance between the point intersecting the line of sight and that particular point.

- Interference between the line of sight image and a scattered image on the screen is given by Equations 2.8 and 2.9.
- As with the oscillator model, we can give each point on the screen a complex magnification μ , although μ now follows a continuous distribution $\mu(\theta_{\text{obs}})$. The electric field from the interference between two screen images is also given by Equation 2.14.

2.2.4 Derivation of a one-screen model

In this section, we will derive the time delay and doppler shift for a one-screen model of scattering.

Derivation of τ

We will begin with the situation in Figure 2.8. The time delay can be found by first finding the path-length difference between the scattered and unscattered rays. The unscattered ray travels a distance of D_{psr} . The scattered ray travels in two legs: from the pulsar to the screen and from the screen to the observer. The distance traveled from the pulsar to the screen is given by the Pythagorean theorem as

$$\sqrt{(D_{\text{psr}}s)^2 + (D_{\text{psr}}s\theta_{\text{psr}})^2} = D_{\text{psr}}s\sqrt{1 + \theta_{\text{psr}}^2}. \quad (2.16)$$

Meanwhile, the distance traveled from the screen to the observer is given by

$$\sqrt{(D_{\text{psr}}(1 - s))^2 + (D_{\text{psr}}(1 - s)\theta_{\text{obs}})^2} = D_{\text{psr}}(1 - s)\sqrt{1 + \theta_{\text{obs}}^2}. \quad (2.17)$$

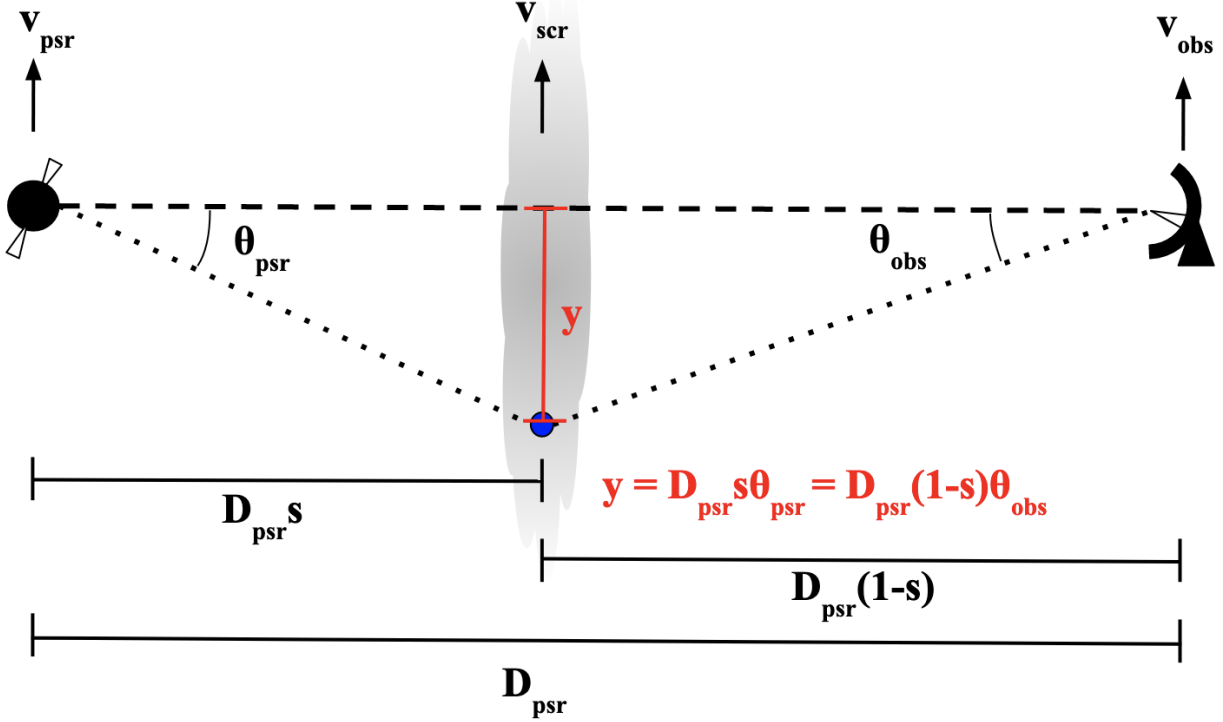


Figure 2.8: The point model of scattering, highlighting that $\theta_{\text{psr}} = (1 - s)\theta_{\text{obs}}/s$.

The total path length is the sum of these two legs, so the difference in path length is

$$\Delta l = D_{\text{psr}}s\sqrt{1 + \theta_{\text{psr}}^2} + D_{\text{psr}}(1 - s)\sqrt{1 + \theta_{\text{obs}}^2} - D_{\text{psr}}. \quad (2.18)$$

Both θ_{psr} and θ_{obs} are very small, so we can approximate the square root as $1 + \theta^2/2$. This gives us

$$D_{\text{psr}} \left[s \left(1 + \frac{\theta_{\text{psr}}^2}{2} \right) + (1 - s) \left(1 + \frac{\theta_{\text{obs}}^2}{2} \right) - 1 \right] \quad (2.19)$$

$$= D_{\text{psr}} \left[s + s \frac{\theta_{\text{psr}}^2}{2} + 1 - s + (1 - s) \frac{\theta_{\text{obs}}^2}{2} - 1 \right] \quad (2.20)$$

$$= D_{\text{psr}} \left[s \frac{\theta_{\text{psr}}^2}{2} + (1 - s) \frac{\theta_{\text{obs}}^2}{2} \right]. \quad (2.21)$$

We can now observe that the our two angles are both opposite the same length, allowing us to solve for θ_{psr} in terms of θ_{obs} :

$$\theta_{\text{psr}} = \frac{1 - s}{s} \theta_{\text{obs}}. \quad (2.22)$$

Substituting this into equation 2.21 gives us

$$\Delta l = D_{\text{psr}} \left[s \left(\frac{1-s}{s} \right)^2 \frac{\theta_{\text{obs}}^2}{2} + (1-s) \frac{\theta_{\text{obs}}^2}{2} \right] \quad (2.23)$$

$$= \frac{D_{\text{psr}}}{2} \theta_{\text{obs}}^2 \left[\frac{(1-s)^2}{s} + \frac{s(1-s)}{s} \right] \quad (2.24)$$

$$= \frac{D_{\text{psr}}}{2} \theta_{\text{obs}}^2 \left[\frac{1-s}{s} ((1-s) + s) \right] \quad (2.25)$$

$$= \frac{D_{\text{psr}}}{2} \frac{1-s}{s} \theta_{\text{obs}}^2. \quad (2.26)$$

Time delay is then this quantity divided by the speed of light:

$$\tau = \frac{\Delta l}{c} = \frac{D_{\text{psr}}}{2c} \frac{1-s}{s} \theta_{\text{obs}}^2. \quad (2.27)$$

At this point, we introduce $D_{\text{eff}} = D_{\text{psr}} \frac{1-s}{s}$. This gives us the familiar looking equation

$$\tau = \frac{D_{\text{eff}}}{2c} \theta_{\text{obs}}^2. \quad (2.28)$$

Derivation of f_{D}

Doppler shift is given by

$$\Delta\nu = \frac{\Delta v}{c} \nu_0. \quad (2.29)$$

Here, Δv is the relative speed at which the source is moving towards or away from the observer. In our one-screen model, the images are moving transverse to the line of sight at a speed $v_{\text{eff},\parallel}$. Relative to the observer, this velocity will have both a transverse and radial component. Directly at the line of sight, the motion is entirely transverse, so the radial component is zero and consequently the Doppler shift is also zero.² However, as we look at

²Note that the line of images as a collective can also be moving radially towards or away from the observer, but this radial motion is nearly the same for all images and therefore contributes negligibly to the relative Doppler shift.

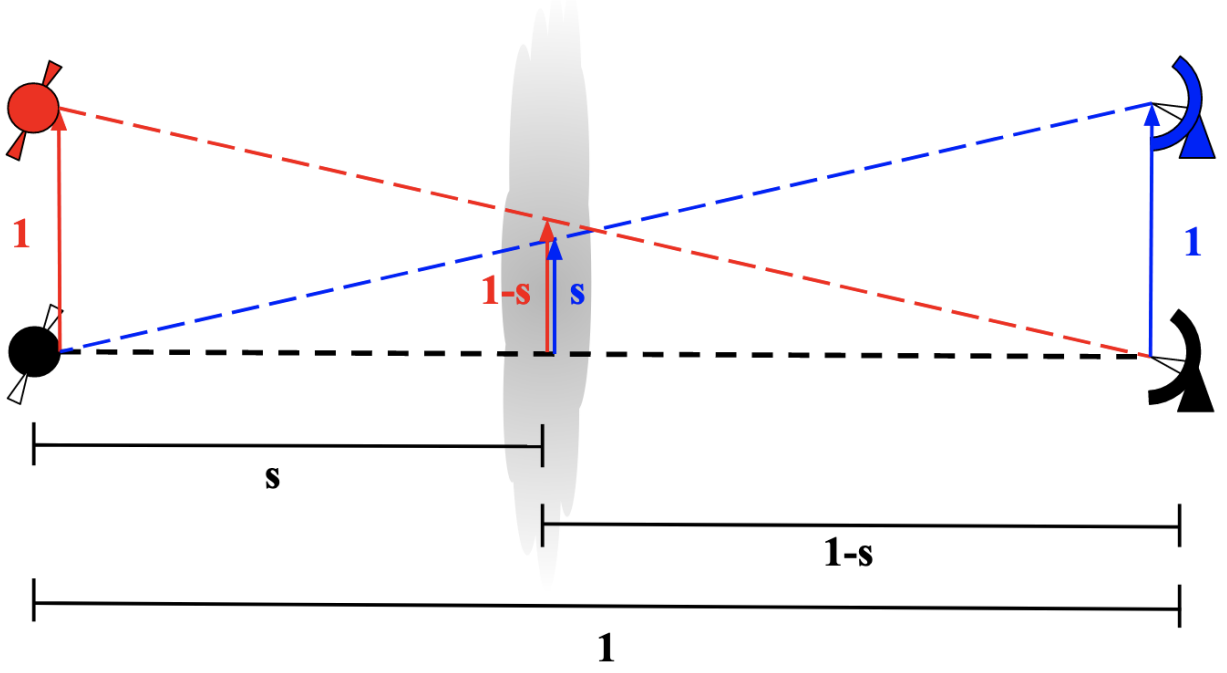


Figure 2.9: A diagram showing how the velocity of the screen images relative to the line of sight, $v_{\text{los},\parallel}$, can be calculated as a sum of velocities of the pulsar, screen, and observer, weighted by the distance the line of sight moves at the screen if pulsar, screen, or observer move a distance of one unit in the transverse direction.

images further away from the line of sight, we introduce a radial component that increases the further away we look. If we look an angle θ_{obs} away from the line of sight, the radial component is $v_{\text{eff},\parallel} \sin \theta_{\text{obs}}$. With a small angle, we can approximate this as

$$v_{\text{eff},\parallel} \theta_{\text{obs}} \quad (2.30)$$

It still remains for us to find $v_{\text{eff},\parallel}$. $v_{\text{eff},\parallel}$ is the speed at which the images are moving transverse to the line of sight from the perspective of the observer. However, it will be easier for now to find the speed of the line of sight $v_{\text{los},\parallel}$ relative to the screen. This can be found by taking a weighted sum of the velocities of the pulsar, the observer, and the screen, as is shown in figure 2.9. The weights are found by how far the line of sight moves at the screen if the pulsar, screen, or observer move a distance of one (arbitrary) unit in the transverse

direction.

If the pulsar moves one unit in the transverse direction, the line of sight moves a distance of $1 - s$ units at the screen. If the screen moves one unit in the transverse direction, the line of sight, relative to the screen, moves -1 units. If the observer moves one unit in the transverse direction, the line of sight moves a distance of s units at the screen. So, we can construct $v_{\text{los},\parallel}$ as

$$v_{\text{los},\parallel} = (1 - s)v_{\text{psr},\parallel} - v_{\text{scr},\parallel} + sv_{\text{obs},\parallel}. \quad (2.31)$$

Now, to find $v_{\text{eff},\parallel}$, we can take $v_{\text{los},\parallel}$ and convert it to a velocity relative to the observer. The relative weights of the velocity terms will be preserved, but the weighting of the $v_{\text{obs},\parallel}$ term should now be 1. So, we can divide by s to find

$$v_{\text{eff},\parallel} = \frac{1 - s}{s}v_{\text{psr},\parallel} - \frac{1}{s}v_{\text{scr},\parallel} + v_{\text{obs},\parallel}. \quad (2.32)$$

With this knowledge, we can now calculate the Doppler shift. Using equations 2.29 and 2.30, we find for a particular image that

$$\Delta\nu = \frac{\nu}{c}v_{\text{eff},\parallel}\theta_{\text{obs}}. \quad (2.33)$$

Now, f_D is the *relative* Doppler shift between the two images. But, if the first image is at the line of sight, the Doppler shift is zero. So

$$f_D = \Delta\nu - 0 = \frac{\nu}{c}v_{\text{eff},\parallel}\theta_{\text{obs}}. \quad (2.34)$$

2.3 Scintillation Arcs

As previously mentioned, scintillation arcs are parabolic arcs of power in secondary spectra that are characteristic of diffractive scintillation by 1D screens. Scintillation arcs have been observed in dozens of pulsars (Stinebring et al., 2022), and this section will discuss these

arcs to explain their importance in uncovering the physical parameters underlying a pulsar's scintillation.

As we have shown, τ and f_D are both parameterized by θ_{obs} , the angle at the observer between the line of sight and the image. We can use this to solve for τ as a function of f_D . First, from Equation 2.9

$$\theta_{\text{obs}} = \frac{c}{\nu v_{\text{eff},\parallel}} f_D. \quad (2.35)$$

Substituting this into Equation 2.8, we find

$$\tau = \frac{D_{\text{eff}}}{2c} \frac{c^2}{\nu^2 v_{\text{eff},\parallel}^2} f_D^2. \quad (2.36)$$

We have found a quadratic relationship between τ and f_D given by

$$\tau = \eta f_D^2, \quad (2.37)$$

where the arc curvature η is given by

$$\eta = \frac{D_{\text{eff}} c}{2\nu^2 v_{\text{eff},\parallel}^2}. \quad (2.38)$$

η is a parameter that can be directly measured from a secondary spectrum. Thus, it can be used as a powerful tool for finding D_{eff} , which is much harder to measure directly. The very existence of a parabolic arc in the secondary spectrum is also evidence of 1D screen-like scattering, since it is only this geometry that produces a relationship between τ and f_D for which Equation 2.37 holds. As a result, observing scintillation arcs and measuring η are the main ways of characterizing pulsar scintillation.

2.3.1 Multiple Arcs

The secondary spectra of some pulsars have been observed to contain not just one scintillation arc, but several arcs of different curvatures. For example, McKee et al. (2022) have

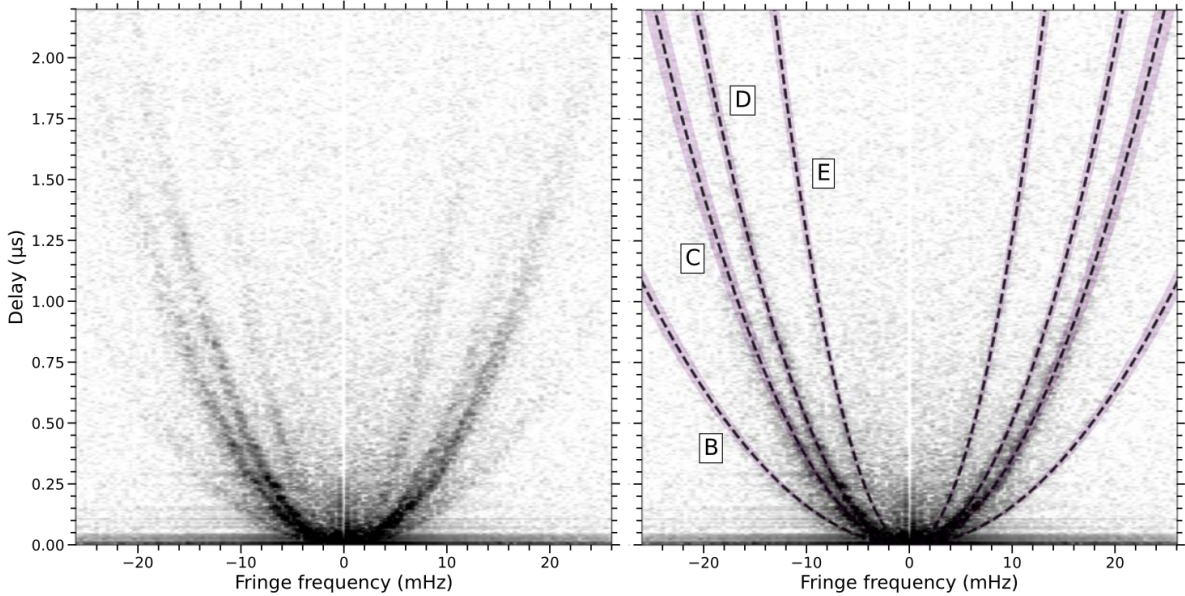


Figure 2.10: A secondary spectrum of B1133+16 showing multiple clear arcs, labeled B, C, and E. Figure taken from McKee et al. (2022).

identified six arcs in the secondary spectra of pulsar B1133+16. If one scintillation arc corresponds to a single screen along the line of sight, then multiple arcs correspond to multiple screens. However, not all arcs are likely to be as visible as others, and a system may have different screens visible in different observations. The easiest way to identify multiple screens is to observe multiple arcs in a secondary spectrum. This is the case with B1133+16, as can be seen in Figure 2.10. However, there are some systems with multiple screens where the identification of multiple arcs is not as straightforward. This is the case with pulsar B1508+55 as shown by Sprenger et al. (2022), and it is also the case with the pulsar under study here, B1737+13.

2.3.2 Scintillation Arc Substructure

While some scintillation arcs have power in a thin, well defined parabola, others have more complicated substructure. The most common example are *inverted arclets*. These are parabolic arcs that open downwards, are much smaller in extent than the main arc, and have their apexes at a point on the main arc. Recall equations 2.12 and 2.13, which differ from

the general expressions for τ and f_D in that their theta terms involve two angles, θ_j and θ_k . If one of these angles is zero, then these equations reduce to 2.8 and 2.9, from which we get our equation for the main parabola. If, however, we fix θ_j to be non-zero, then we can write our equations as

$$\tau = \tau_j - \frac{D_{\text{eff}}}{2c} \theta_k^2 \quad (2.39)$$

and

$$f_D = f_{D,j} + \frac{\nu v_{\text{eff},\parallel}}{c} \theta_k, \quad (2.40)$$

where τ_j and $f_{D,j}$ are the values of τ and f_D from interference between θ_j and the line of sight. We can then again find τ as a function of f_D by first noting that

$$\theta_k = \frac{c}{\nu v_{\text{eff},\parallel}} (f_D - f_{D,j}). \quad (2.41)$$

Substituting this into Equation 2.39, we find

$$\tau = \tau_j - \frac{D_{\text{eff}}}{2c} \left(\frac{c}{\nu v_{\text{eff},\parallel}} (f_D - f_{D,j}) \right)^2. \quad (2.42)$$

Therefore,

$$\tau - \tau_j = -\eta (f_D - f_{D,j})^2. \quad (2.43)$$

This is a parabola that opens downwards with curvature $-\eta$ and apex at $(f_{D,j}, \tau_j)$. In other words, this describes an inverted arclet. We can see, then, that an inverted arclet arises from interference between screen images and another image not on the line of sight.

2.3.3 Anisotropy Angle

In the previous sections of this chapter, we have referred just to $v_{\text{eff},\parallel}$ when calculating f_D , remaining agnostic about the direction of anisotropy at which the images are found. However, this does not have to be the case. Let us now let the 1D anisotropy on the screen

be at angle α with respect to some reference. A natural reference to use is a line in the transverse plane at constant declination for the observer. This will be the \hat{x} direction, while the \hat{y} direction will be in the transverse plane normal to \hat{x} . We will define the origin of our scattering screen to be at the intersection of this line with the line of sight. Under this framework, we can define the vector quantity $\boldsymbol{\theta}_{\text{obs}}$ representing a dimensionless position that gives the coordinates of an image on the screen as

$$\boldsymbol{\theta}_{\text{obs}} = D_{\text{scr}} \theta_{\text{obs}} (\cos \alpha \hat{x} + \sin \alpha \hat{y}). \quad (2.44)$$

We can now also define the effective velocity as a vector quantity with respect to the same coordinate system, with

$$\mathbf{v}_{\text{eff}} = \frac{1-s}{s} \mathbf{v}_{\text{psr}} - \frac{1}{s} \mathbf{v}_{\text{scr}} + \mathbf{v}_{\text{obs}}. \quad (2.45)$$

For the purposes of calculating the Doppler shift, we need the component of \mathbf{v}_{eff} in the direction of $\boldsymbol{\theta}_{\text{obs}}$, as this is the velocity along the line of images. Thus, we can write the Doppler shift as

$$f_{\text{D}} = \frac{\nu}{c} (\mathbf{v}_{\text{eff}} \cdot \boldsymbol{\theta}_{\text{obs}}) \quad (2.46)$$

or

$$f_{\text{D}} = \frac{\nu}{c} v_{\text{eff}} \theta_{\text{obs}} \cos \alpha. \quad (2.47)$$

The curvature, η , can now be written as

$$\eta = \frac{D_{\text{eff}} c}{2\nu^2 v_{\text{eff}}^2 \cos^2 \alpha}. \quad (2.48)$$

As a result, η is now not just dependent on D_{eff} and v_{eff} , but also on α .

Chapter 3

Measuring Arc Curvature

As described in Section 2.3, the curvature of a scintillation arc has a direct correspondence with the physical parameters of the corresponding screen(s) that produce the arc. Thus, measuring the curvature of an arc is a vital step in the analysis of scintillation data. In this section, I will outline the various methods used to measure arc curvature. These techniques apply both image processing techniques and an understanding of the pulsar-screen-Earth system.

3.1 Manual Arc Measurement

A straightforward method of measuring arc curvature is simply to have a human manually identify the arc to be measured and then to identify points in the arc that can be used to produce a best-fit value of curvature using a least-squares fit. This process makes use of a free web-based tool called WebPlotDigitizer, which allows the user to identify points of interest in an image and extract their coordinates (Rohatgi, 2022). A process for manually measuring arc curvature from a secondary spectrum is outlined as follows:

1. Upload and open the image of the secondary spectrum in WebPlotDigitizer.
2. Use the Calibration tool to identify the axes in the image and their scale.

3. Use the “Add Point” tool to identify points in the arc that can be used to produce a best-fit value of curvature.
4. View the data produced, and export it to a text file.
5. Using a data analysis software of choice, fit a 2nd order polynomial to the data points and extract the curvature value as the coefficient of the 2nd order term.

A visual demonstration of this process is shown in Figure 3.1.

3.1.1 Linearizing the Secondary Spectrum

While the manual measurement of a parabolic arc is generally straightforward, it is much easier for the eye to identify a straight line than a parabola. Thus, we can linearize the secondary spectrum before arc measurement to make the process easier, following the example of Sprenger et al. (2022). For a parabolic arc passing through the origin given by $\tau = \eta f_D^2$, we can linearize the secondary spectrum by plotting $\sqrt{\tau}$ vs. f_D , with $\sqrt{\tau} = \sqrt{\eta}f_D$. This transformation is shown in Figure 3.2. Manual measurement can then be performed on the transformed image, this time fitting a first-order polynomial to the points on the arc identified by the user. The curvature value is then the square of the coefficient of the first-order term.

3.2 Theta-Theta Mapping

Recall that, for a 1D anisotropic screen, we can express τ and f_D corresponding to two interfering rays from screen positions θ_1 and θ_2 as

$$\tau = \frac{1}{2c} D_{\text{eff}} (\theta_1^2 - \theta_2^2) \quad (3.1)$$

$$f_D = -\frac{\nu}{c} v_{\text{eff},\parallel} (\theta_1 - \theta_2), \quad (3.2)$$

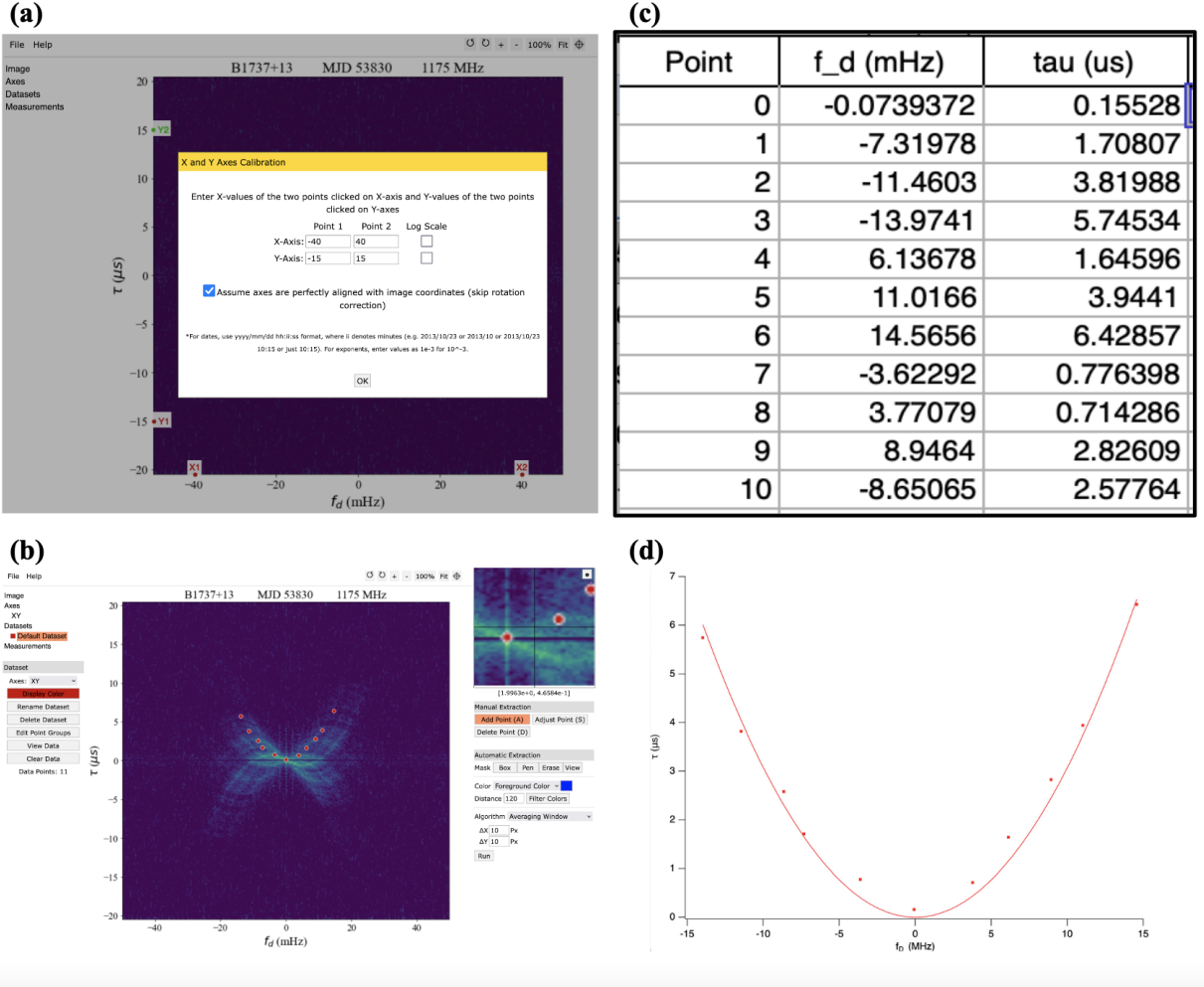


Figure 3.1: A demonstration of the manual measurement process using WebPlotDigitizer. In panel (a), the user identifies the axes and calibrates the scale. In panel (b), the user selects points from which to extract coordinates. In panel (c), the user has exported the coordinates to a text file for analysis. In panel (d), the user has fit a 2nd order polynomial to the data from which the curvature value can be extracted.

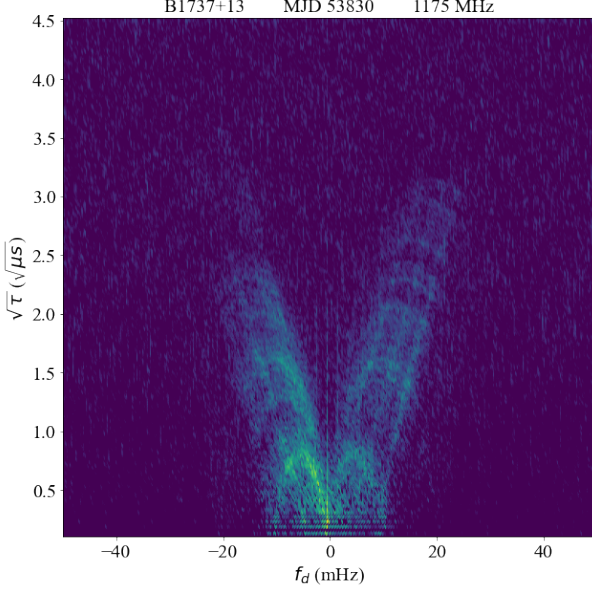


Figure 3.2: An example of the linearization of a secondary spectra for an observation of pulsar B1737+13. The parabolic arc has been transformed into two straight lines, making manual curvature measurement easier.

and a scintillation arc curvature from such a screen

$$\eta = \frac{c D_{\text{eff}}}{2\nu^2 v_{\text{eff},\parallel}^2}, \quad (3.3)$$

where $v_{\text{eff},\parallel} = v_{\text{eff}} \cos \alpha$. τ and f_D are observational parameters that can be measured from a secondary spectrum, but θ_1 and θ_2 are physical parameters related to the screen. Thus, if we are interested in learning about the 1D screen that can produce a given secondary spectrum, it is helpful to move from our observational parameters to physical ones. This is the aim of the theta-theta mapping technique, which was first developed by Sprenger et al. (2021). To transform a secondary spectrum (τ vs. f_D) into theta-theta space (θ_2 vs. θ_1), we solve equations 3.1 and 3.2 for θ_1 and θ_2 in terms of τ and f_D .

Following the derivation of Sprenger et al. (2021), we can simplify this process by defining

$$\tilde{\theta}_i = -\frac{\nu v_{\text{eff},\parallel}}{c} \theta_i, \quad (3.4)$$

which allow us to write our equations for τ and f_D as

$$\tau = \eta(\tilde{\theta}_1^2 - \tilde{\theta}_2^2), \quad (3.5)$$

$$f_D = \tilde{\theta}_1 - \tilde{\theta}_2. \quad (3.6)$$

Note then that we can linearize our expression for τ by taking $\frac{\tau}{f_D}$ instead:

$$\frac{\tau}{f_D} = \eta(\tilde{\theta}_1 + \tilde{\theta}_2). \quad (3.7)$$

This now gives us two linear equations for two unknowns, $\tilde{\theta}_1$ and $\tilde{\theta}_2$, which can be easily solved:

$$\tilde{\theta}_1 = \frac{1}{2} \left(\frac{1}{\eta f_D} \tau + f_D \right), \quad (3.8)$$

$$\tilde{\theta}_2 = \frac{1}{2} \left(\frac{1}{\eta f_D} \tau - f_D \right). \quad (3.9)$$

Thus, we now have equations for transforming a secondary spectrum into theta-theta space. We can now convert back from $\tilde{\theta}_1$ and $\tilde{\theta}_2$ to θ_1 and θ_2 using equation 3.4. However, this is a non-linear transformation, which presents several challenges. θ_1 and θ_2 diverge at $f_D = 0$, and one pixel in theta-theta space can correspond to multiple pixels in the secondary spectrum. To account for this, Sprenger et al. (2021) develop an approach that first defines a grid of pixels in theta-theta space. Then, for each pixel, the θ_1 and θ_2 values corresponding to the corners of the pixel are transformed to secondary spectrum coordinates, defining an area in the secondary spectrum. The intensity of the pixel in theta-theta space can then be found by integrating the intensity over the corresponding area in the secondary spectrum.

Note that theta-theta mapping assumes a curvature of η for the transformation. Suppose now that our 1D screen has a curvature of η' , with $\varepsilon = \eta'/\eta$. Using equations 3.5 and 3.6 and following Sprenger et al. (2021), we write the transformation equations to $\tilde{\theta}_1$ and $\tilde{\theta}_2$ from a

pair of angles ϕ_1 and ϕ_2 as:

$$\tilde{\theta}_1 = \frac{1}{2} \left(\frac{\eta'(\phi_1^2 - \phi_2^2)}{\eta(\phi_1 - \phi_2)} + \phi_1 - \phi_2 \right) \quad (3.10)$$

$$\tilde{\theta}_1 = \frac{1}{2} (\varepsilon(\phi_1 + \phi_2) + \phi_1 - \phi_2) \quad (3.11)$$

$$\tilde{\theta}_1 = \frac{\varepsilon + 1}{2} \phi_1 + \frac{\varepsilon - 1}{2} \phi_2. \quad (3.12)$$

Likewise,

$$\tilde{\theta}_2 = \frac{\varepsilon - 1}{2} \phi_1 + \frac{\varepsilon + 1}{2} \phi_2. \quad (3.13)$$

If we now solve for $\tilde{\theta}_1$ in terms of $\tilde{\theta}_2$, we get

$$\tilde{\theta}_1 = \frac{\varepsilon + 1}{2} \phi_1 + \frac{\varepsilon - 1}{2} \frac{2}{\varepsilon + 1} \left(\tilde{\theta}_2 - \frac{\varepsilon - 1}{2} \phi_1 \right) \quad (3.14)$$

$$\tilde{\theta}_1 = \frac{\varepsilon - 1}{\varepsilon + 1} \tilde{\theta}_2 + \frac{1}{2} \left((\varepsilon + 1) - \frac{(\varepsilon - 1)^2}{\varepsilon + 1} \right) \phi_1 \quad (3.15)$$

$$\tilde{\theta}_1 = \frac{\varepsilon - 1}{\varepsilon + 1} \tilde{\theta}_2 + \frac{2\varepsilon}{\varepsilon + 1} \phi_1. \quad (3.16)$$

Similarly, we find

$$\tilde{\theta}_2 = \frac{\varepsilon - 1}{\varepsilon + 1} \tilde{\theta}_1 + \frac{2\varepsilon}{\varepsilon + 1} \phi_2. \quad (3.17)$$

As $\varepsilon \rightarrow 1$, our guess η approaches the true η' , and the equations reduce to

$$\tilde{\theta}_1 = \phi_1 \quad (3.18)$$

$$\tilde{\theta}_2 = \phi_2, \quad (3.19)$$

and letting ϕ_1 or ϕ_2 vary will give us straight horizontal or vertical lines in theta-theta space.

If, however, we make a bad guess of η , then we will not get horizontal and vertical lines. This property of theta-theta mapping allows us to test whether our guess of η is accurate. Two

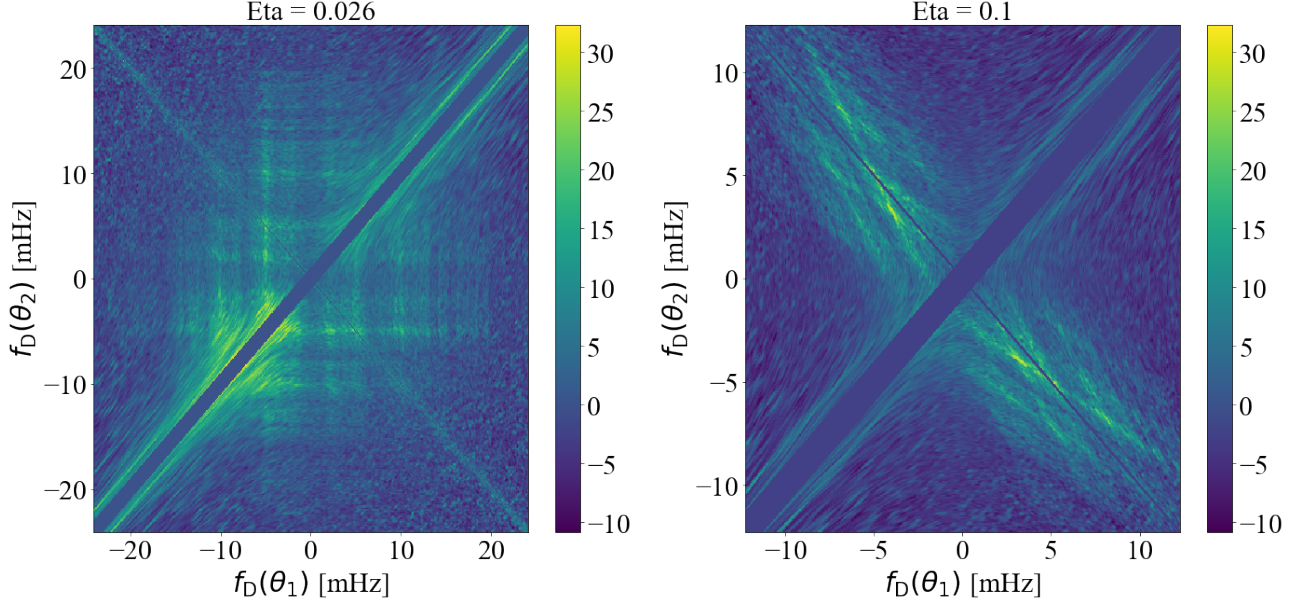


Figure 3.3: Theta-theta maps made using a good guess of $\eta = 0.026 \text{ s}^3$ (left) and a bad guess of $\eta = 0.010 \text{ s}$ (right). The left image shows clear horizontal and vertical lines that indicated our guess of η was accurate. The features in the right image are inclined from the horizontal and vertical, indicating that our guess of η was not accurate. These theta-theta maps were both made using the same observation of PSR B1737+13 at 1175 MHz on MJD 53830 using code provided Tim Sprenger.

theta-theta maps are shown in Figure 3.3 demonstrating a map made with a good guess of η and a map made with a bad guess of η .

Theta-theta mapping was performed using two different codes. The first used an implementation developed by Baker et al. (2022) contained within the Scintools Python package (Reardon, 2023) (Reardon et al., 2020). This was used for coherent theta-theta mapping, where only a chunk of the dynamic spectrum is used to make the theta-theta map. The second used a standalone Python implementation of theta-theta mapping provided by Tim Sprenger. This was used for incoherent theta-theta mapping, where the entire dynamic spectrum is used to make the theta-theta map.

3.2.1 Physical Significance of the Theta-Theta Map

For a given pixel with coordinates (θ_1, θ_2) in the theta-theta map, the intensity of the pixel is given by the intensity of pixels in the secondary spectrum that correspond to light received from the interference between rays from screen positions θ_1 and θ_2 . If we consider the brightness distribution $B(\theta)$ that gives the intensity of light received from position θ on the screen, we can think of the theta-theta map as the outer product of $B(\theta)$ with itself. Hence, one way to recover the underlying brightness distribution $B(\theta)$ is to find the eigenvector of the theta-theta map that corresponds to the largest eigenvalue (Baker et al., 2022).

3.3 Curvature Search Algorithms

If one already has determined a guess of η , then theta-theta mapping is a useful tool for testing whether the guess is accurate. However, the repeated application of theta-theta mapping with a range of η can also be used on its own to find η . One way to do this is simply by performing theta-theta mapping with a range of η and then visually inspecting the resulting maps to find which η gives closest to horizontal and vertical lines. Fortunately, Baker et al. (2022) have developed an automated algorithm for measuring curvature with higher precision than is possible using a guess-and-check method. These methods use the principle that the brightness distribution $B(\theta)$ can be modeled as the dominant eigenvector of the theta-theta map.

If we perform theta-theta mapping with a guess of η , we can find the dominant eigenvector and create a model theta-theta map using the outer product of the eigenvector with itself. If we make a good guess of η , then the model represented by the dominant eigenvector will correspond well with the physical reality. Baker et al. (2022) use the model theta-theta map to construct a model dynamic spectrum, and then compare the model dynamic spectrum to the observed dynamic spectrum through a chi-squared analysis. In this procedure, the value of η that minimized the chi-squared value is taken to be the best guess of η . This lowest

value can be found by fitting a parabola to the chi-squared values as a function of η , as a this is more likely to correspond to a physical best-fit for η than simply taking the minimum value of the chi-squared. Another method for finding the best-fit η is, instead of finding the chi-squared value, to simply save the largest eigenvalue of the theta-theta map. A peak in the distribution of max eigenvalues as a function of η can then be used to find the maximized largest eigenvalue, which corresponds to the best-fit η .

To improve the precision of the curvature search, it is important that images on the screen do not move much over the course of the observation. It is also important that curvature not vary much in an observation. Of the two, curvature variation is a larger problem, as our observation spans a range of frequencies, and arc curvature is expected to vary with frequency. To account for this, Baker et al. (2022) divide the dynamic spectrum into “chunks” with much smaller frequency ranges (and, if necessary, smaller time ranges), performing an arc curvature search on each chunk.

By dividing each observation into chunks, we then obtain many arc curvature measurements for each observation. With 144 observations of PSR B1737+13, we quickly require an efficient way to sift through the various measurements and identify where our search algorithm has returned plausible measurements and where it has failed to accurately find curvature. To do this, we use a ranking scheme to identify, by eye, the highest quality measurements. The ranking scheme ranks each arc curvature measurement (corresponding to a single chunk of one observation) from 0-5 as follows:

- 0: The search algorithm has failed to find a curvature measurement, and no estimate is available.
- 1: The search algorithm has found a curvature measurement, but the measurement is clearly flawed and unphysical.
- 2: The search algorithm has returned a curvature measurement, but the measurement does not appear accurate.

- 3: The search algorithm has returned a curvature measurement, but the fitting process has clearly missed a different peak in the chi-squared/max eigenvalue distribution that would have been more accurate.
- 4: The returned curvature measurement appears to be plausible, although it may lack some precision.
- 5: The returned curvature measurement appears to be a highly accurate measurement.

For the purposes of our current investigation, only the measurements that were coded as 4 or 5 were used for further analysis.

The full procedure for using curvature search algorithms to measure η is outlined as follows:

1. Take one observation and divide the dynamic spectrum into 32 chunks 64 pixels wide in frequency and spanning the full time range of the observation.
2. For each chunk, use the curvature search algorithm (either the chi-squared method or the largest eigenvalue method) as proposed by Baker et al. (2022) as implemented in Scintools.
3. Save the best-fit η from the measurement, as well as the distribution of chi-squared values or max eigenvalues as a function of η . Also save a summary plot of the process displaying the distribution with fit and dynamic spectra, secondary spectra, and theta-theta map side-by-side with model versions for visual inspection. An example of such a plot is shown in Figure XXX.
4. Repeat steps 2-3 for all 32 chunks, and repeat the process for all 144 observations.
5. Manually review each arc curvature measurement, using the summary plot to assign each measurement a score 0-5 according to the ranking scheme outlined above.
6. Save the observations that scored 4-5 for further analysis.

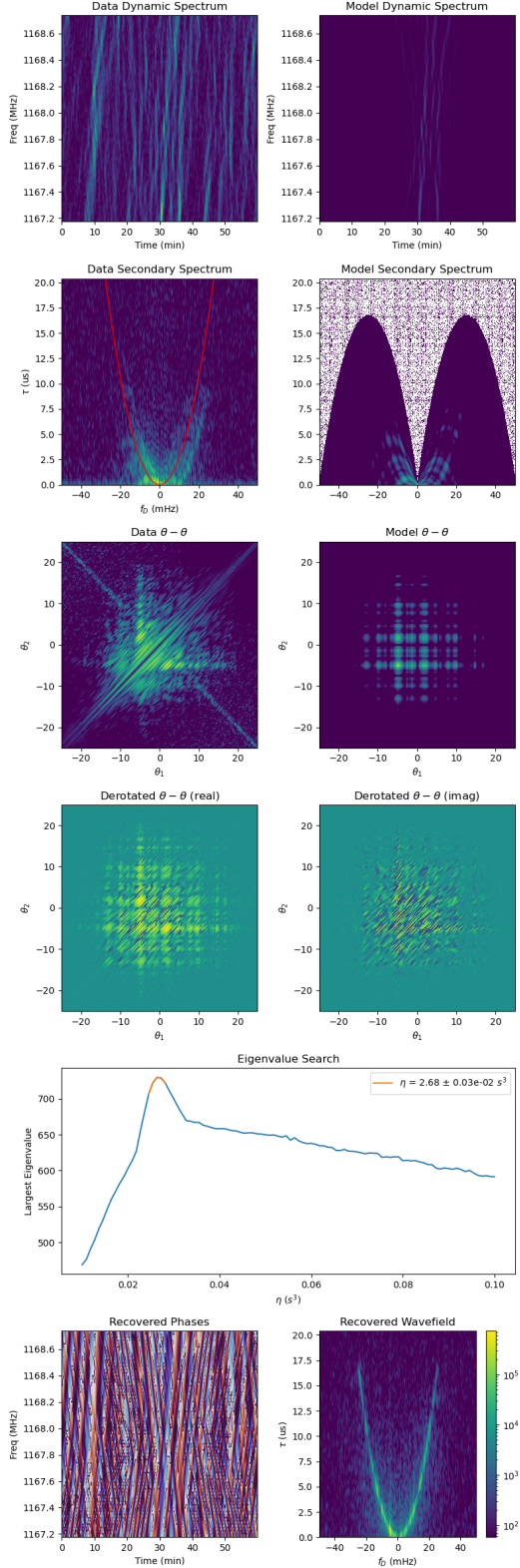


Figure 3.4: Example of a summary plot for a curvature search algorithm measurement. The second-to-bottom row shows the largest eigenvalue distribution as a function of η , with the fit to the peak shown. This was used, along with the secondary spectrum and theta-theta map, to assign a score of 5 to this measurement.

Chapter 4

Simulating Scintillation

Our aim in using simulations was, first, to better understand the dynamics of two-screen scintillation, and, second, to model the PSR B1737+13 system in order to better constrain its physical parameters. We made use of two different simulation frameworks, which are outlined in the sections that follow. First, we used the Screens Python package developed by Marten van Kerkwijk and Rik van Lieshout (2022). Additionally, we developed Python code to model two screen systems using the mathematical framework developed by Sprenger et al. (2022). I will outline the two frameworks in the sections that follow, with a focus on how each approach finds τ and f_D at the observer. In the last section, I will then show how dynamic spectra are generated from the wavefield, as this process is the same for both frameworks.

4.1 Screens Package

4.1.1 Code Framework

The Screens package provides an object-oriented framework for modeling observations of pulsars with scattering from screens. They take advantage of Python classes, using different classes to represent different objects in a Earth-screen(s)-pulsar system and make use of the

Astropy package for handling units and coordinate transformations (Astropy Collaboration et al., 2022). The parent class for all of these objects is the `Source` class, which defines any object that can be observed. Each source can have an associated position and velocity specified by Astropy’s `CartesianRepresentation` as well as a magnification used to indicate the relative brightness of the source. The pulsar is specified by an instance of the `Source` class.

Inheriting from the `Source` class is the `Screen` class. This class represents a collection of images of a particular source of radiation. With the `Screen` class, we can specify the position, velocity, and magnification of *each* image in the screen using arrays. The `Screen` class also allows us to specify the source of the radiation that gives rise to the images, as well as the screen’s distance from the source.

Two classes inherit from the `Screen` class. The `Telescope` class represents the observer; here we specify the telescope’s position and velocity. The `Screen1D` class is used to represent our canonical one-dimensional lines of images in a scattering screen. In addition to specifying the position, velocity, and magnification of each image, we also specify the orientation of the line of images as a unit vector in the direction of the normal vector connecting the line of images and the line of sight.

The strength of the Screens package’s object-oriented framework is that it allows us to easily construct a system of pulsar, screen(s), and observer. It should be noted that, in an idealized scattering screen, the line of scattered images is continuous and given by a continuous brightness distribution. However, for simulations we must discretize the line of images into a finite number of points. The Screens package requires the user to specify the position of each image as a distance along the line from the origin of the normal vector. Magnification values are also specified for each point. For our simulations, we used complex-valued magnification values given by

$$\mu_j(x_j) = A(x_j)e^{i\phi_j} \quad (4.1)$$

where μ_j is the magnification of the j th image, $A(x_j)$ is the real-valued brightness distribution at the corresponding position x_j , and ϕ_j is a random phase drawn from a uniform distribution between 0 and 2π . All of the magnification values for a given screen are then normalized to have a total magnitude of unity.

4.1.2 Calculating τ and f_D

The Screens package is able to handle complex systems of pulsar, screens, and observer. It does this through an iterative approach that considers the system as a series of nested source and destination screens. For a given source screen and destination screen, the relative positions and velocities of each point in the source screen with respect to each point in the destination screen are calculated. Consider image j in the source screen and image k in the destination screen, with the screens separated by a distance D and r_{jk} giving the distance between image j and image k when projected onto the same plane. The time delay τ_{jk} associated with a ray of light traveling from image j to image k is given by

$$\tau_{jk} = \frac{D}{2c}\theta_{jk}^2, \quad (4.2)$$

where θ_{jk} is given as $\frac{r_{jk}}{D}$. Using the relative velocity \mathbf{v}_{jk} of the two images projected onto the same plane, we can also calculate the time derivative of delay, $\dot{\tau}_{jk}$:

$$\dot{\tau}_{jk} = \frac{v_{jk}}{c}\theta_{jk}. \quad (4.3)$$

For each pair of images, we can use this to calculate τ and $\dot{\tau}$ associated with these images, giving a total of $N_1 * N_2$ values each for τ and $\dot{\tau}$, where N_1 and N_2 are the number of images in the source and destination screens, respectively. To propagate these images on the destination screen to the next screen in a ray's path, we make what was our destination screen the new source screen and the new destination screen the next screen in the ray's path. So, when we consider image k in our new source screen and image l in our new destination

screen, we can again calculate τ and $\dot{\tau}$. However, we must also take into account that image k already has a τ and $\dot{\tau}$ associated with it. van Kerkwijk & van Lieshout (2022) treat τ and $\dot{\tau}$ as cumulative quantities, so that our new τ and $\dot{\tau}$ are given by:

$$\tau_{\text{acc}} = \tau_0 + \tau_{kl} = \tau_0 + \frac{D}{2c} \theta_{kl}^2 \quad (4.4)$$

and

$$\dot{\tau}_{\text{acc}} = \dot{\tau}_0 + \dot{\tau}_{kl} = \dot{\tau}_0 + \frac{v_{kl}}{c} \theta_{kl}, \quad (4.5)$$

where τ_0 and $\dot{\tau}_0$ are the τ and $\dot{\tau}$ associated with image k in the source screen.

Now, there are actually N_1 values of τ_0 and $\dot{\tau}_0$ for each image k in the source screen associated with rays propagated from each of the N_1 images in our original source screen. To deal with this degeneracy, we consider there to be not N_2 images in the new source screen, but $N_2 * N_1$ images, many of which share the same associated position with each other. But, each of these images has a unique τ_0 and $\dot{\tau}_0$ associated with it. Thus, if there are N_3 images in the new destination screen, there are $N_3 * N_2 * N_1$ total unique τ and $\dot{\tau}$ values. If we then wish to propagate these images on the third screen to the fourth screen, we need to consider there to be $N_3 * N_2 * N_1$ images in the third screen. If we continue this process for M screens, our final destination screen will have $N_M * N_{M-1} * \dots * N_2 * N_1$ images.

To simplify this, rather than increasing the number of images with each successive screen, Screens in its backend considers all screens to have $N_M * N_{M-1} * \dots * N_2 * N_1$ images. Many of these images will share the same position, but each image will represent a unique ray path from source to destination, and as such will have a unique τ and $\dot{\tau}$. The advantage of this approach is that each possible ray path has an associated index, allowing us to vectorize our calculation of τ and $\dot{\tau}$. For a particular ray path i , with $i \in [1, N_M * N_{M-1} * \dots * N_2 * N_1]$, we can calculate τ_i and $\dot{\tau}_i$ as:

$$\tau_i = \sum_{j=2}^M \tau_{i,j-1,j} \quad (4.6)$$

and

$$\dot{\tau}_i = \sum_{j=2}^M \dot{\tau}_{i,j-1,j}, \quad (4.7)$$

where $\tau_{i,j-1,j}$ and $\dot{\tau}_{i,j-1,j}$ are the τ and $\dot{\tau}$ associated with a ray traveling from the i th image in screen $j - 1$ to the i th image in screen j .

There is just one more step before we can proceed further. We have τ for each image at our destination, but we do not have f_D . The Screens package does not calculate f_D directly, but recall that we can calculate f_D from $\dot{\tau}$ as

$$f_D = \nu \dot{\tau}, \quad (4.8)$$

where ν is the frequency of the wave.

4.2 Sprenger et. al. (2022) Version

In their analysis of B1508+55, Sprenger et al. (2022) develop their own model for describing two-screen scattering. Sprenger et al. (2022) use a model beginning from Kirchoff diffraction, which gives the electric field at a point with position p in the destination plane as a function by integrating over all possible paths from some point s in the source plane to p .

$$E(\mathbf{p}) = \frac{i}{\lambda} \int d^2 s \frac{e^{2\pi i \frac{d(\mathbf{p}, \mathbf{s})}{\lambda}}}{d(\mathbf{p}, \mathbf{s})} E(\mathbf{s}) \quad (4.9)$$

where $d(\mathbf{p}, \mathbf{s})$ is the distance between \mathbf{p} and \mathbf{s} . What interests us most is the phase term $e^{2\pi i d(\mathbf{p}, \mathbf{s})/\lambda}$, which is the phase shift experienced by the electric field as the wave travels from \mathbf{s} to \mathbf{p} . Since the perpendicular distance between the two planes is much larger than the extent of each plane, we can approximate $d(\mathbf{p}, \mathbf{s})$ to the first order as $(\mathbf{p} - \mathbf{s})^2/2D_{p,s}$, where $D_{p,s}$ is the perpendicular distance between the two planes. This then gives us the following

equation for following equation for electric field at \mathbf{p} :

$$E(\mathbf{p}) = \int d^2 s e^{i \frac{\pi \nu}{c} \frac{(\mathbf{p}-\mathbf{s})^2}{D_{p,s}}} E(\mathbf{s}) \quad (4.10)$$

When our source plane is the pulsar and our destination plane is the observer, then the phase shift is due only to the geometric distance between the pulsar and the observer. However, when we have a diffraction screen, an extra phase shift ϕ is accumulated due to this diffraction. For diffraction due to free electrons, as we have in the case of a scattering screen, the phase shift is given by the dispersion measure (DM) of the path of propagation crossing the screen at position \mathbf{x} :

$$\phi(\mathbf{x}) = -\frac{1}{4\pi\epsilon_0} \frac{e^2}{m_e c} \frac{DM(\mathbf{x})}{\nu} \quad (4.11)$$

Sprenger et al. (2022) generalize this situation to the case where a ray travels from pulsar to observer, being scattered en route by N screens. The phase shift experienced by the ray is then given by the sum of the geometric phase shift from traveling the total path length and the phase shift inflicted by diffractive scattering at each of the N screens. They also allow for all planes (including the pulsar, observer, and all N screens) to have some velocity with respect to a stationary reference frame, with position on the n th screen in this reference frame given by $\mathbf{X}_n = \mathbf{x}_n + \mathbf{V}_n t$, where \mathbf{x}_n is the (unmoving) position on the n th screen in its own frame and \mathbf{V}_n is the velocity of the n th screen with respect to the stationary reference frame.

In this formalism, we can write the total phase shift Φ experienced by a ray as:

$$\Phi(\mathbf{x}_0, \mathbf{x}_1, \dots, \mathbf{x}_{N+1}, t) = \sum_{n=1}^N \phi_n(\mathbf{x}_n) + \sum_{n=1}^{N+1} \frac{\pi \nu}{c} \frac{(\mathbf{x}_n - \mathbf{x}_{n-1} + (\mathbf{V}_n - \mathbf{V}_{n-1})t)^2}{D_{n-1,n}}. \quad (4.12)$$

Here $n = 0$ corresponds to the observer plane, and $n = N + 1$ corresponds to the pulsar plane. Thus, diffractive scattering only occurs at $n = [1, N]$, but the geometric phase shift is accumulated as the ray travels between each consecutive pair of planes. If we then wish to

find the electric field at the observer plane, we can use

$$E(\mathbf{x}_0, t) = \int e^{i\Phi(\mathbf{x}_0, \mathbf{x}_1, \dots, \mathbf{x}_{N+1}, t)} d^2x_1 d^2x_2 \dots d^2x_{N+1}. \quad (4.13)$$

Sprenger et al. (2022) then consider the case of a two-screen system, with observer plane position given by \mathbf{P} , pulsar plane position given by \mathbf{S} , the screen closer to the observer given by \mathbf{X} , and the screen closer to the pulsar given by \mathbf{Y} . They also assume the x and y screens to have one dimensional anisotropy of the sort that produces scintillation arcs, with the angles of the anisotropy relative to a fixed reference frame given by α_x and α_y . x_{\parallel} and y_{\parallel} give the components of screen position in the direction of the anisotropy, while x_{\perp} and y_{\perp} give the components of screen position in the direction perpendicular to the anisotropy. In this case, the phase shift experienced by the ray (with time dependence built in to our position coordinates) is given by:

$$\Phi = \phi_1(\mathbf{x}_{\parallel}) + \phi_2(\mathbf{y}_{\parallel}) + \frac{\pi\nu}{c} \left[\frac{(\mathbf{X} - \mathbf{P})^2}{D_{p,x}} + \frac{(\mathbf{Y} - \mathbf{X})^2}{D_{x,y}} + \frac{(\mathbf{S} - \mathbf{Y})^2}{D_{y,s}} \right]. \quad (4.14)$$

After much algebraic manipulation, Sprenger et al. (2022) arrive at the following equation for Φ in the two-screen case:

$$\Phi(\theta_x, \theta_y, t) = \frac{\pi\nu}{c} (D_{\text{eff},x}\theta_x^2 - 2V_{\text{eff},x,\parallel}\theta_x t + D_{\text{eff},y}\theta_y^2 - 2V_{\text{eff},y,\parallel}\theta_y t - 2D_{\text{mix}}\theta_x\theta_y + Kt^2), \quad (4.15)$$

where we have introduced the parameters $\theta_x = x_{\parallel}/D_{p,x}$ and $\theta_y = y_{\parallel}/D_{p,y}$ as with the one-screen case. The effective terms $D_{\text{eff},x}$, $D_{\text{eff},y}$, $V_{\text{eff},x,\parallel}$, $V_{\text{eff},y,\parallel}$, and D_{mix} are also used to mimic the one-screen case, but are much more complicated:

$$D_{\text{eff},x} = \frac{D_{p,s}D_{p,x}D_{p,y}}{D_{p,y}D_{x,s} - D_{p,x}D_{y,s}\delta^2}, \quad (4.16)$$

$$D_{\text{eff},y} = \frac{D_{p,s}D_{x,s}D_{p,y}^2/D_{y,s}}{D_{p,y}D_{x,s} - D_{p,x}D_{y,s}\delta^2}, \quad (4.17)$$

$$V_{\text{eff},x,\parallel} = \frac{-D_{p,s}D_{p,y}V_{x,\parallel} + \delta D_{p,x}D_{p,s}V_{y,\parallel} + \gamma\delta D_{p,x}D_{y,s}V_{p,\perp} + \gamma D_{p,x}D_{p,y}V_{s,\perp}}{D_{p,y}D_{x,s} - D_{p,x}D_{y,s}\delta^2} + V_{p,\parallel}, \quad (4.18)$$

$$V_{\text{eff},y,\parallel} = \frac{-D_{p,s}D_{x,s}D_{p,y}V_{y,\parallel}/D_{y,s} + \delta D_{p,y}D_{p,s}V_{x,\parallel} - \gamma D_{p,y}D_{x,s}V_{p,\perp} - \gamma\delta D_{p,x}D_{p,y}V_{s,\perp}}{D_{p,y}D_{x,s} - D_{p,x}D_{y,s}\delta^2} + \frac{D_{p,y}V_{s,\parallel}}{D_{y,s}}, \quad (4.19)$$

$$D_{\text{mix}} = \frac{\delta D_{p,x}D_{p,y}D_{p,s}}{D_{p,y}D_{x,s} - D_{p,x}D_{y,s}\delta^2}. \quad (4.20)$$

Here, we have $\gamma = \sin(\alpha_x - \alpha_y)$, $\delta = \cos(\alpha_x - \alpha_y)$, and K is a constant that is not dependent on the screen positions and so is irrelevant for our further analysis.

For our simulations, our primary interest is in finding the τ and f_D of a particular ray passing through θ_x and θ_y . To do this, Sprenger et al. (2022) use the definition of the τ and f_D through a Fourier transform to find

$$\tau = \left. \frac{\partial \Phi}{2\pi\partial\nu} \right|_{t=0}, \quad (4.21)$$

$$f_D = \left. \frac{\partial \Phi}{2\pi\partial t} \right|_{t=0}. \quad (4.22)$$

Using these expressions, we arrive at equations for τ and f_D in the two-screen case as a function of θ_x and θ_y :

$$\tau(\theta_x, \theta_y) = \frac{1}{2c} (D_{\text{eff},x}\theta_x^2 + D_{\text{eff},y}\theta_y^2 - 2D_{\text{mix}}\theta_x\theta_y), \quad (4.23)$$

$$f_D(\theta_x, \theta_y) = -\frac{\nu}{c} (V_{\text{eff},x,\parallel}\theta_x + V_{\text{eff},y,\parallel}\theta_y). \quad (4.24)$$

Thus, if we set up our two scattering screens in the same way as the Screens package (i.e.: discrete images in the x and y screens), we can use these equations to find the τ and f_D associated with each possible combination of images in the x and y screens, for N_x and N_y total images.

4.3 Finding Dynamic Spectra from the Wavefield

We have shown that we can use either framework to arrive at the wavefield. While Screens works with n screens, we will only consider the two-screen case. Suppose we want to find the dynamic spectrum of a pulsar whose light is scattered by screens Y and X on its way to us. We can define N_y images in the Y , each with an associated position and magnification, with the magnification determined using a method such as that given by Equation 4.1. We can then define N_x images in the X screen in a similar manner. We can then find τ and f_D using either framework, with $N_x N_y$ points for each. For path j , the intensity of the wavefield corresponding to τ_j and $f_{D,j}$ values is $\mu_j = \mu_{j,x} \mu_{j,y}$: the product of all magnifications on path j . We can then use the wavefield to reverse-engineer the dynamic spectrum. For a particular point (t, ν) , we can find the electric field at the observer as

$$E(t, \nu) = \sum_{j=1}^{N_x N_y} \mu_j \exp [2\pi i (f_{D,j} t + \tau_j \nu)]. \quad (4.25)$$

The dynamic spectrum is then the intensity of the electric field,

$$S(t, \nu) = |E(t, \nu)|^2. \quad (4.26)$$

Chapter 5

A 36-Epoch Observation of Pulsar B1737+13

5.1 Characterizing the Data Set

Observations of pulsar B1737+13 were made using the Arecibo telescope in Puerto Rico by Daniel Hemberger (Oberlin College '07) and Dan Stinebring, mostly remotely. The data set consists of 36 epochs of observations over a period of 38.5 weeks, with the first observation on 5 April 2006 (MJD 53830) and the last on 31 December 2006 (MJD 54100). Observations were 1 hour long and were made in 4 different frequency bands—1175 MHz, 1380 MHz, 1425 MHz, and 1470 MHz—using the L-wide feed and the WAPP spectrometers.¹ Each frequency band was 50 MHz wide, and the WAPP spectrometers were used with 2048 channels, giving a channel width of 24.4 kHz (Hemberger & Stinebring, 2008). The data were then split into 360 time bins with subintegration times of 10 seconds, with the off-pulse signal subtracted from the on-pulse signal before the signal was integrated over the 10 second time bin to produce a dynamic spectrum. The 144 dynamic spectra from each observation were stored as individual FITS files.² This same dataset was previously studied by Hemberger & Stinebring

¹Information about the WAPP can be found at <http://naic.edu/~wapp/>

²FITS documentation can be found at <https://fits.gsfc.nasa.gov/>

(2008).

From the first epoch of observation at MJD 53830, a well-resolved scintillation arc is visible. We also see a clear inverted arclet substructure. The arc is also more or less symmetric. All of these factors would appear to indicate that we are viewing scattering from a single screen, with little else that could be contributing to the scattering. Beginning at around MJD 53880, we see the scintillation arc become wider, and the arc becomes more asymmetric. During this time, we also see the inverted arclet substructure become less prominent. By MJD 53899, the primary arc has become more diffuse and only a few signs of inverted arclets remain. As time progresses, the inverted arclets disappear entirely and the primary arc becomes blurred out and fuzzy, with the fuzziness beginning on the left side of the arc at MJD 53894 and reaching the origin a few epochs later. We also see the fuzziness spread out over a larger area, making the arc appear more distorted. At MJD 54019, we do not even see an arc; we see only a region of power at the origin. At MJD 54036, however, the arc begins to reemerge. The arc then becomes less fuzzy over the next few epochs. At MJD 54083, we even see signs of inverted arclets returning on the left side of the arc. However, the secondary spectrum does not return to its original state for the remainder of the observation period.

The evolution of the secondary spectrum is illustrated in Figure 5.1 with four epochs spaced throughout the observation period. The secondary spectra from all 36 epochs of observation are shown for the 1175 MHz band, the 1380 MHz band, the 1425 MHz band, and the 1470 MHz band in Figures 5.2, 5.3, 5.4, and 5.5, respectively.

5.2 Measured Curvatures

As noted previously, there is a clear primary arc throughout the dataset that is well resolved in some epochs. Establishing the curvature of this arc is described in Section 5.2.1. However, we also wished to investigate the existence of any other arcs present in the sec-

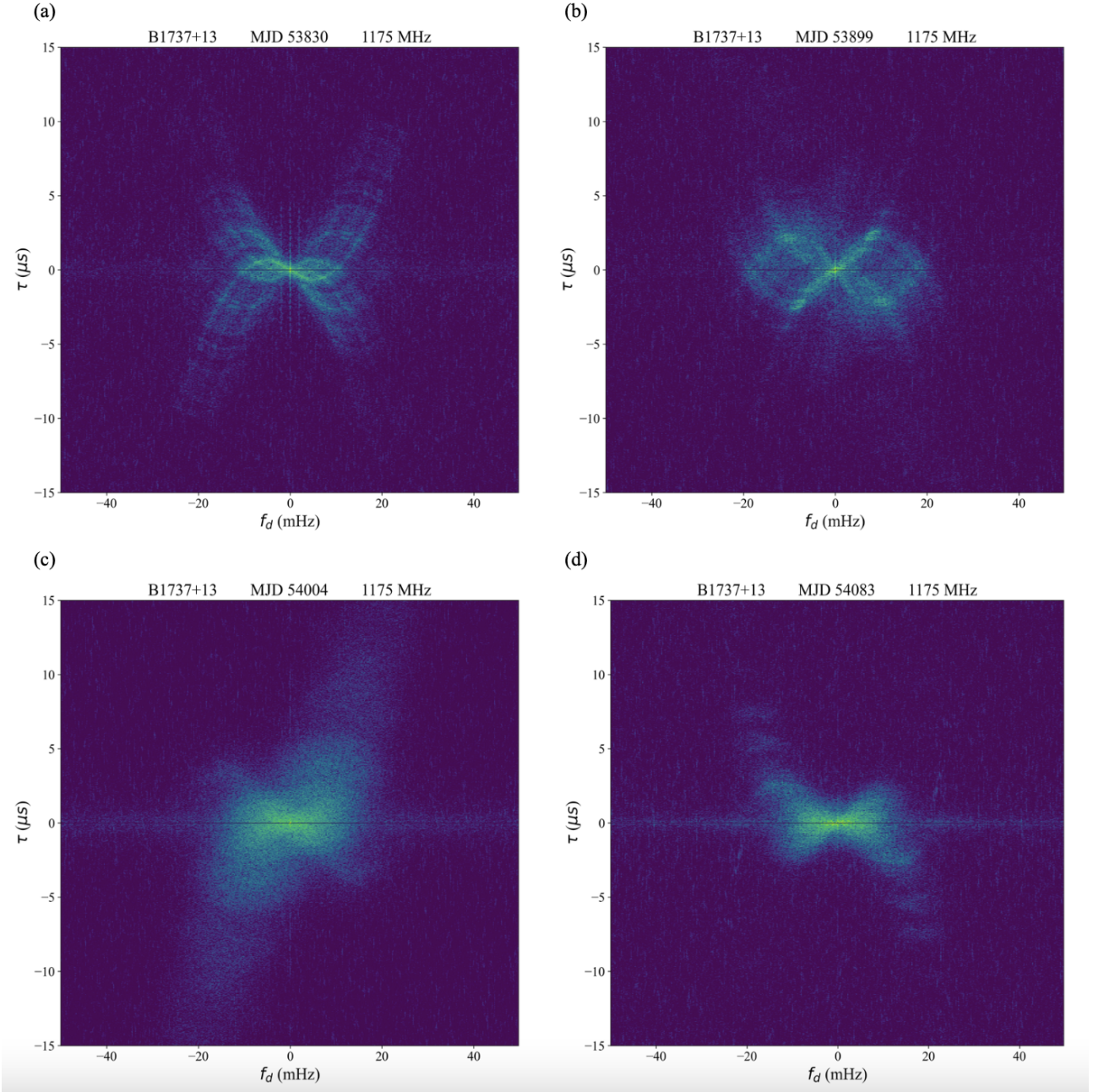


Figure 5.1: Secondary spectra from four epochs of observation of pulsar B1737+13 in the 1175 MHz band. In panel (a), at MJD 53830, a scintillation arc is well resolved and shows inverted arclet structure. In panel (b), at MJD 53899, the inverted arclets are still present, but the scintillation arc has become more diffuse. In panel (c), at MJD 54004, the inverted arclets are no longer visible, and the scintillation arc is even more diffuse. In panel (d), at MJD 54083, the scintillation arc has become less diffuse, and signs of inverted arclets are visible again.

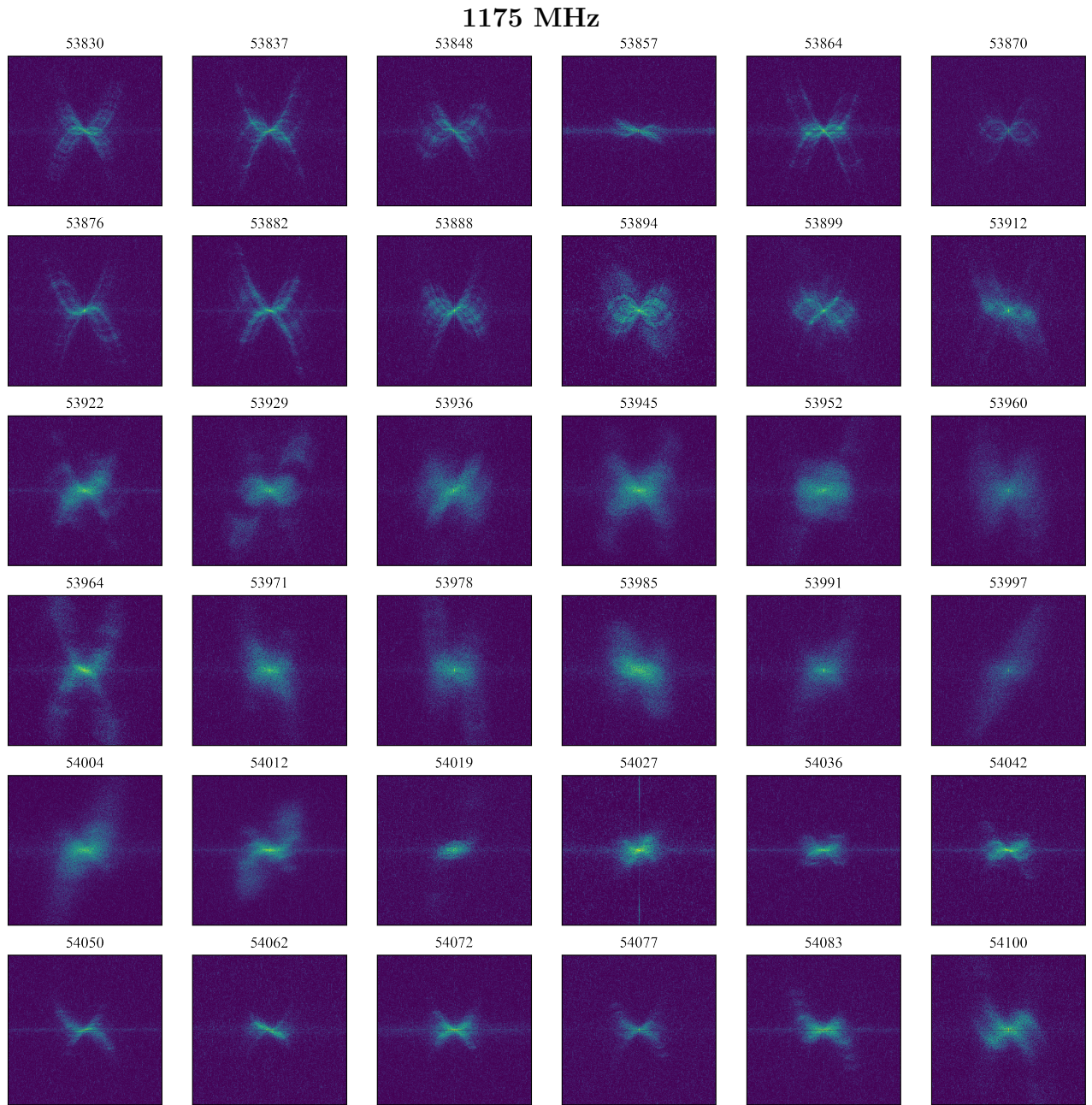


Figure 5.2: Secondary spectra from all 36 epochs of observation of pulsar B1737+13 in the 1175 MHz band. Corresponding dates of each observation are given above in MJD. All axes are scaled the same running from $-15 \mu\text{s}$ to $15 \mu\text{s}$ in τ and -40 mHz to 40 mHz in f_d . Intensity is scaled logarithmically, and each spectrum is normalized differently.

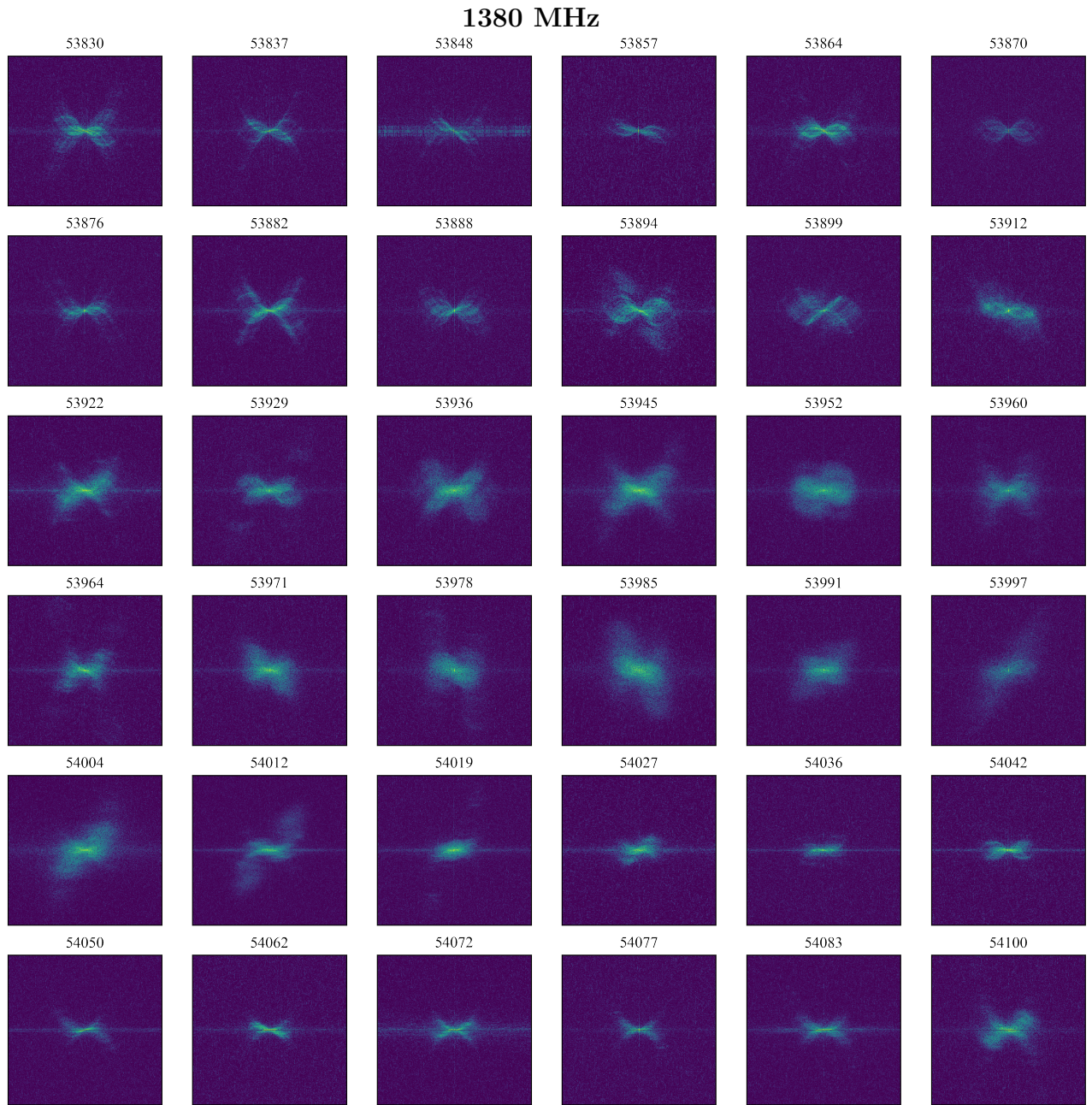


Figure 5.3: Secondary spectra from all 36 epochs of observation of pulsar B1737+13 in the 1380 MHz band. Corresponding dates of each observation are given above in MJD. All axes are scaled the same running from -15 μ s to 15 μ s in τ and -40 mHz to 40 mHz in f_d . Intensity is scaled logarithmically, and each spectrum is normalized differently.

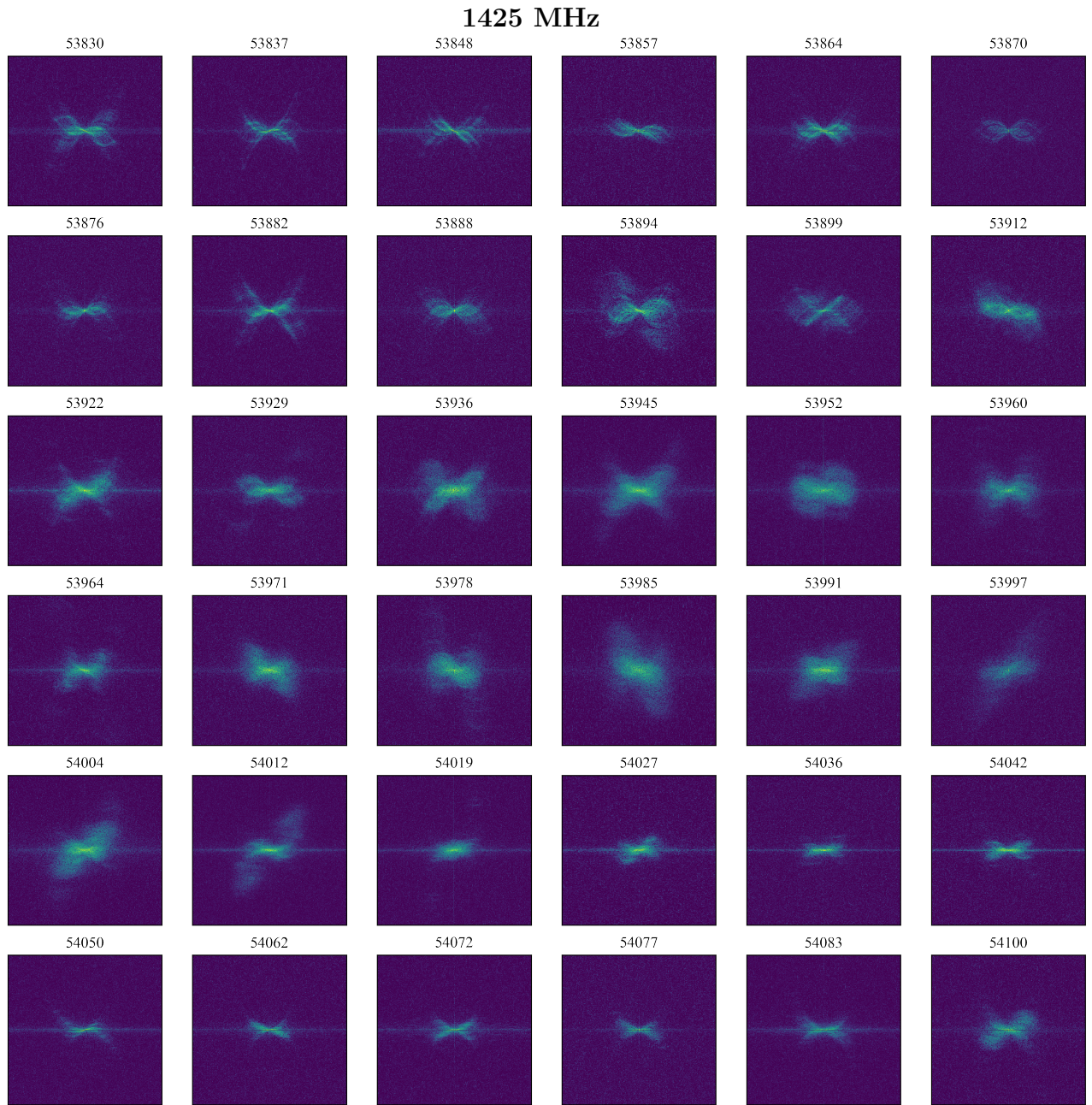


Figure 5.4: Secondary spectra from all 36 epochs of observation of pulsar B1737+13 in the 1425 MHz band. Corresponding dates of each observation are given above in MJD. All axes are scaled the same running from $-15 \mu\text{s}$ to $15 \mu\text{s}$ in τ and -40 mHz to 40 mHz in f_d . Intensity is scaled logarithmically, and each spectrum is normalized differently.

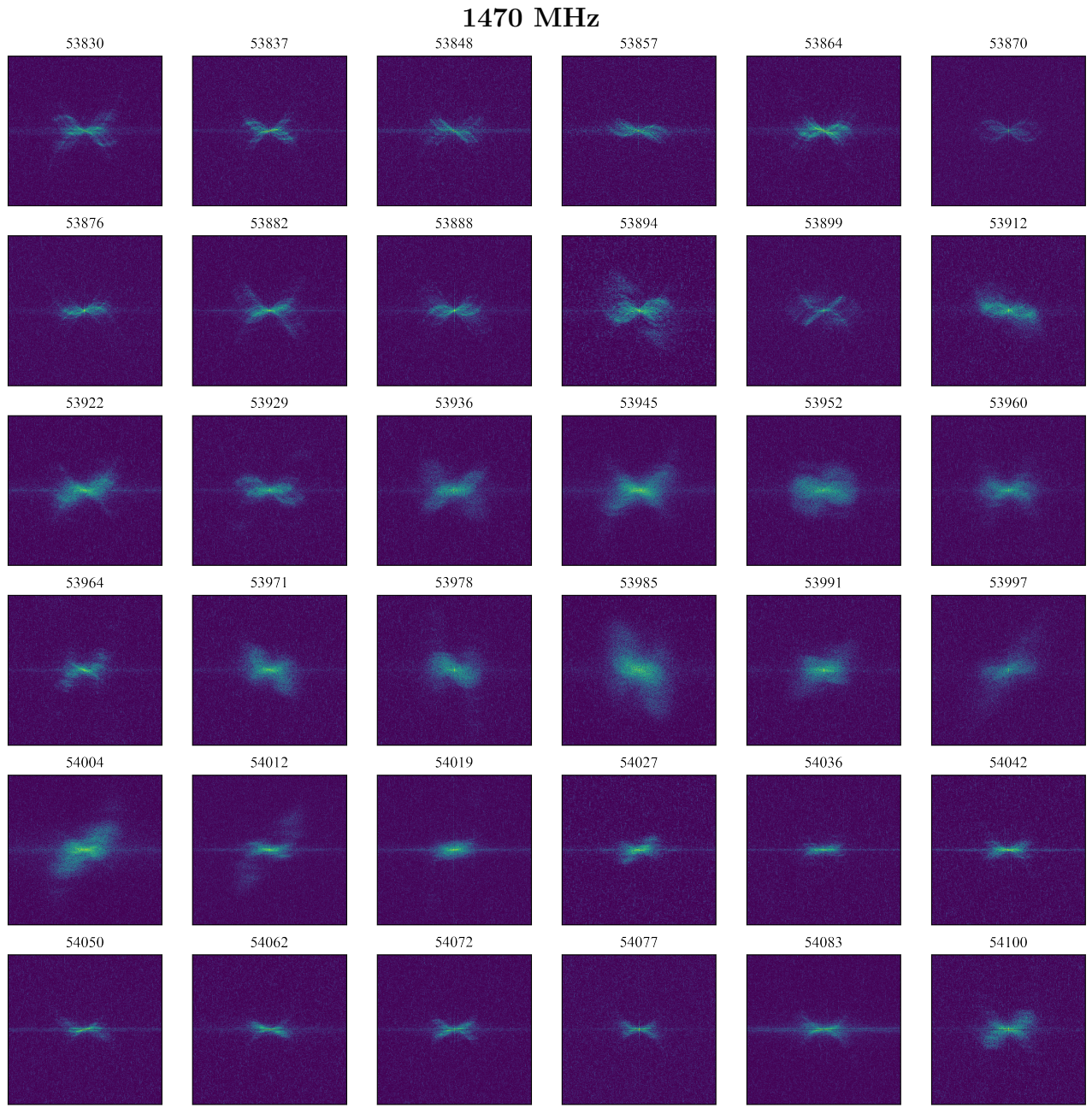


Figure 5.5: Secondary spectra from all 36 epochs of observation of pulsar B1737+13 in the 1470 MHz band. Corresponding dates of each observation are given above in MJD. All axes are scaled the same running from $-15 \mu\text{s}$ to $15 \mu\text{s}$ in τ and -40 mHz to 40 mHz in f_d . Intensity is scaled logarithmically, and each spectrum is normalized differently.

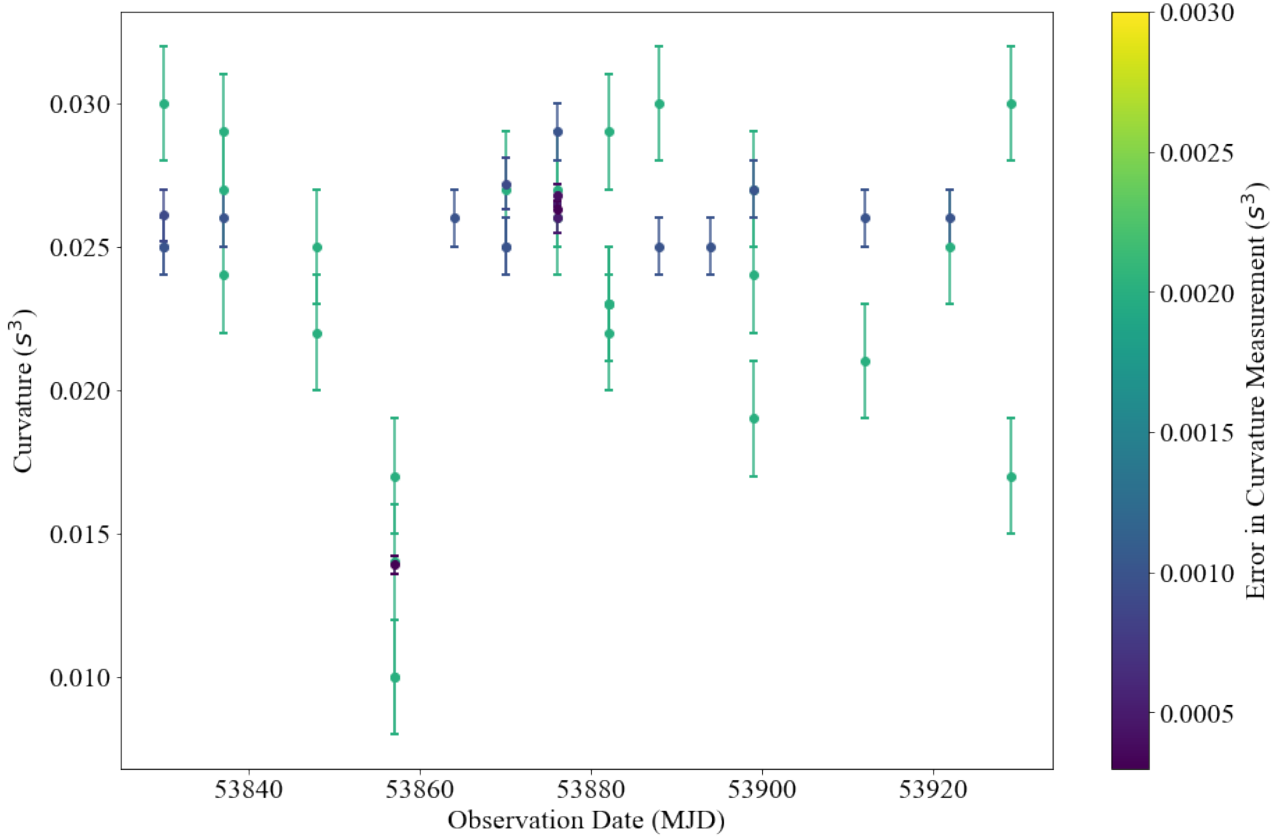


Figure 5.6: Manually measured curvatures of the primary arc in the 1175 MHz band for the first 14 epochs of observation. Error bars are shown with the color indicating the relative size of the error, with error determined by the width in τ corresponding to between 1 and 3 cursor movements, depending on the resolution of the feature being measured.

ondary spectrum that could indicate the presence of an additional scattering screen. This measurement process is described in Section 5.2.2.

5.2.1 Primary Arc

Primary arc curvature was measured manually as described in Section 3.1. Uncertainty in the curvature measurement was determined by the width in τ corresponding to at least one and up to three of the smallest possible movements of the cursor. One cursor movement was used for the features that were easily resolved, while three cursor movements were used for the features that were not as easily resolved. The results are shown in Figure 5.6 for the 1175 MHz band, which had the best resolution of any band. Arc curvature measurement was

only performed for the first 14 epochs of observation, as the arc was not resolved enough in subsequent epochs for a clear identification by eye. There is a clear outlier with epoch 3 (with the first epoch being epoch 0) at MJD 53857, which has a measured curvature much lower than the rest of the data. It has been previously suggested that this epoch may have been mislabeled in frequency, resulting in an arc with an incorrect curvature when treated to be also in the 1175 MHz band³. If we treat this epoch as an outlier, the remaining measurements have an average curvature of $0.0262 \pm 0.0002 \text{ s}^3$ at 1175 MHz.

We also measured the curvature of the primary arc using a curvature search algorithm as described in Section 3.3. Both the largest eigenvalue method and the smallest chi-squared method were used with a chunk size of 64 frequency channels. This divided each observation into 32 chunks of bandwidth 1.56 MHz, which was small enough to precisely measure arc curvatures since curvature remained roughly constant over a single chunk. The error associated with a curvature measurement was taken from the best-fit for a parabola around a peak in either the largest eigenvalue or chi-squared distribution; the standard deviation of the fit parameter corresponding to the η value of the parabola apex was used as the error.

Since the primary arc was the most prominent feature in our secondary spectra, the curvature search algorithm was able to measure it with greater precision and accuracy than other features. As such, secondary spectra in which the primary arc was well resolved were often given a score of 5, whereas secondary spectra with worse resolution or other features were not given scores higher than 4. As a result, we used only measurements with a score of 5 to find the curvature of the primary arc using this method. Measured curvature is shown as a function of frequency in Figure 5.7 for the 1175 MHz band. Because we expect arc curvature to have a $\frac{1}{\nu^2}$ dependence, we fit for such a relationship and found a best-fit curvature of

$$\eta_{1175 \text{ MHz}} = 0.0267 \pm 0.0001 \text{ s}^3$$

³Private communication with Robert Main.

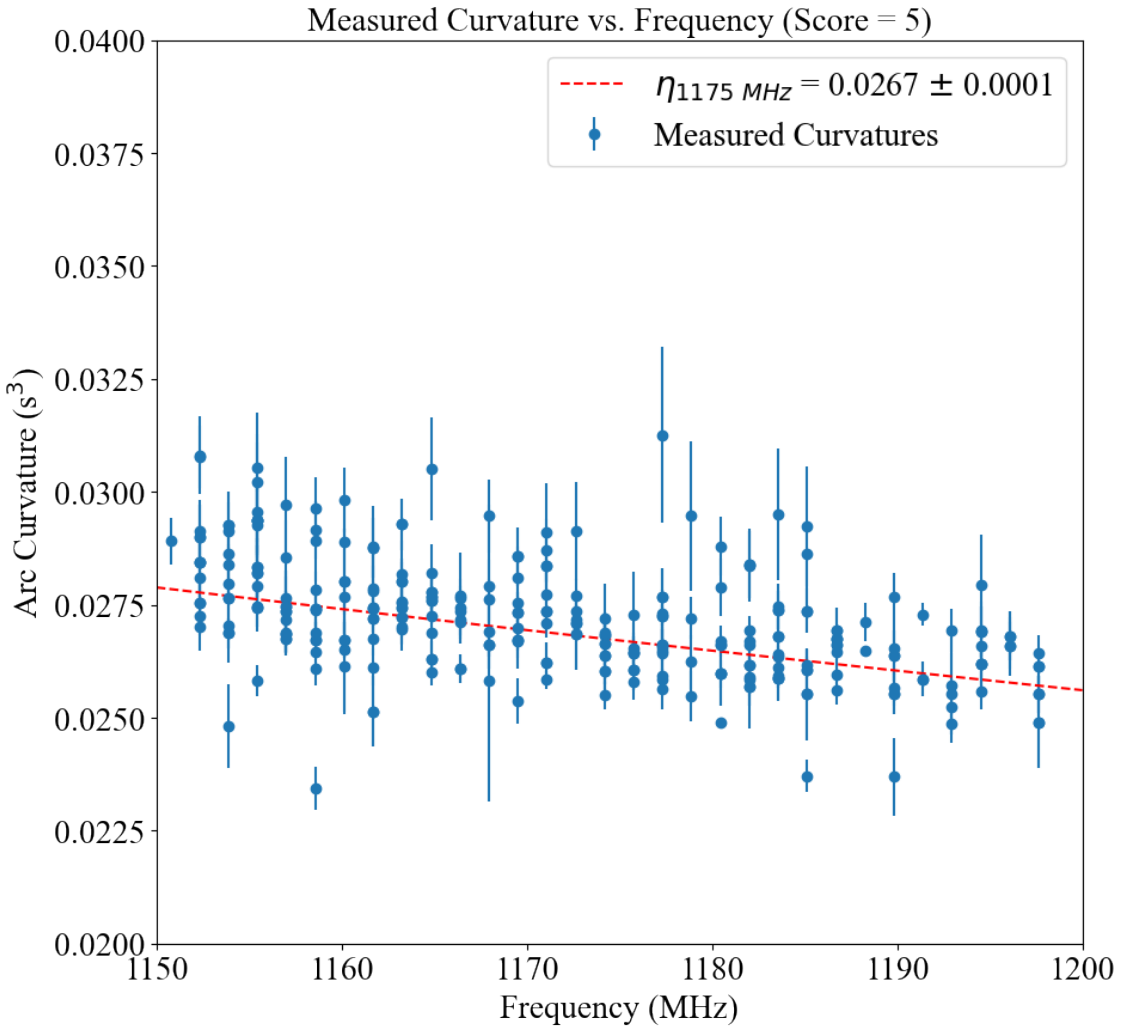


Figure 5.7: Measured curvatures using the curvature search algorithm in the 1175 MHz band that were given a score of 5. The measurements are shown as a function of frequency and span all epochs. The dotted red line shows the best fit curvature assuming a ν^{-2} frequency dependence, which was found to be $0.0267 \pm 0.0001 \text{ s}^3$.

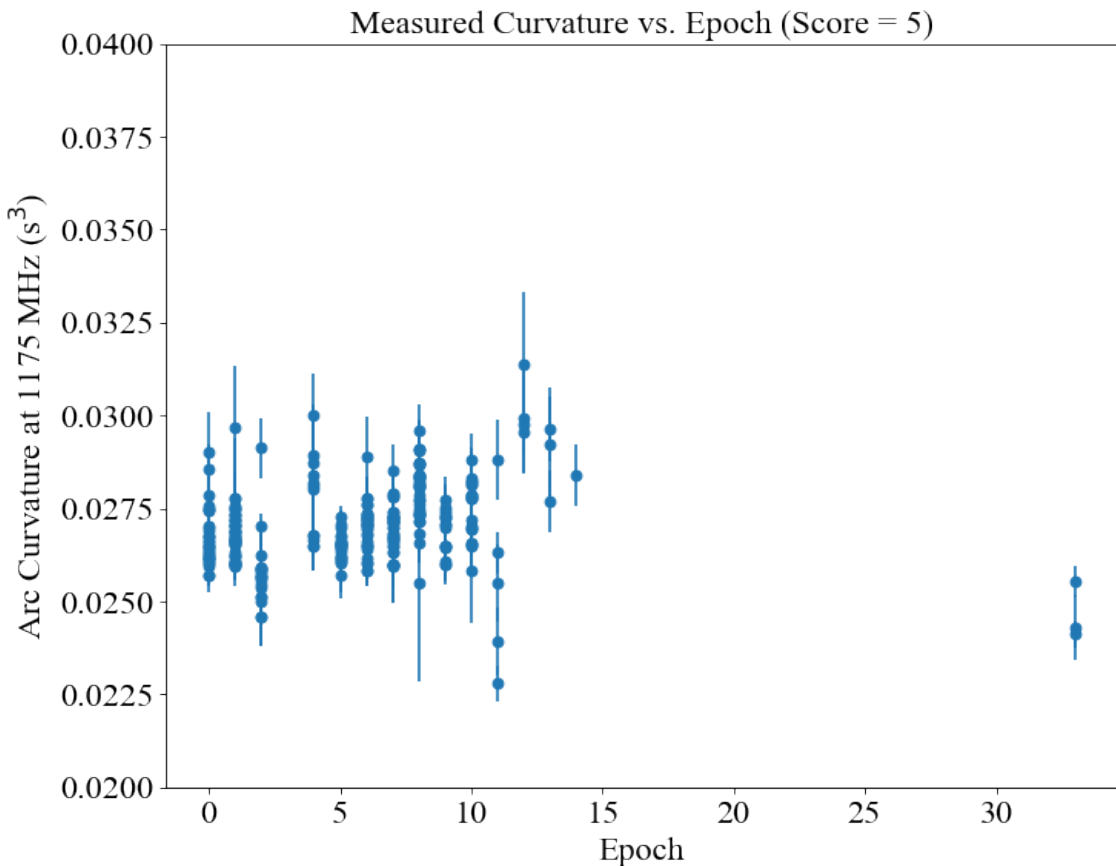


Figure 5.8: Measured curvatures using the curvature search algorithm in the 1175 MHz band that were given a score of 5. The measurements are shown as a function of epoch and span Epochs 1 through 35. Arc curvature measurements remain fairly constant for these measurements, consistent with a primary arc. Exceptions are epochs 2, 11, and 35, which appear to have smaller curvatures. No measurements were scored 5 for epoch 3 and epochs 15 through 34, consistent with the arc not being resolved in these epochs.

at 1175 MHz. This is consistent with the manually measured curvature.

Figure 5.8 shows the measured curvatures that were given a score of 5 as a function of epoch for the 1175 MHz band. Consistent with our observation that the primary arc becomes less resolved in later epochs, there were no measurements given a score of 5 for epochs 15 through 34. Of the measurements given a score of 5, the curvatures remain fairly constant, as we would expect with a primary arc. There are a few exceptions, however. Epochs 2, 11, and 35 appear to have smaller curvatures than the rest of the data. There also appears to be a suggestion of a curvature increase in epochs 12-14 coinciding with the increasing fuzziness of the arc.

From these measurements, the curvature of the primary arc is roughly between 0.026 and 0.027 s^3 at 1175 MHz. This represents a scattering screen located at least 2.5 kpc from Earth along the line of sight. This scenario of one scattering screen describes the early epochs well, but is lacking when the primary arc becomes less resolved in later epochs to the point that it cannot be measured. Thus, in the next section we investigate the possibility of additional arcs.

5.2.2 Secondary Arc Curvatures

If we now consider measurements using our curvature search algorithm that were given a score of 4 or 5, we see all measurements that gave a plausible curvature measurement for a particular chunk of an observation. These measurements are shown in Figure 5.9 as a function of frequency for the 1175 MHz band. The majority of the measurements are consistent with the primary arc curvature, including the measurements given a score of 5. However, there are a large number of measurements that differ significantly from the primary arc curvature. These measurements complicate the picture of a single scattering screen.

More clarity can be gained by looking at the measurements as a function of epoch, as shown in Figure 5.10. In the first 14 or so epochs, the measurements are mostly consistent with the primary arc curvature. However, arc curvature appears to increase significantly

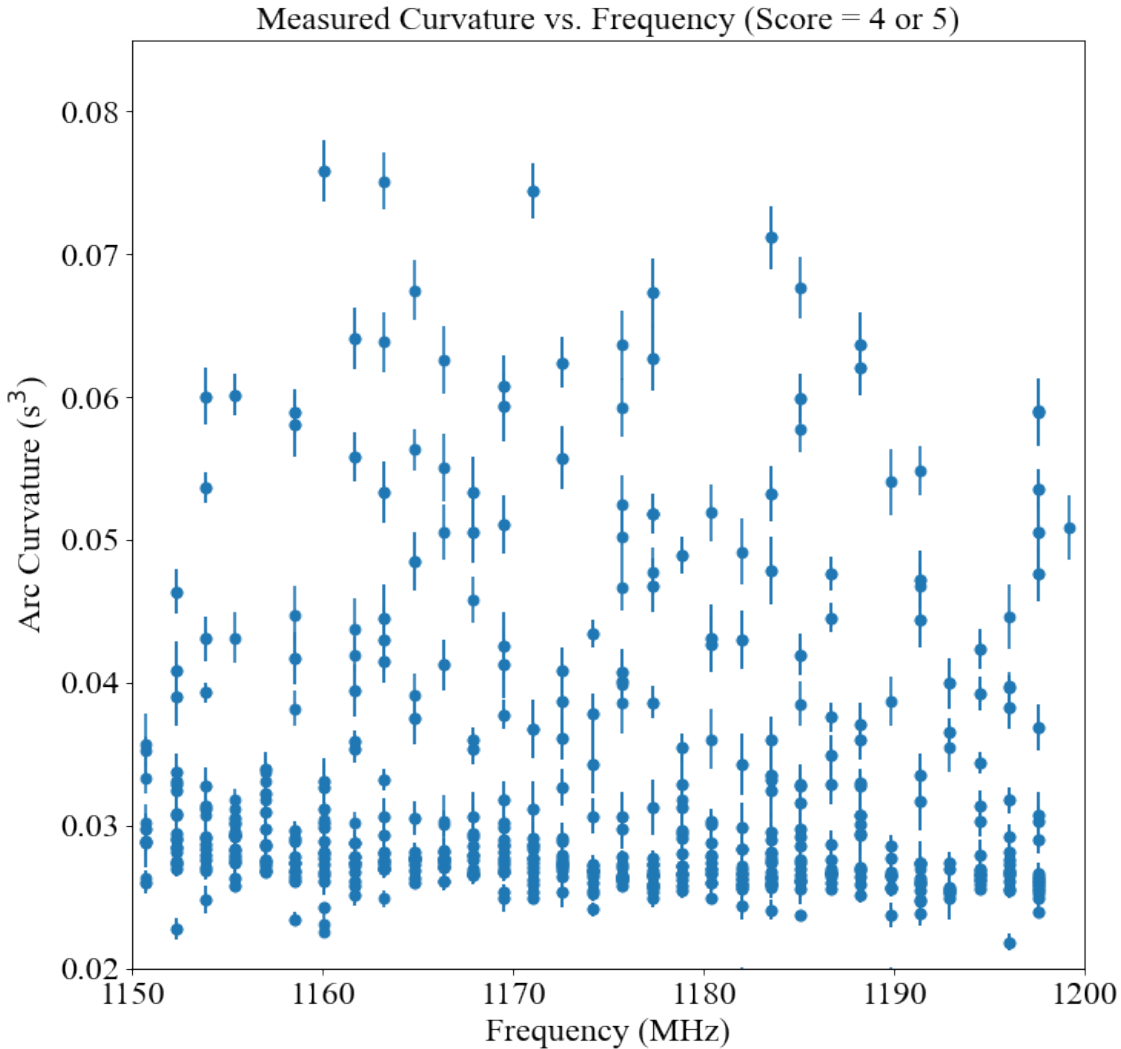


Figure 5.9: Measured curvatures using the curvature search algorithm in the 1175 MHz band that were given a score of 4 or 5, shown as a function of frequency and spanning all epochs. While most of the measurements are consistent with a primary arc, there are a large number that differ significantly from the primary arc curvature, indicating the presence of additional scattering structures.

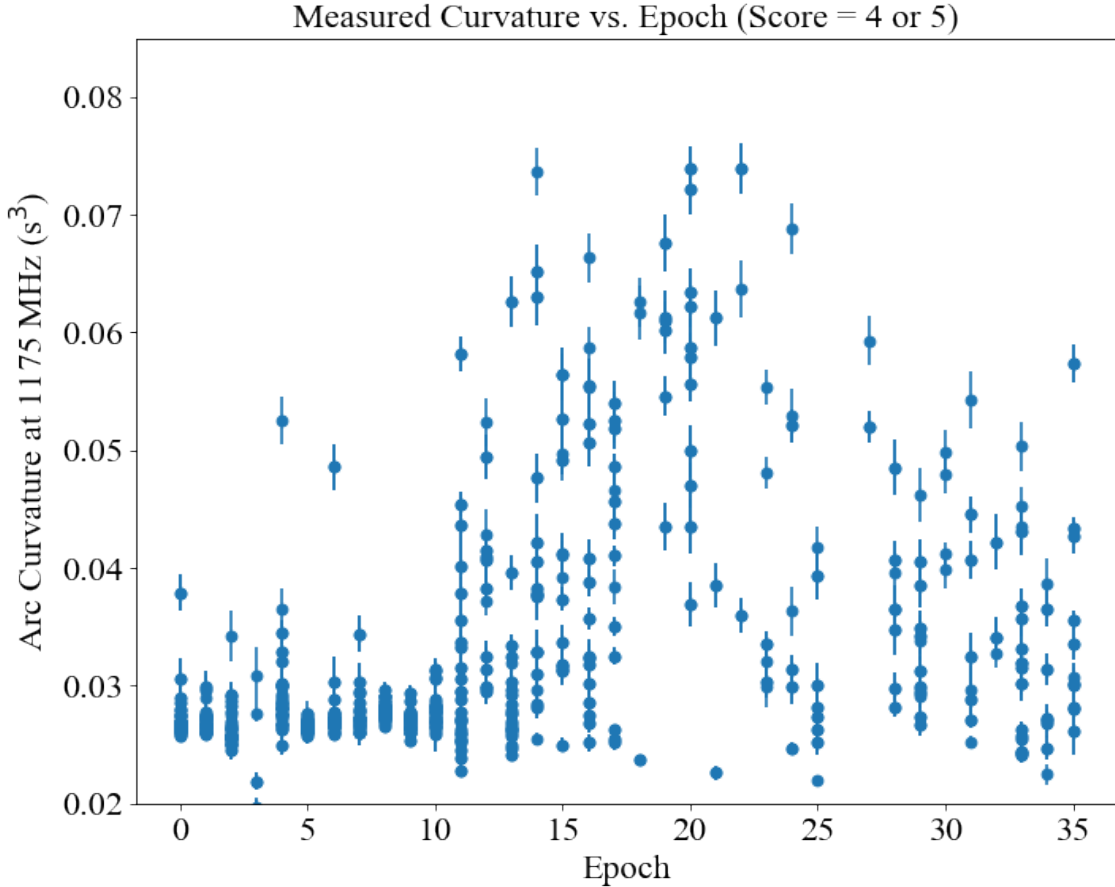


Figure 5.10: Measured curvatures using the curvature search algorithm in the 1175 MHz band that were given a score of 4 or 5, shown as a function of epoch. Measurements are consistently around the primary arc curvature for the early epochs. However, curvature measurements diverge from this pattern around epoch 15, with significantly higher curvature values of up to $0.07 s^3$ being measured. Towards the end of the observation, the curvature measurements become more consistent with the primary arc curvature, although some scatter remains.

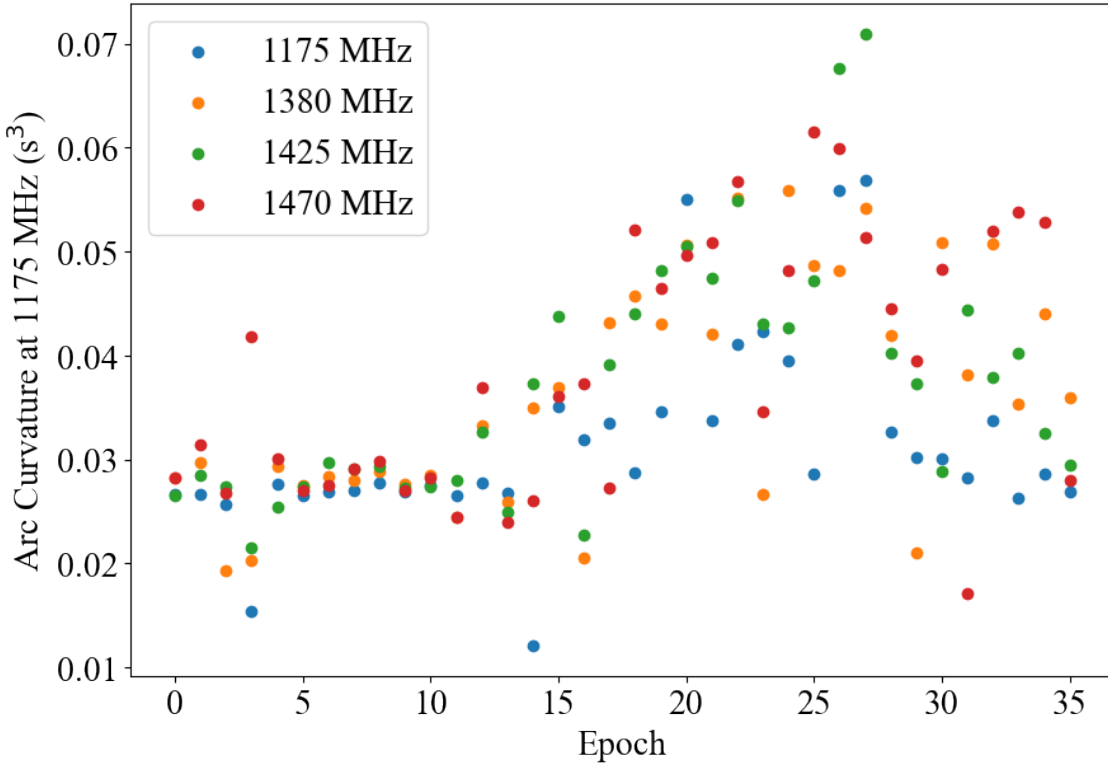


Figure 5.11: Curvature values for each epoch in each band, obtained by finding the best-fit curvature at 1175 MHz for a ν^{-2} dependence across a single observation. The overall trend for each band is fairly similar, although the three higher frequency bands have more scatter than the 1175 MHz band. The scattering event previously identified around epoch 15 is apparent in all four bands, although the three higher frequency bands increase in curvature before epoch 15 and reach higher curvature values than the 1175 MHz band.

around epoch 15. We find many curvature values of between 0.04 and 0.07 s^3 , with curvature increasing from epoch 15 to epoch 22 and then decreasing from epoch 22 to epoch 30. In the last few epochs, measurements return at the primary arc curvature value. This suggests that a scattering event took place around epoch 15 which is not consistent with one scattering screen.

Thus far, we have treated different chunks of an observation as, roughly speaking, independent measurements at different frequencies. That is, each chunk could be treated as a separate observation of potentially different scattering structures. However, treating each chunk in an observation as reflecting the same scattering structure can help constrain arc curvature for a particular observation. This can be done by performing a best fit of arc

curvature as a function of frequency across a single observation, obtaining a single curvature value for each observation. To perform these fits, we disregarded the scores assigned to observations and weighted each fit according to the error in each curvature measurement. The results of these fits are shown in Figure 5.11. Best-fit curvature is shown for each epoch in all four bands. The overall trend for each band is fairly similar, although the three higher frequency bands have more scatter than the 1175 MHz band. The scattering event previously identified around epoch 15 is apparent in all four bands, although the three higher frequency bands increase in curvature before epoch 15. The highest two frequency bands reach higher curvature values than the 1175 or 1380 MHz bands.

Since the four bands are probing four different frequency ranges, it would not be unreasonable to see scattering behavior change across the bands. However, the fact that all four bands show a similar trend in curvature suggests that the scattering behavior is similar across the bands. As a result, we can constrain curvature further by treating all four bands for a particular epoch as a single observation and finding a best fit curvature across the entire range of frequencies. This is shown in Figure 5.12. The scattering event is still apparent, and curvature values throughout the observations are consistent with measurements of each band independently and, indeed, with measurements of each chunk of an observation independently. A few epochs have lower curvatures, at around 0.02 s^3 . These include epochs 2, 3, 14, 16, 28, and 31.

Summary

A qualitative and quantitative analysis of the B1737+13 dataset under study has revealed a number of interesting features. Both forms of analysis are in agreement that the primary arc is best resolved during the early epochs, and then a scattering event occurs around epoch 15. This scattering event is characterized by two main features:

1. The primary arc becomes less resolved, looking “fuzzy” or diffuse.

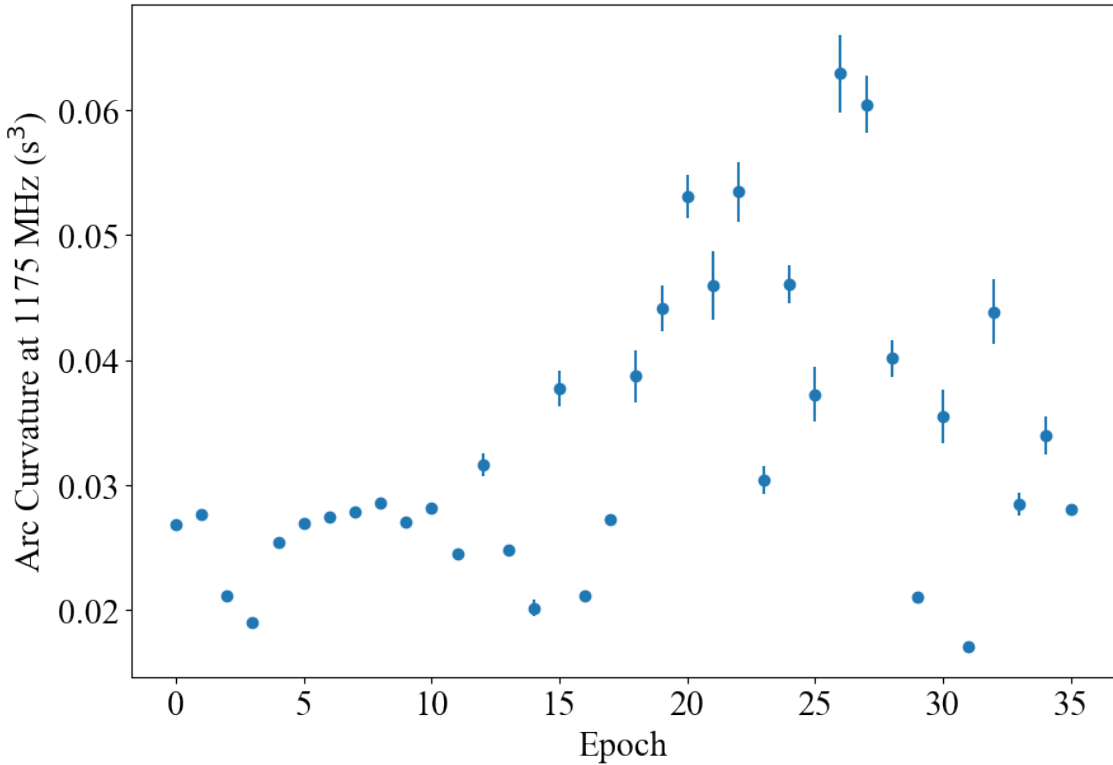


Figure 5.12: Curvature values for each epoch, obtained by finding fitting all four bands simultaneously for a ν^{-2} dependence across a single observation. The scattering event is still apparent, and curvature values throughout the observations are consistent with measurements of each band independently. A few epochs have lower curvatures, at around $0.02 s^3$. These include epochs 2, 3, 14, 16, 28, and 31.

2. Measured curvature values increase significantly, from the primary arc curvature of roughly 0.026 s^3 to values of up to 0.070 s^3 .

In the next chapter, we will seek a model of scattering in the B1737+13 system that can explain these features.

Chapter 6

Modeling the Scintillation of Pulsar B1737+13

6.1 Interaction Curvature

6.1.1 Definition

Consider a situation like that shown in Figure 6.1, where a primary scattering screen is located closer to the observer than a secondary scattering screen. Both screens consist of discrete scattering points for simulation purposes, and the primary screen is so called because it contains more scattering points over a larger extent. When we simulate this system, following the method of Screens (van Kerkwijk & van Lieshout, 2022), we will construct the wavefield as a composite of the wavefield due to scattering off of both screens and the wavefield due to scattering off of the primary screen only. Such a wavefield from a system described above is show in panel (a) of Figure 6.2, where the primary arc is composed of 101 discrete scattering points and the secondary arc is composed of 5 discrete scattering points. In this wavefield, we see the lower curvature primary arc as well as five arcs at much higher curvature. The higher curvature arcs are also composed of 101 points, indicating that we are seeing five copies of the primary arc, each corresponding to a different scattering point on

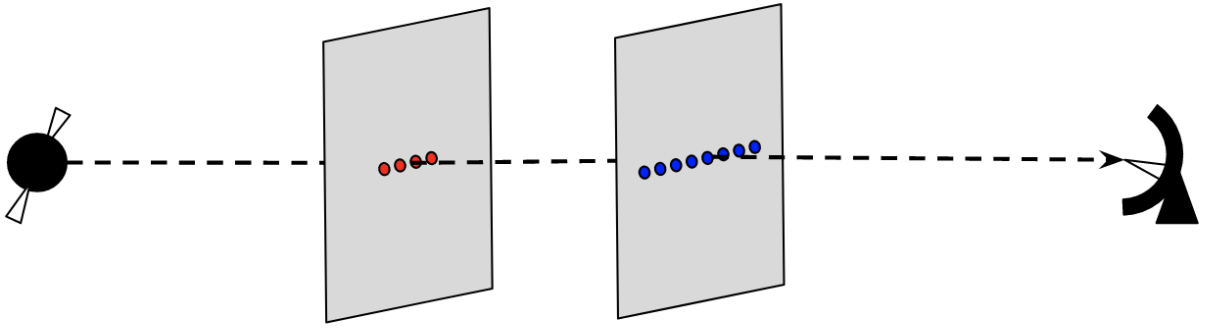


Figure 6.1: A schematic of a system with a primary scattering screen (blue images) and a secondary scattering screen (red images), with the primary scattering screen located closer to the observer.

the secondary arc.

In panel (b) of Figure 6.2, we see the wavefield broken down by the scattering screen(s) that produced it. The wavefield due to scattering off of both screens is shown in orange, and the wavefield due to scattering off of the primary screen is shown in blue. The wavefield due to scattering off of the secondary screen is shown in red for reference and connected by a dotted parabola to indicate the curvature of the secondary screen. From that, we can see that the higher curvature arcs have apexes that are located at points on the secondary arc. Thus, although the secondary arc is not visible in the wavefield, it nevertheless also affects the wavefield. Henceforth, I shall refer to these higher curvature arcs due to scattering off of both screens as *interaction arcs*, with the curvature of interaction arcs being referred to as the *interaction curvature*:

Interaction Arcs: Parabolic arcs in the wavefield of a two-screen system corresponding to scattering by both screens.

Interaction Curvature: The curvature of an interaction arc; η_{int} .

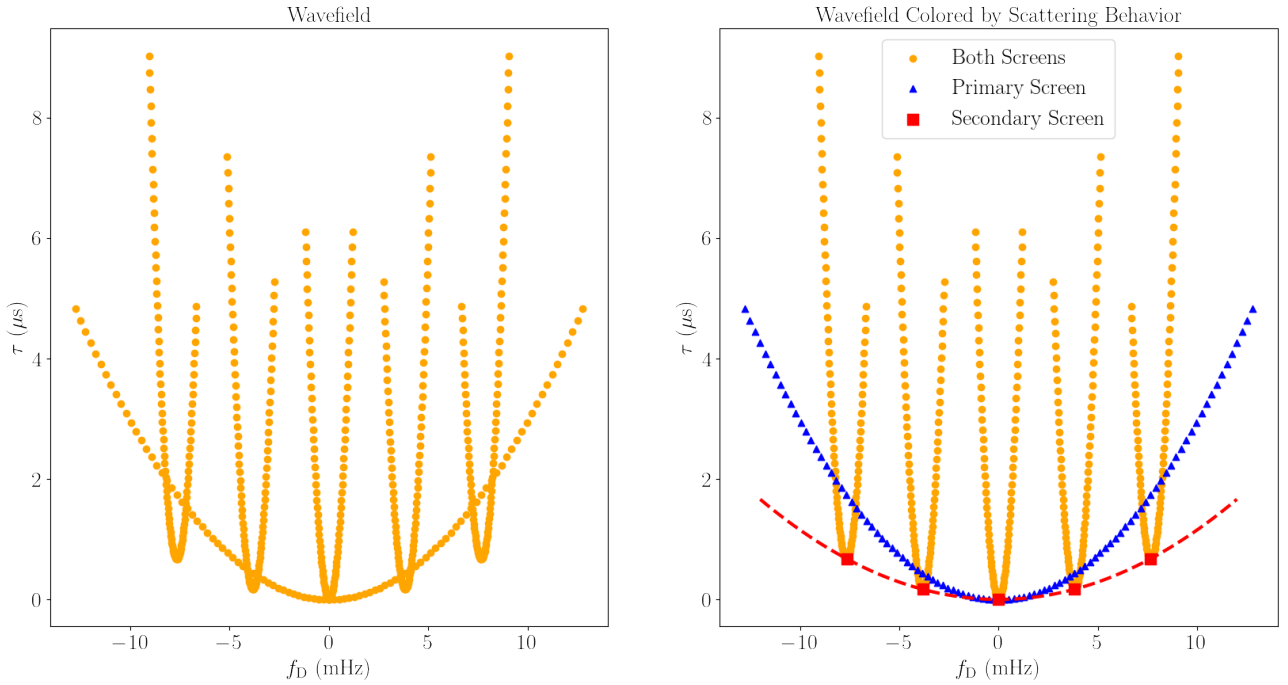


Figure 6.2: The wavefield from a situation like that in Figure 6.1, simulated using the Sprenger et. al. equations. The primary screen is composed of 101 discrete scattering points and located 2.5 kpc from the observer, and the secondary screen is composed of 5 discrete scattering points and located 3.2 kpc from the observer. In panel (a), the composite wavefield from scattering due to both screens and scattering due to the primary screen only is shown. In panel (b), the wavefield from the interaction of the two screens is shown in orange, the wavefield from scattering due to the primary screen is shown in blue, and the wavefield from scattering due to the secondary screen is shown in red and connected by a dotted parabola to indicate the curvature of the secondary screen.

6.1.2 A Problem Arises

No notion of interaction curvature exists in the literature, so we proceed into uncharted territory to characterize how interaction curvature behaves in a two-screen system. To easily find the interaction curvature of a two-screen system, we use a secondary screen consisting of a single scattering point at the line of sight. In this situation, there is only one interaction arc, and it is centered at the origin. The curvature of this arc can then be measured by performing a least-squares fit to a second order polynomial and taking the coefficient of the second order term.

Figure 6.3 shows the interaction curvature of a simulated B1737+13 as a function of distance (from the observer) to the primary screen and distance to the secondary screen. It reveals a clear discontinuity in the interaction curvature when the secondary screen is located at the same distance from the observer as the primary screen. A discontinuity is expected when the screens are in the same place, as the scattering behavior required for such a situation is non-physical. What happens on either side of this discontinuity is more interesting. When the secondary screen is located in front¹ of the primary screen, the interaction curvature is lower, decreasing as the primary screen moves towards the pulsar. On the other hand, when the secondary screen is located behind the primary screen, the interaction curvature is higher, increasing as the secondary screen moves towards the pulsar.

It is notable that interaction curvature behaves differently depending whether the secondary screen is located in front of or behind the primary screen. This is problematic, as it seems to indicate that whether we call a screen “primary” or “secondary” makes a physical difference on scattering. This should not be the case, as there is nothing intrinsic to a screen that makes it “primary” or “secondary”. Thus, we need to return to our definition of interaction curvature and see if there is a way to make it more physically meaningful.

¹Throughout this and subsequent sections, “in front” means closer to the observer and “behind” means further away from the observer.

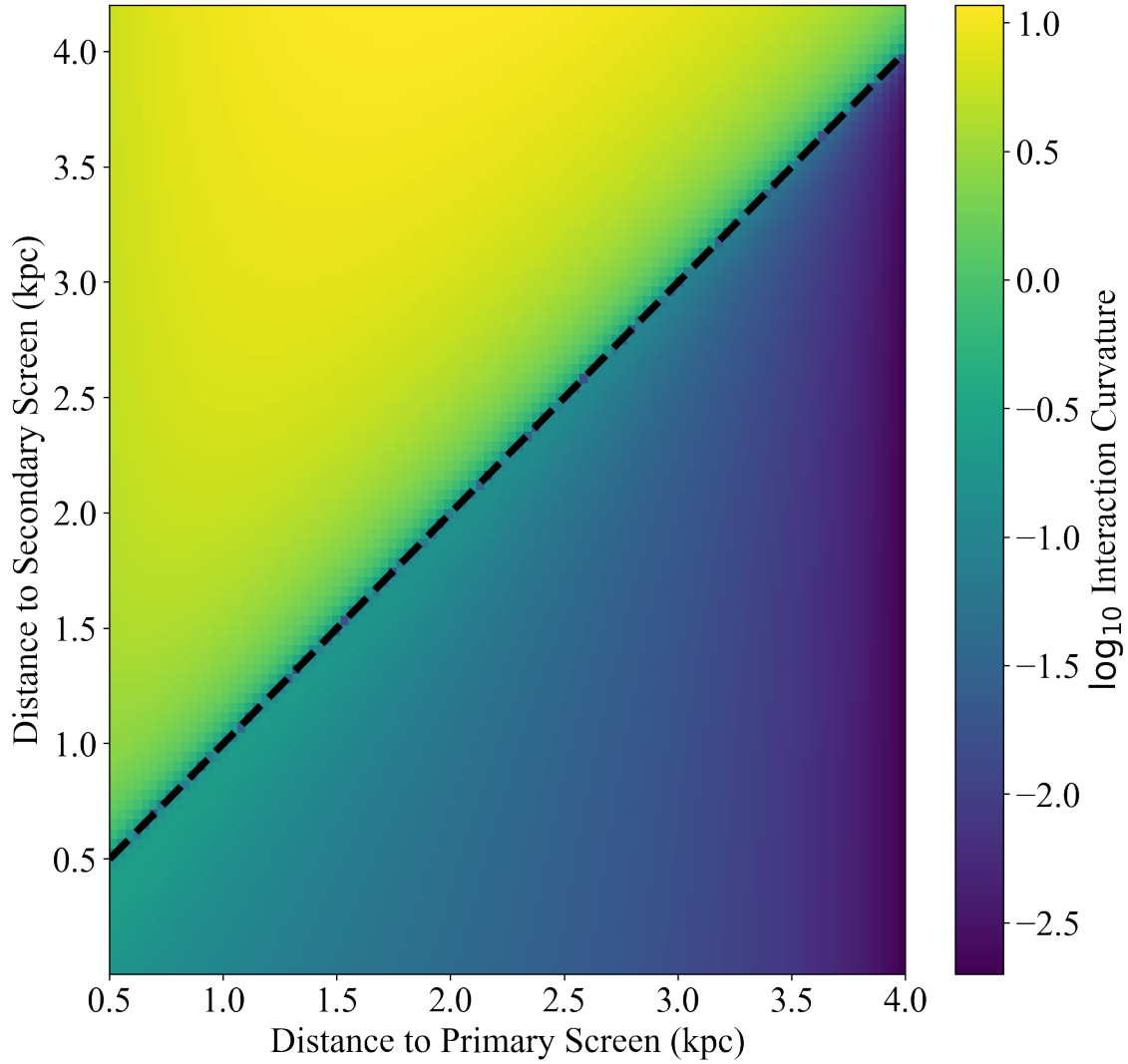


Figure 6.3: Interaction curvature of a simulated B1737+13 system with a primary 1-D scattering screen and secondary 1-D scattering screen located at various distances from the observer, with the base 10 logarithm of the interaction curvature shown as the color of each pixel. Both screens have a rotation of 46 degrees on the sky in this example. The dotted black line indicates the distance points where the primary screen and secondary screen are located at the same distance from the observer. Interaction curvature shows two different behaviors depending on the relative positions of the primary and secondary screens. When the secondary screen is located in front of the primary screen, the interaction curvature is lower, decreasing as the primary screen moves towards the pulsar. When the secondary screen is located behind the primary screen, the interaction curvature is higher, increasing as the secondary screen moves towards the pulsar.

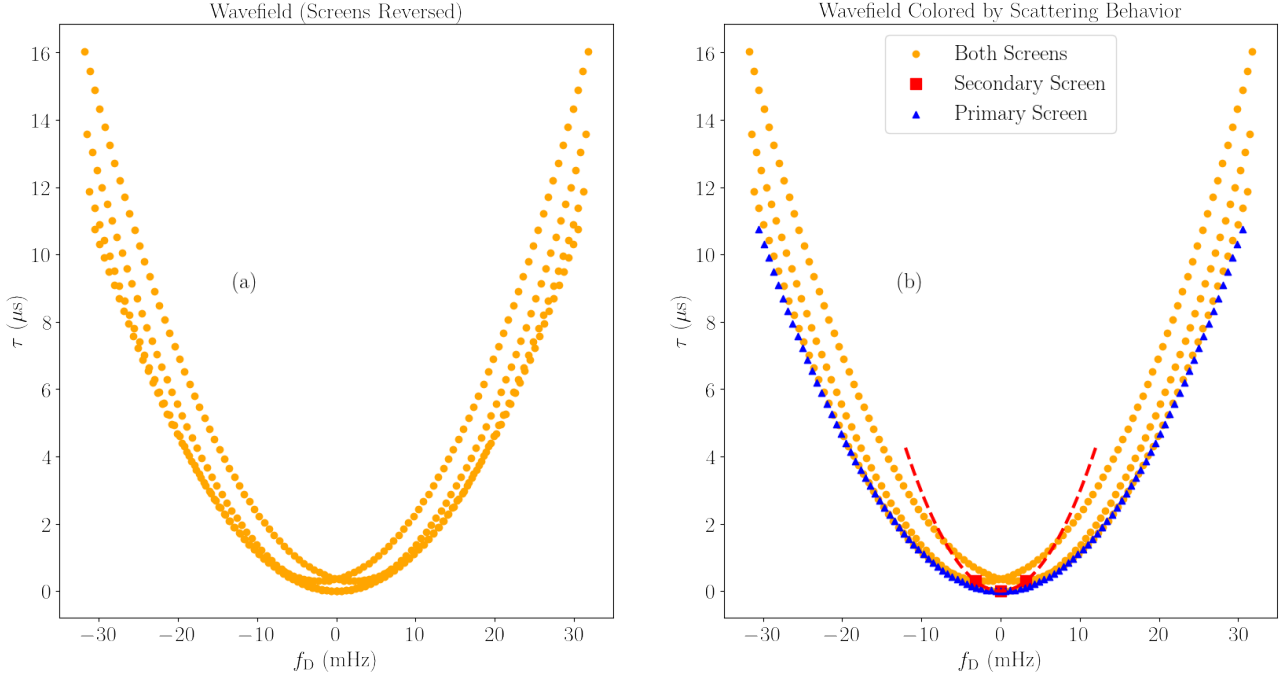


Figure 6.4: The wavefield from a situation like that in Figure 6.1, except with the order of the screens reversed. The secondary arc is now 2.5 kpc from the observer and the primary arc is 3.2 kpc from the observer. The interaction arcs now have a much lower curvature than in Figure 6.2, and the secondary screen now has a higher curvature than the primary screen, as the primary screen is now the one closer to the pulsar.

6.1.3 Revising the Definition of Interaction Curvature

Let us return to the situation of Figure 6.1, but now reverse the order of the two screens. As shown in Figure 6.4, the interaction arcs now have a much lower curvature than in Figure 6.2. The behavior looks markedly different, when all that has changed is a reversal of the order of the screens. Of course, the primary screen is still made up of 101 points and the secondary screen is made up of 5 points, so the reversal has changed the situation physically. However, we don't expect interaction curvature to depend on how many points are in each screen, so this does not resolve the problem.

To resolve this problem, we need to first think about how we actually make the wavefield for scattering off of two screens. We make each point of the wavefield by choosing a point in the primary screen and a point in the secondary screen; then, we calculate τ and f_D for this interaction and add it to the wavefield. We can choose these points in any order we like as

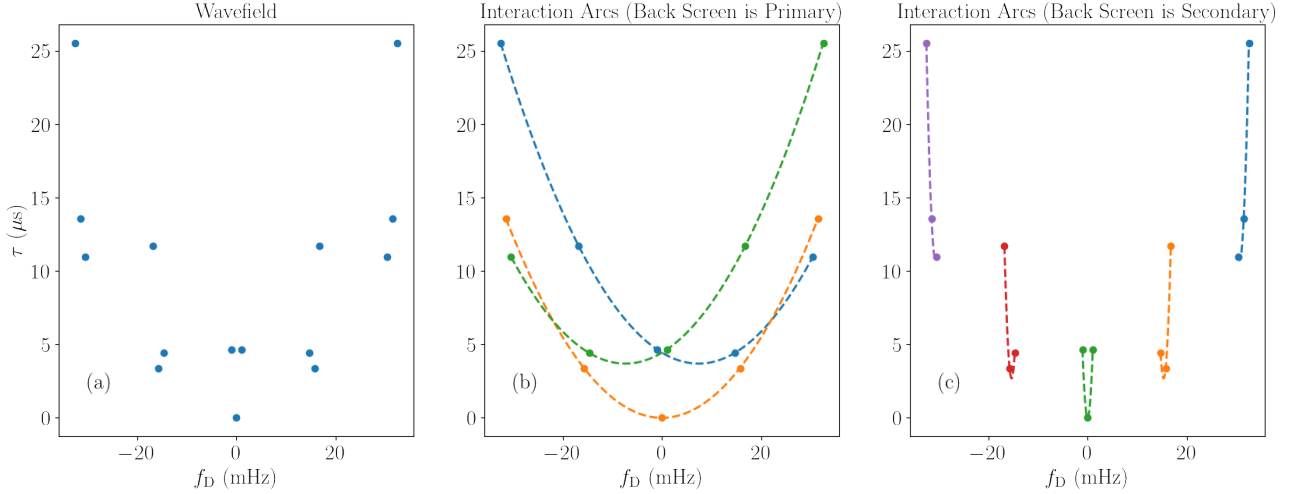


Figure 6.5: Panel (a) shows the wavefield from the interaction between a screen closer to the observer (the front screen) with three points and a screen farther from the observer (the back screen) with five points. In Panel (b), we have plotted the wavefield in groups, with each group corresponding to the interactions of one point in the front screen with each point in the back screen. In Panel (c), we have plotted the wavefield in different groups, with each group corresponding to the interactions of one point in the back screen with each point in the front screen. Each group is given a different color, and as panels (b) and (c) show, the points in a group can be joined by a parabola to form an interaction arc. This shows that there are two ways to define the interaction arcs depending on how we make the wavefield.

long as we end up with all possible combinations of points from the two screens. There are, however, two logical orders to use:

1. Choose a point from the primary screen, and for each point in the secondary screen, calculate τ and f_D and add it to the wavefield. Repeat this process for each point in the primary screen.
2. Choose a point from the secondary screen, and for each point in the primary screen, calculate τ and f_D and add it to the wavefield. Repeat this process for each point in the secondary screen.

In our simulations, we have used the second method, and we find that there is one interaction arc for each point in the secondary screen. However, we could just as easily use the first method. Figure 6.5 shows the wavefield from the interaction between a screen closer to the observer (the front screen) with three points and a screen farther from the observer (the back

screen) with five points. We can plot the wavefield in groups using one ordering, where each group corresponds to the interactions of one point in the front screen with each point in the back screen. We can also plot the wavefield in with a different ordering, where each group corresponds to the interactions of one point in the back screen with each point in the front screen. These two ways are shown in panels (b) and (c) respectively. As we can see, the points in a group can be joined by a parabola to form an interaction arc. However, since there are two different sets of groups, there are two different sets of interaction arcs depending on which ordering we use. Panel (b) has three interaction arcs made up of five points each, while panel (c) has five interaction arcs made up of three points each.

Our model actually gives us two equivalent ways of identifying the interaction arcs, as there are two different ways to overlay sets of parabolas over the same wavefield. When one screen has many more scattering points than the other, it will be much easier to identify the interaction arcs formed by the second ordering method, as each parabola will be made up of many more points than the parabolas formed by the first ordering method. However, there is no inherent preference for identifying one set of interaction arcs over the other. It still makes sense to identify the interaction arcs by the second ordering method since the primary screen has many more points in our model, but we need to refine our definitions to make this clear:

Interaction Arc: The parabola-shaped set of points in the wavefield that are formed by the interaction of a single point in the secondary screen with each point in the primary screen.

Interaction Curvature: The curvature of the interaction arc formed by the interaction of a single point in the secondary screen with each point in the primary screen.

6.1.4 Characterizing Interaction Curvature Behavior

Now that we are more confident in our definition of interaction curvature, we can use it to characterize the behavior of the interaction arcs in our model. We have already seen in Figure 6.3 that the interaction arcs have two different behaviors depending on whether the secondary screen is in front of or behind the primary screen. Let us now hold the primary

screen distance fixed at a distance of 2.5 kpc—the closest possible distance to achieve the observed primary arc curvature—and vary the secondary screen distance. We will also hold the rotation of both screens fixed at 46 degrees relative to a line of constant declination on the sky. This direction is parallel to the motion of the pulsar on the sky, thus minimizing the curvature of each screen. The results are shown in Figure 6.6. Panel (a) shows the simulated data compared to the curvature of the primary screen. As the secondary screen approaches the observer, the interaction curvature approaches the curvature associated with the primary screen. In the opposite direction, the interaction curvature increases as the secondary screen approaches the primary screen before reaching a steep discontinuity, decreasing rapidly as the secondary screen passes through the primary screen. On the other side of the primary screen, the interaction curvature rises dramatically through several orders of magnitude as the secondary screen approaches the pulsar.

Several model fits were attempted to describe the behavior of interaction curvature as a function of secondary screen distance, including exponential fits, logarithmic fits and sigmoidal fits. However, the model that best described the data is shown in panel (b) of Figure 6.6 and is as follows:

$$\eta_{\text{int}}(x) = \begin{cases} \frac{a_1}{x-b_1} + c_1 + \frac{k}{(x-d_1)^2} & x < d_1 \\ \frac{a_2}{x-b_2} + c_2 + \frac{k}{(x-d_1)^2} & x > d_1 \end{cases}, \quad (6.1)$$

where η_{int} is the interaction curvature, x is the distance from the observer to the secondary screen, d_1 is the distance from the observer to the primary screen, and $a_1, b_1, c_1, a_2, b_2, c_2$, and k are the fit parameters.

This model is a combination of two $1/x$ fits: one for $x < d_1$ and one for $x > d_1$, with a $1/(x - d_1)^2$ term added to account for the discontinuity in the curvature at $x = d_1$. It appears from this that interaction curvature has an overall a/x dependence on secondary screen distance, with $a > 0$ for $x < d_1$ and $a < 0$ for $x > d_1$. The piecewise nature of the model is necessary to account for the discontinuity, and it is less concerning given the limitations of our conception of interaction curvature.

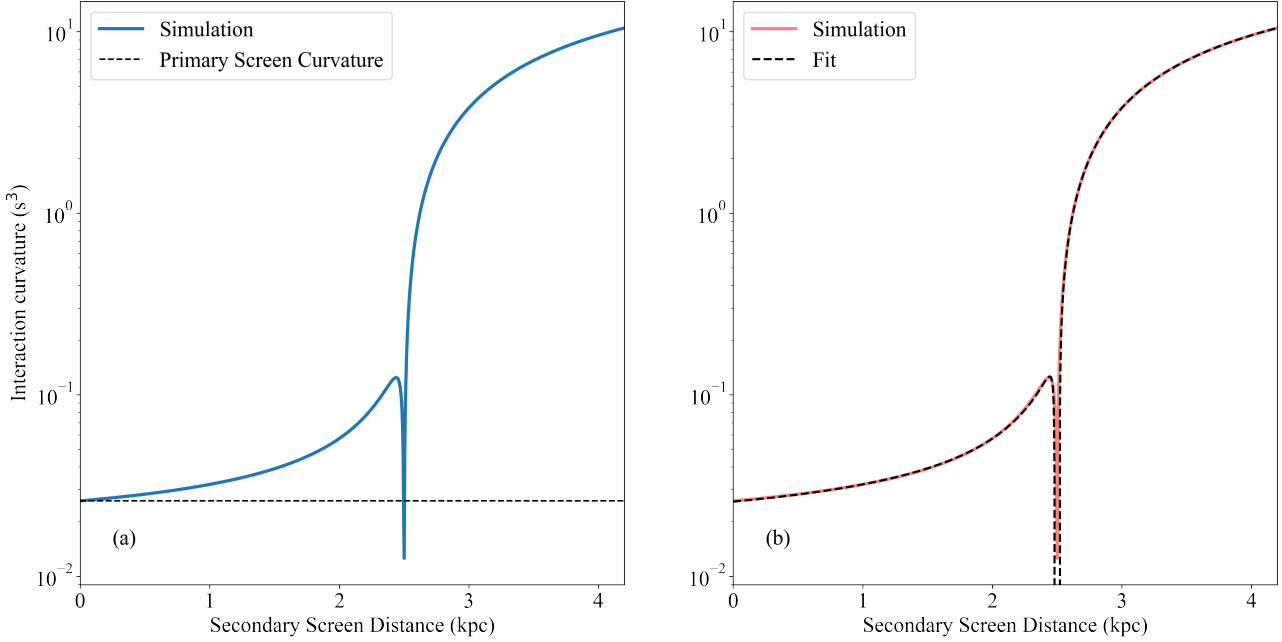


Figure 6.6: Interaction curvature of a simulated B1737+13 system with a primary 1-D scattering screen located at 2.5 kpc with a rotation of 46 degrees on the sky and a secondary screen with a rotation of 46 degrees at various distances indicated. Panel (a) shows the simulated data compared to the curvature of the primary screen. Interaction curvature approaches the curvature associated with the primary screen as the secondary screen approaches the observer and experiences a discontinuity as the secondary screen approaches the primary screen. Curvature rises steeply for a secondary screen between the pulsar and the primary screen. Panel (b) shows the simulated data fitted with a model of arc curvature as a function of secondary screen distance given by Equation 6.1.

We can make this model more complete by now allowing the rotation of the secondary screen to vary. Figure 6.7 shows the interaction curvature of a simulated B1737+13 system with the primary screen fixed at 2.5 kpc and a rotation of 46 degrees on the sky, and a secondary screen at various distances from the observer and with various rotations on the sky. Interaction curvature behaves quite differently depending on the angular offset of the secondary screen from the primary screen. While the curvature for all angular offsets follow the same general trend, the width of the discontinuity at the primary screen decreases as the angle of the secondary screen is more offset from the primary screen, and interaction curvature is overall decreased for secondary screens with larger angular offsets.

For higher angular offsets, interaction curvature no longer increases over several orders of magnitude as the secondary screen approaches the pulsar, but rather increases much more modestly, remaining at the same order of magnitude as the primary screen curvature throughout.

As we have said, 2.5 kpc is the closest distance the primary screen can be to the observer in order to have a curvature as low as the observed primary screen curvature of the B1737+13 system. However, we can place the primary screen closer to the pulsar and keep the same curvature by increasing the rotation of the primary screen on the sky relative to the direction of the pulsar's motion. Figure 6.8 shows the interaction curvature of a simulated B1737+13 system with a primary screen fixed at 3.2 kpc and a rotation of 93 degrees on the sky, and a secondary screen at various distances from the observer and with various rotations on the sky. The trend in interaction curvature is now markedly different and more complicated than in Figure 6.7. As the secondary screen approaches the primary screen from the observer side, interaction curvature spikes drastically for angular offsets from 5 to 40 degrees and then decreases sharply as the secondary screen reaches the primary screen. For other angular offsets, interaction curvature increases more gradually as the secondary screen approaches the primary screen, and angular offsets of 70 and 80 degrees even see a decrease in interaction curvature in this region. Behind the primary screen, interaction curvature increases as the secondary screen approaches the observer for all angular offsets, but the increase varies greatly depending on the angular offset.

Figure 6.8 shows that interaction curvature depends not just on the rotation of each screen relative to each other, but also on the rotation of each screen relative to the direction of the pulsar's motion. This makes sense, as the curvature of each individual screen depends on the rotation of that screen relative to the direction of the pulsar's motion.

In this section, we developed the concept of an interaction arc, and we studied how interaction curvature changes as the parameters of a two-screen scattering model are varied. In the next section, we will use the insights gained from this section to develop a plausible

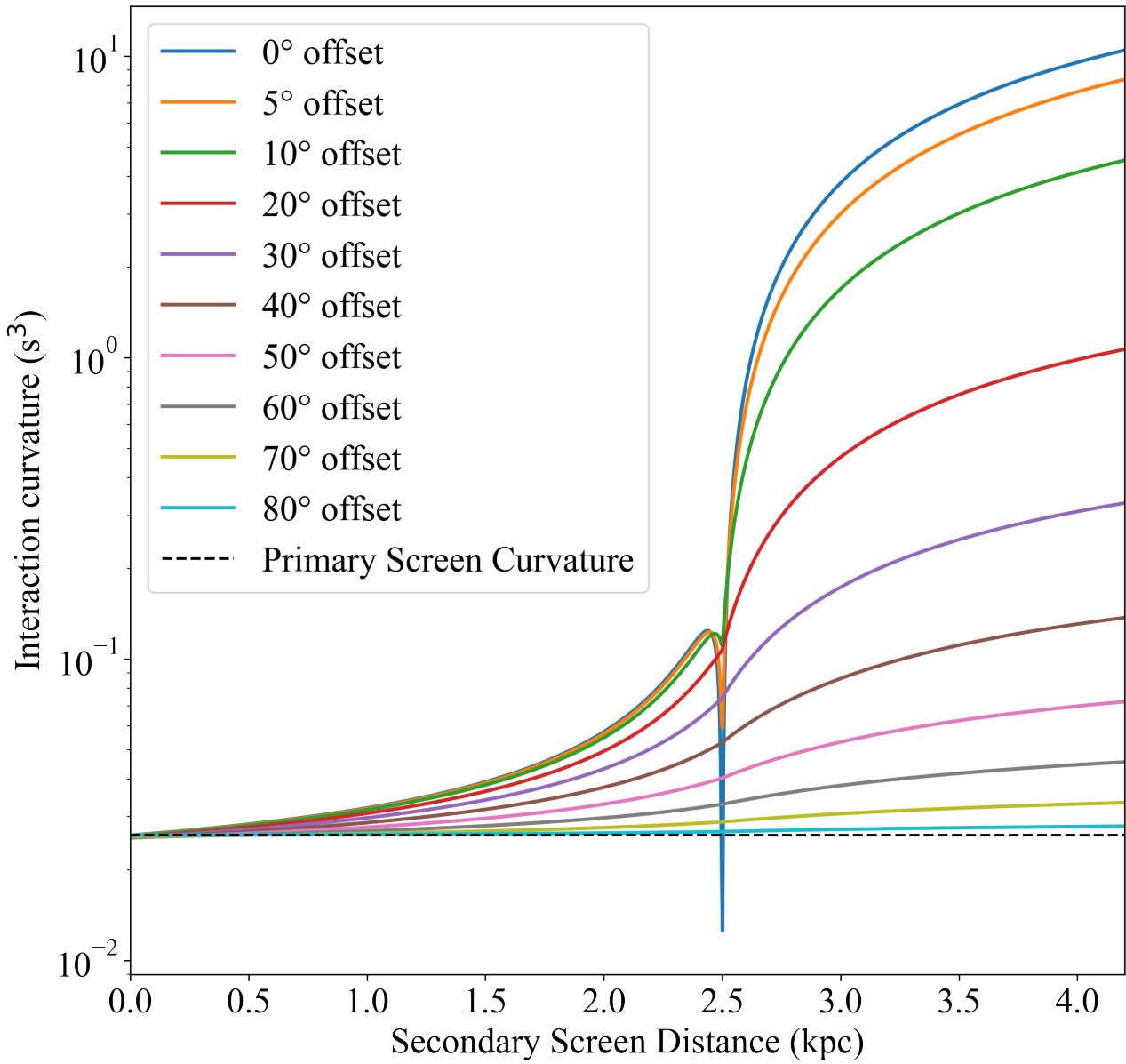


Figure 6.7: Interaction curvature of a simulated B1737+13 system with a primary 1-D scattering screen located at 2.5 kpc with a rotation of 46 degrees on the sky and a secondary scattering screen at various distances from the observer, and with various rotations on the sky. The angular offsets indicated by the legend are the rotations of the respective secondary screen relative to the 46 degree rotation of the primary screen. The dotted black line indicates the curvature of the primary screen, with interaction curvatures for all angular offsets approaching the curvature of the primary screen as the secondary screen approaches the observer. The width of the discontinuity at the primary screen decreases as the angle of the secondary screen is more offset from the primary screen, and interaction curvature is overall decreased for secondary screens with larger angular offsets.

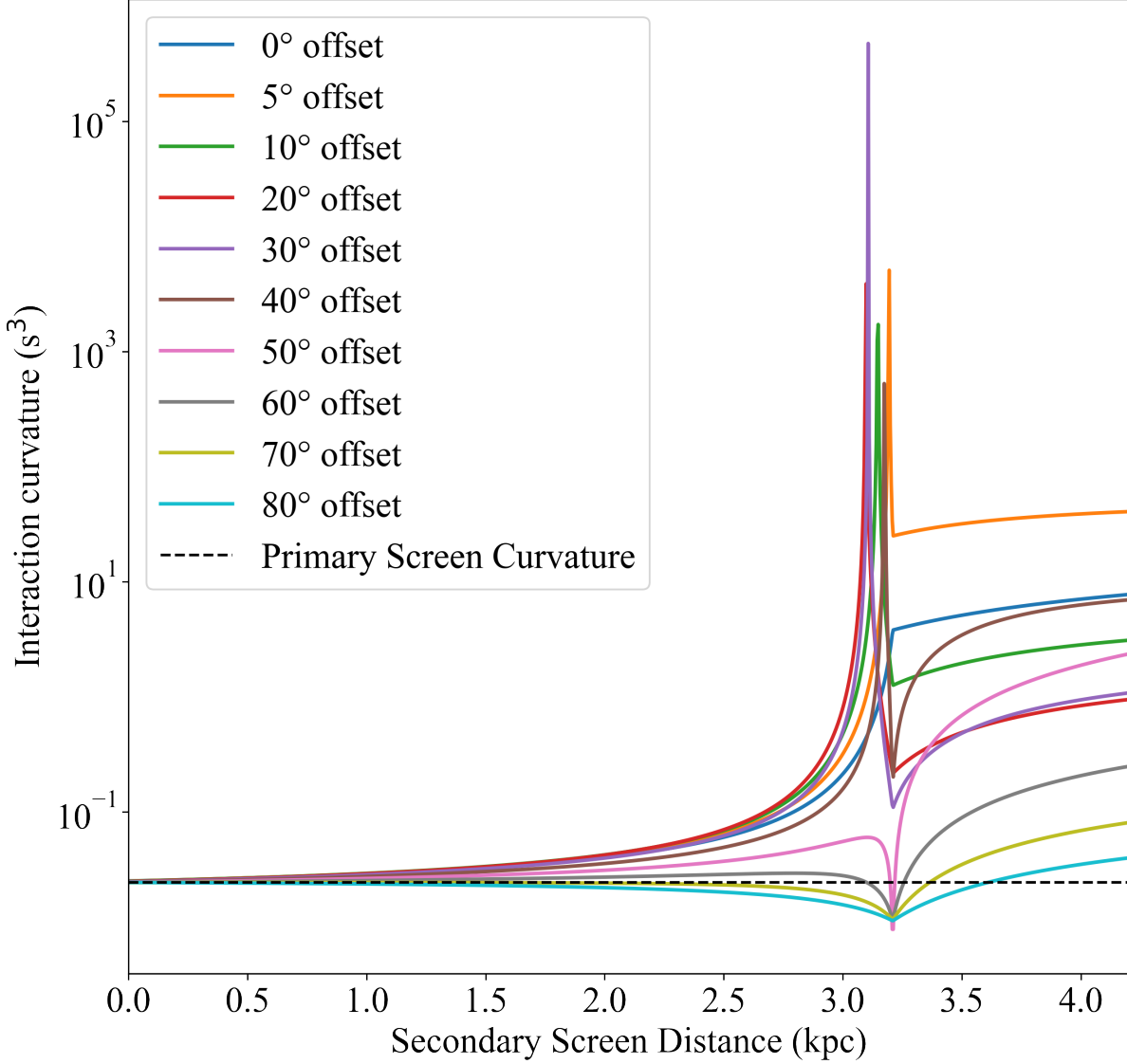


Figure 6.8: Interaction curvature of a simulated B1737+13 system with a primary 1-D scattering screen located at 3.2 kpc with a rotation of 93 degrees on the sky and a secondary scattering screen at various distances from the observer, and with various rotations on the sky. The angular offsets indicated by the legend are the rotations of the respective secondary screen relative to the 93 degree rotation of the primary screen. The dotted black line indicates the curvature of the primary screen, with interaction curvatures for all angular offsets approaching the curvature of the primary screen as the secondary screen approaches the observer. We see much different behavior at the discontinuity than in Figure 6.7. As the secondary screen approaches the primary screen from the observer side, interaction curvature spikes drastically for angular offsets from 5 to 40 degrees and then decreases sharply as the secondary screen reaches the primary screen. Other angular offsets increase more gradually as the secondary screen approaches the primary screen, and angular offsets of 70 and 80 degrees even see a decrease in interaction curvature in this region. Behind the primary screen, interaction curvature increases for all angular offsets, though the increase is much greater for some angular offsets, and there is no clear patterning to this ordering.

model of scattering for the B1737+13 system.

6.2 Modeling

Recall the two key features of the scattering event that we noted (5.2.2): that the secondary spectrum becomes “fuzzy,” and that we measure higher arc curvatures than the primary screen curvature. The idea of interaction arcs can help us explain both of these features.

The higher curvatures seen in the dataset had values of around $\eta = 0.06 \text{ s}^3$. We will proceed under the hypothesis that the interaction curvature is around this value. The increase up to this value and decrease after this value, under this hypothesis, is due to the curvature search algorithm trying to fit both the primary screen curvature and the interaction curvature overlaid on top of each other, with curvature values closer to the primary screen when it is the dominant factor in scattering, and curvature values closer to the interaction curvature when the interaction is the dominant factor in scattering.

As a starting point for the model, we can refer back to Figure 6.8. With a primary screen at 3.2 kpc and a rotation of 93 degrees on the sky and a secondary screen at 2.5 kpc, interaction curvature is around 0.06 s^3 for a variety of angular offsets. Our model for simulations has the secondary screen at 2.5 kpc and aligned with the direction of the pulsar’s motion at 46 degrees on the sky. We used 101 scattering points for the primary screen and 20 scattering points for the secondary screen. These model parameters are listed in Table 6.1. For the brightness distributions, we used a Gaussian $\exp(-\theta^2/2\sigma^2)$ distribution, and, for the secondary screen, we used a uniform distribution for simplicity.

We performed three tests of this model in an attempt to recreate three situations in our dataset. In the first, the primary arc is well resolved with inverted arclet substructure, as in the early part of the dataset. In the second and third, the scattering event has made

Parameter	Primary Screen Value	Secondary Screen Value
Distance (kpc)	3.2	2.5
Rotation (degrees)	93	46
Scattering Points	101	20
Point Density (points/AU)	0.045	0.1

Table 6.1: Parameters of the two-screen scattering model used to model the B1737+13 system.

Model	Primary Screen Magnification	Interaction Magnification	Primary Screen Brightness Function $2\sigma^2$ (mas 2)	Secondary Screen Offset from LOS (AU)
One-Screen Scattering	1.0	0.0	0.05	0.0
Symmetric Two-Screen Scattering	0.5	1.0	0.01	0.0
Asymmetric Two-Screen Scattering	0.5	1.0	0.01	0.5

Table 6.2: Relevant parameters of the three different scattering models shown in Figures 6.9, 6.10, and 6.11, respectively.

the primary arc fuzzy, with the second situation representing a fuzzy arc that is roughly symmetric and the third representing a fuzzy arc that is asymmetric. Relevant parameters for the three models are listed in Table 6.2, and the results of these simulations are shown along with similar dynamic and secondary spectra from the dataset in Figures 6.9, 6.10, and 6.11, respectively.

For the first situation, we used a one-screen scattering model with the primary screen only. This produced a model secondary spectrum with a well defined primary arc with inverted arclet substructure. This mimics the basic structure of the secondary spectrum from the early part of the dataset, with a comparison shown to MJD 53830 in Figure 6.9. However, the model dynamic spectrum has much larger regions of power than the data, and the secondary spectrum contains additional substructure that is not present in the model. It is

possible, then, that the one-screen scattering model cannot fully explain the early part of the dataset.

For the second situation, we used a two-screen scattering model with the secondary screen centered on the line of sight. The magnification of the wavefield from the primary arc only was reduced by 50% to account for the fact that the presence of the secondary screen would reduce the amount of light reaching the observer that has only been scattered by the primary screen. The variance of the brightness distribution for the primary screen also decreased by a factor of 5, increasing the magnification of the core relative to the wings to reduce the intensity of inverted arclets. This produced a model secondary spectrum that is much fuzzier, particularly around the origin. The fuzziness is also symmetric in this case. These feature mimic some of the secondary spectra during the scattering event, with MJD 53978 shown in Figure 6.10 for comparison. The size of the scintles in the model dynamic spectrum is also similar to the data. The fuzziness in the secondary spectrum extends further out from the origin than in the model, but the overall comparison is quite promising.

For the third situation, we used a two-screen scattering model with the secondary screen offset from the line of sight by 0.5 AU. All other model parameters were the same as in the second situation. This produced a model secondary spectrum that is fuzzy, but is asymmetric with power mainly in quadrants 1 and 3. This is shown in Figure 6.11 along with data from MJD 54004. Again, the fuzziness in the secondary spectrum extends further out from the origin than in the model, but the overall comparison is also promising.

Because we have selected parameters that produce a desired interaction curvature, we can be confident that our model accurately reproduces the observed higher curvature during the scattering event. As for the fuzziness, the model secondary spectra have been able to capture some of the fuzziness seen during the scattering event. There is certainly room for the model to improve in this regard, but the model is able to capture some essential features of the data.

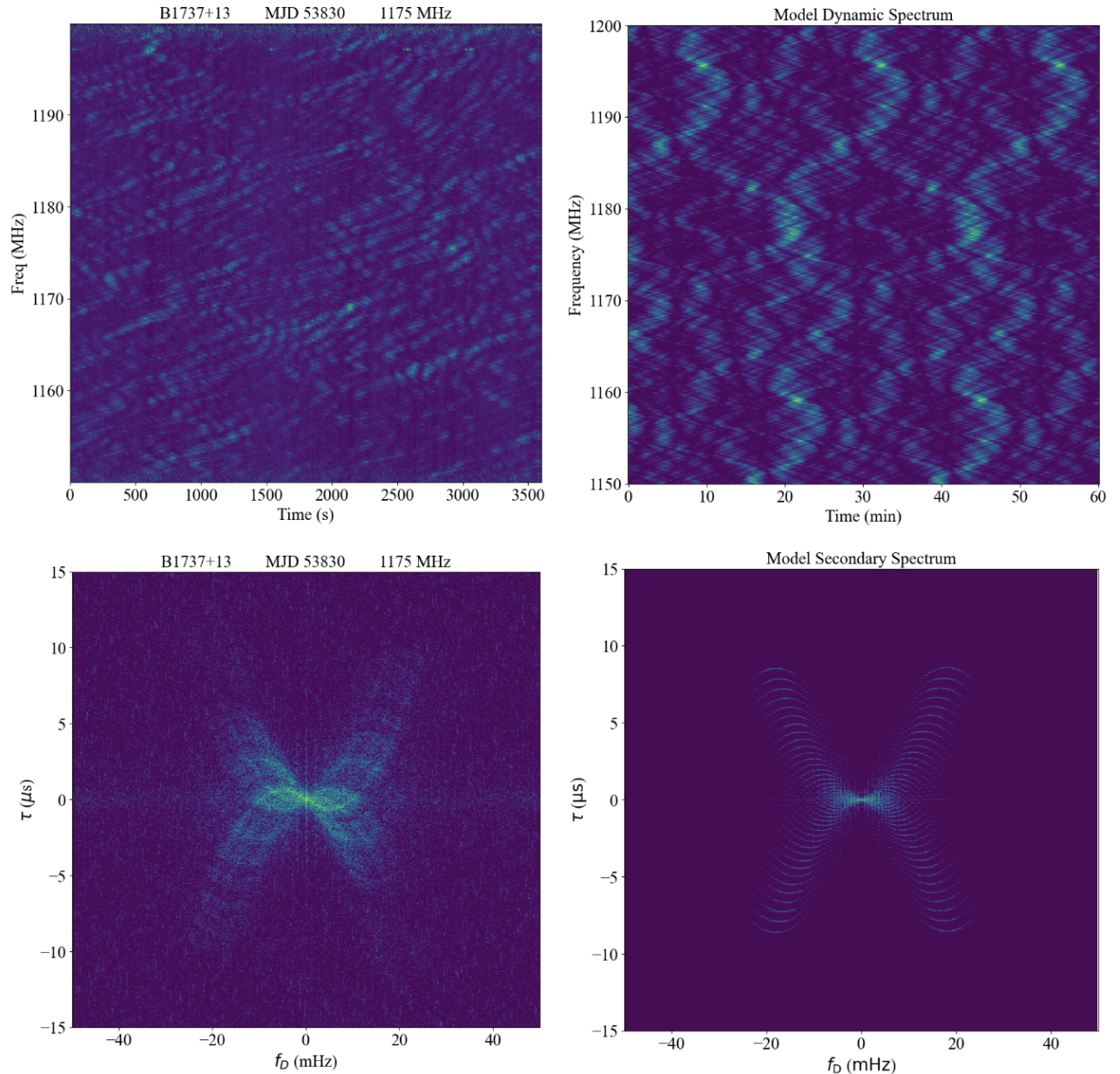


Figure 6.9: Dynamic and secondary spectra from the 1175 MHz observation of B1737+13 at MJD 53830 compared with model dynamic and secondary spectra produced with Screens.

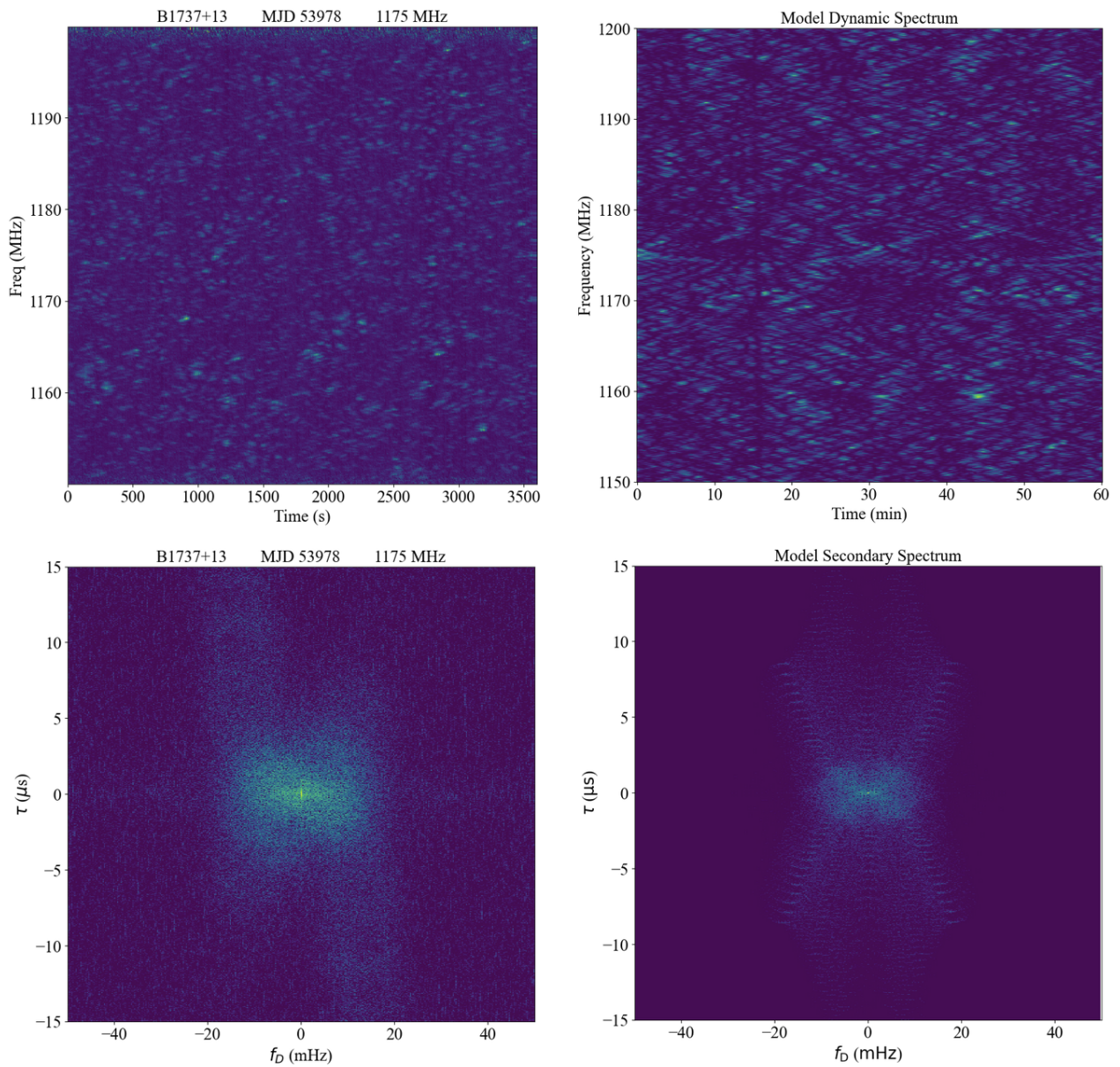


Figure 6.10: Dynamic and secondary spectra from the 1175 MHz observation of B1737+13 at MJD 53978 compared with model dynamic and secondary spectra produced with Screens.

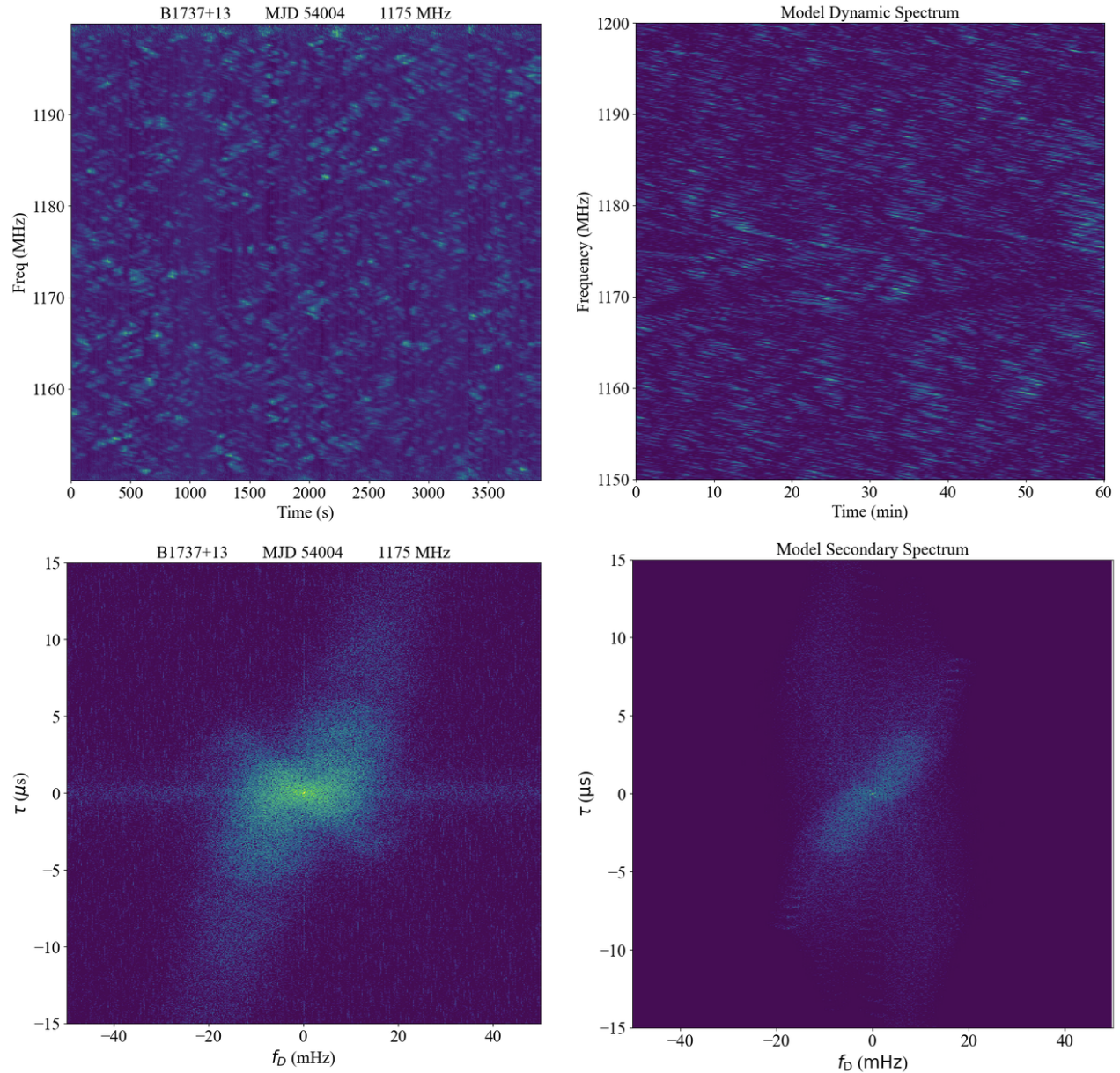


Figure 6.11: Dynamic and secondary spectra from the 1175 MHz observation of B1737+13 at MJD 54004 compared with model dynamic and secondary spectra produced with Screens.

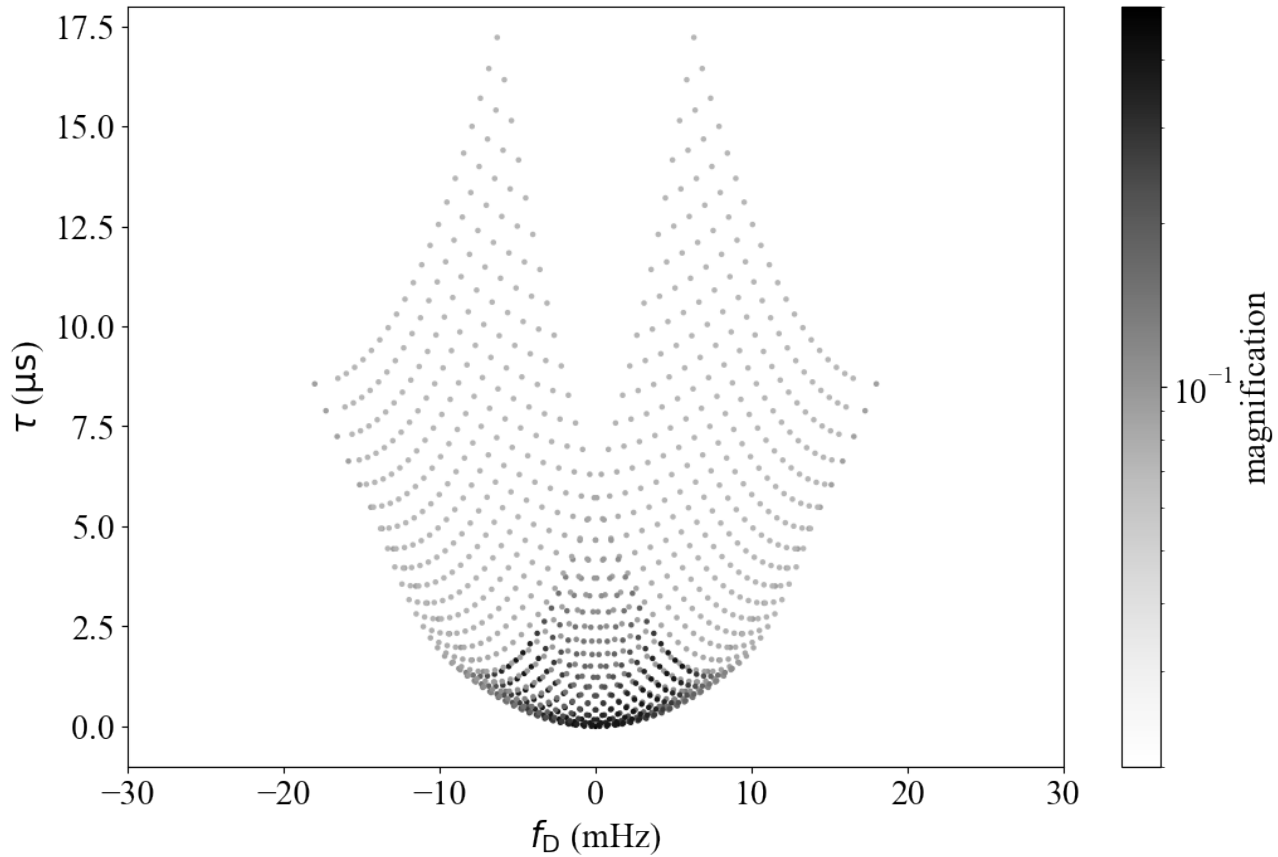


Figure 6.12: Wavefield from the two-screen scattering model that is shown in Figure 6.10. The interaction arcs sit on top of the primary arc such that the primary arc is washed out, giving a fuzzy appearance.

To see where the fuzziness comes from in the model, we can look at the wavefield. This is shown in Figure 6.12 to represent the second situation, where the secondary screen is centered on the line of sight. The interaction arcs are overlaid on top of the primary arc such that the primary arc is competing with the interaction arcs for visibility. This has the effect of washing out the primary arc, which gives the fuzzy appearance.

Chapter 7

Conclusion

7.1 Summary of Results

This thesis has presented a model for the variable scintillation of pulsar B1737+13 that uses two-screen scattering. To arrive at this model, we first measured the arc curvature during the 36-epoch observation. This revealed the presence of a primary arc, but it also showed a scattering event which was associated with higher measured curvatures and fuzziness in the secondary spectrum. A single screen model is not sufficient to explain this. We developed the idea of interaction arcs, which arise in the wavefield from scattering off of both a primary and a secondary screen. Once we refined our definition of interaction arcs, we were then able to show how they behave with various screen parameters and use that knowledge to find a plausible set of parameters for a two-screen model. We then showed that this model is also able to explain fuzziness in the secondary spectrum.

The model we have developed shows great promise in demonstrating the qualitative and quantitative effects of a secondary screen on scintillation arc behavior. On the basis of the curvature measurements and the model presented, it is highly likely that more than one screen is responsible for the observed scintillation. The model we have developed shows that two screens are able to explain many features of the data.

7.2 Future Work

The model we have developed is an excellent starting point. However, there is much room for improvement. Some of this could potentially come from adjusting model parameters: the extent of each screen, the distances, the rotations, and the brightness distributions. For example, we used a uniform brightness distribution for the secondary screen, but we could also try a Gaussian distribution. We could also try other distributions for either screen.

Further study is also needed in understanding the interaction arcs. We have already shown that our understanding of them is subject to the pattern-seeking nature of the human brain. While we were able to refine our definition of interaction arcs, it is still possible that we have not found the best formulation of what we observe in the wavefields of simulated two-screen scattering. We also have no method currently for determining interaction curvature *a priori* based on the screen parameters, nor do we know if such a method even exists.

In terms of the dataset itself, there is a lot of richness that is still unexplored. While we have been able to probe deeply into the data using theta-theta mapping and curvature search algorithms, we have yet to try other methods of curvature analysis. We have yet to try phase retrieval, another technique developed by Baker et al. (2022). We could also investigate underlying brightness distribution using techniques developed by Stinebring et al. (2019).

Bibliography

Astropy Collaboration, Price-Whelan, A. M., Lim, P. L., et al. 2022, ApJ, 935, 167

Baker, D., Brisken, W., van Kerkwijk, M. H., et al. 2022, , 510, 4573

Blandford, R. D., Hewish, A., Lyne, A. G., & Mestel, L. 1992, Phil. Trans. Roy. Soc. A, 341, 1

Ellison, M. W. 1952, Irish Astronomical Journal, 2, 5

Hemberger, D. A., & Stinebring, D. R. 2008, ApJ, 674, L37

Hewish, A., Bell, S. J., Pilkington, J. D. H., Scott, P. F., & Collins, R. A. 1968, Nature, 217, 709

Hewish, A., Scott, P. F., & Wills, D. 1964, Nature, 203, 1214

Hill, A. S., Stinebring, D. R., Barnor, H. A., Berwick, D. E., & Webber, A. B. 2003, ApJ, 599, 457

Lorimer, D. R., & Kramer, M. 2005, Handbook of Pulsar Astronomy (Cambridge University Press)

Lyne, A. G., & Smith, F. G. 1990, Pulsar Astronomy (Cambridge: Cambridge University Press)

Main, R. A., Parthasarathy, A., Johnston, S., et al. 2023, , 518, 1086

McKee, J. W., Zhu, H., Stinebring, D. R., & Cordes, J. M. 2022, ApJ, 927, 99

Reardon, D. J. 2023, Scintools, <https://github.com/danielreardon/scintools>

Reardon, D. J., Coles, W. A., Bailes, M., et al. 2020, ApJ, 904, 104

Rickett, B. 2001, International Astronomical Union Colloquium, 182, 5–10

Rohatgi, A. 2022, WebPlotDigitizer: Version 4.6, <https://automeris.io/WebPlotDigitizer>

Sprenger, T., Main, R., Wucknitz, O., Mall, G., & Wu, J. 2022, MNRAS, 515, 6198

Sprenger, T., Wucknitz, O., Main, R., Baker, D., & Brisken, W. 2021, MNRAS, 500, 1114

Stinebring, D. 2007, Astronomical Society of the Pacific Conference Series, 365, 254

Stinebring, D. R., McLaughlin, M. A., Cordes, J. M., et al. 2001, ApJ Letters, 549, L97

Stinebring, D. R., Rickett, B. J., & Ocker, S. K. 2019, ApJ, 870, 82

Stinebring, D. R., Rickett, B. J., Minter, A. H., et al. 2022, ApJ, 941, 34

van Kerkwijk, M. H., & van Lieshout, R. 2022, mhvk/screens: v0.1,

doi:10.5281/zenodo.7455536